JAIST Repository
https://dspace.jaist.ac.jp/

| | |
|---|---|
| Title | その場TEM観察による2硫化モリブデン膜の歪に依存した物性に関する研究 |
| Author(s) | 謝, 立林 |
| Citation | |
| Issue Date | 2021-09 |
| Type | Thesis or Dissertation |
| Text version | ETD |
| URL | http://hdl.handle.net/10119/17533 |
| Rights | |
| Description | Supervisor:大島　義文, 先端科学技術研究科, 博士 |

JAIST
JAPAN
ADVANCED INSTITUTE OF
SCIENCE AND TECHNOLOGY

Japan Advanced Institute of Science and Technology

Doctoral Dissertation

# Study of strain dependence of physical properties in $MoS_2$ layers by in situ transmission electron microscopy observation

XIE Lilin

Supervisor: Professor Yoshifumi Oshima

Graduate School of Advanced Science and Technology

Japan Advanced Institute of Science and Technology

[Materials Science]

September 2021

**Referee-in-chief:**

Professor Yoshifumi Oshima

*Japan Advanced Institute of Science and Technology*

**Referees:**

Professor Masahiko Tomitori

*Japan Advanced Institute of Science and Technology*

Professor Mikio Koyano

*Japan Advanced Institute of Science and Technology*

Professor Yukiko Takamura

*Japan Advanced Institute of Science and Technology*

Professor Satoru Tanaka

*Kyushu University*

## Abstract

**Study of strain dependence of physical properties in $MoS_2$ layers**

**by in situ transmission electron microscopy observation**

XIE Lilin
1820416

Owing to the ultrathin crystal structure, two-dimensional (2D) materials, such as molybdenum disulfide ($MoS_2$), exhibit unique mechanical and electronic properties that make them promising for the application in electronic devices. Applying strain is an effective method to modify its properties since strain can modulate the crystal structure and electronic structure. However, experimentally investigation on atomic-scale during straining has been rarely reported. Therefore, in this thesis, we developed an in situ stretching holder for the transmission electron microscopy (TEM) observation, and investigated the strain dependence of the physical properties of $MoS_2$ nanosheets.

We developed an in situ stretching TEM holder, which was designed for the purpose of investigating the strain dependence of 2D materials. The stretching function is performed with the piezo actuator, which generates a displacement by applying the bias voltage and drives the deformation of the titanium plate for stretching the trench in the Si chip. Our in-situ stretching TEM holder enabled us to obtain an atomic TEM image and a linear relationship between the applied bias voltage and gap distance, indicating it is stable and effective for the TEM observation. The displacement step of the holder was measured to be 0.06 nm/mV that is applicable for stretching on atomic scale.

We performed in situ stretching TEM observations of the $MoS_2$ nanosheet by our stretching TEM holder, for investigating the mechanical response of $MoS_2$ nanosheet under stretching. The fracture process of a multilayer $MoS_2$ nanosheet was studied, in which the crack of the sample was propagated along with the zigzag edge layer by layer. Our results suggested that the fracture of $MoS_2$ nanosheet was an interlayer fracture with a zigzag propagated orientation. Additionally, we observed the rippled structure in the $MoS_2$ nanosheet, and investigated the structural modulation during stretching. The periodically atomic-contrast change during stretching with a 0.7% tensile strain was revealed, it was attributed to the out-of-plane displacement of the sample during stretching.

We proposed a method for the quantitatively identifying ripple structure of $MoS_2$ nanosheets on atomic scale. The periodical ripple structure, which formed along the armchair configuration, were observed in the $MoS_2$ nanosheet. According on the geometry of the rippled structure and the projective feature of TEM, we investigated the relationship between the geometric structure of the ripple and corresponding apparent strain, that the rippled can be identified on atom-scaled with high-resolution TEM (HR-TEM) images. By applying the geometric phase analysis method to the HR-TEM images of ripple structures, we obtained the corresponding apparent strain distribution and proposed that the ripple structure of the $MoS_2$ layers could be quantitatively estimated on the sub-nanometer scale. We experimentally observed the ripple structure of the $MoS_2$ layers, and analyzed the corresponding apparent strain. It was found that it was an inclined sinusoidal pattern, which is inclined approximately 7.1° from the plane perpendicular to the incident electron beam, and its period and amplitude were estimated to be 5.5 and 0.3 nm, respectively. Furthermore, the bending model of $MoS_2$ nanosheet was suggested to be the layer model with no-in-plane distortion, due to the van der Waals interaction between layers of $MoS_2$ was very weak.

We experimentally investigated the mechanical response of $MoS_2$ nanosheets under applied strain conditions. The geometric evolution with increasing tensile strain was revealed by using our strain-based analysis on HR-TEM images. It was found that the relationship between the tensile strain and the amplitude/period was not followed the 1/4 power scale law, indicating the continuum mechanics is failed in explaining the bending of 2D materials at the atomic scale. This failure was attributed to the incapable plate model for the bending of the 2D materials. By analyzing the strain dependence of the geometric structure of the ripples, we estimated the Poisson's ratio of $MoS_2$ nanosheet from our experimental results

during stretching, which showed that the Poisson's ratio increased to 0.57 when the longitudinally tensile strain increased to ~1.6%. We proposed an analytical model, which revealed that the nonlinear response of Poisson's ratio with increasing strain was originated from the changing of bond length was not proportional to strain.

In conclusion, the physical properties of atomic-scale $MoS_2$ layers have been investigated by our homemade TEM holder. Our result revealed the interlayer fracture mechanism, proposed a strain-analysis based method to estimating rippled structure at the subnanometer scale, and investigated the strain dependence of the structure and Poisson's ratio of $MoS_2$ layers. Our results provide an experimental method for investigating 2D materials under strain conditions, which can contribute to a better understanding of their mechanical properties at the atomic scale and the development of their future applications.

**Keywords:** in situ TEM, $MoS_2$, stretching, rippled structure, strain dependence.

# Table of Contents

**Abstract** ........ I

**Table of Contents** ........ III

**Chapter 1 Background** ........ 1

Introduction ........ 1

1.1 Two-dimensional materials and rippled structure ........ 2

1.1.1 Two-dimensional materials and molybdenum disulfide ........ 2

1.1.2 Influence of strain on the properties of $MoS_2$ ........ 4

1.1.3 Rippled structure of 2D materials ........ 5

1.1.4 The bending of 2D materials ........ 8

1.2 Strain engineering and characterization methods of 2D materials ........ 11

1.3 Purpose and contents this research ........ 14

1.4 Conclusion ........ 16

**Chapter 2 Experimental method** ........ 17

Introduction ........ 17

2.1 Transmission electron microscopy ........ 18

2.1.1 The component of TEM ........ 18

2.1.2 The imaging of TEM ........ 20

2.1.3 The geometric phase analysis of TEM image ........ 23

2.1.4 The influence of thickness on the visibility of HR-TEM image ........ 24

2.2 Fabrication process of Si chip for 2D material ........ 27

2.2.1 The experimental equipment used in the fabrication process ........ 27

2.2.2 The overall fabrication process of Si chip ........ 30

2.3 Sample preparation and transfer ........ 33
2.3.1 Preparation ........ 33
2.3.2 Dry transfer process ........ 35
2.4 Conclusion ........ 37

**Chapter 3 Development of stretching TEM holder for 2D materials ........ 38**
Introduction ........ 38
3.1 The design of the in situ stretching TEM holder ........ 39
3.2 The calibration of the in situ stretching TEM holder ........ 41
3.3 Electrical conductance measurement ........ 45
3.4 Conclusion ........ 48

**Chapter 4 The stretching and fracture of $MoS_2$ nanosheet ........ 49**
Introduction ........ 49
4.1 The structure of the of $MoS_2$ nanosheet observed in TEM. ........ 50
4.2 The structural modulation of $MoS_2$ nanosheet under stretching ........ 54
4.3 The fracture of $MoS_2$ nanosheet ........ 57
4.4 Conclusion ........ 64

**Chapter 5 The atomic-scale ripple structure in $MoS_2$ nanosheet ........ 66**
Introduction ........ 66
5.1 The TEM observation of the ripple structure of $MoS_2$ nanosheet ........ 67
5.2 Strain-analysis method to identify the atomic-scale ripples with TEM images 70
5.2.1 Apparent strain of the rippled structure ........ 71
5.2.2 Apparent strain in the HR-TEM image of the rippled structure ........ 72
5.3 Retrieving ripple structure from experimental result ........ 78
5.3.1 Analysis of the observed $MoS_2$ rippled structure ........ 78

5.3.2 Estimation of the observed $MoS_2$ ripple structure ... 82
5.4 The bending of multilayer $MoS_2$ nanosheet ... 84
5.4.1 Apparent strain of ripple structure with a small inclination angle ... 84
5.4.2 Bending model of the multilayer $MoS_2$ ... 85
5.4.3 The appearance of the atomic-scale $MoS_2$ ripple structure ... 90
5.5 Conclusion ... 96

**Chapter 6 Strain dependence of the ripple structure in $MoS_2$ nanosheet ... 98**
Introduction ... 98
6.1 The strain dependence of the ripple structure of $MoS_2$ nanosheet ... 99
6.1.1 The initial ripple structure of $MoS_2$ nanosheet before stretching ... 99
6.1.2 The evolution of ripple structure during stretching ... 103
6.2 The strain dependence of the Poisson's ratio of rippled $MoS_2$ nanosheet ... 108
6.2.1 The strain dependence of the geometry of rippled structure ... 108
6.2.2 The strain dependence of Poisson's ratio ... 111
6.3 Conclusion ... 119

**Chapter 7 Summary ... 121**

**References ... 125**

**Appendix Ⅰ ... 136**

**Acknowledgement ... 140**

**List of achievements ... 142**

# Chapter 1 Background

## Introduction

Chapter 1.1 is the introduction part that introduces the background of the two-dimensional (2D) materials, especially the molybdenum disulfide and its strain dependence on the physical properties, which includes the theoretical and experimental research. Rippled structure of 2D materials is also explained with introducing the recent progresses. In Chapter 1.2, we briefly review the recent research progress on the strain engineering and characterization methods of 2D materials. In Chapter 1.3. the main purpose and significance of the research will be mentioned.

## 1.1 Two-dimensional materials and rippled structure

### *1.1.1 Two-dimensional materials and molybdenum disulfide*

Two-dimensional (2D) materials, which have an atomically thin layered structure, have attracted the abroad research interest since the discovery of graphene [1]. Owing to their ultrathin crystal structure, 2D materials, such as graphene and molybdenum disulfide ($MoS_2$) layer, exhibit unique mechanical and electronic properties. For example, graphene has a fracture strength of 130 GPa and Young's modulus of 1.0 TPa [2] with high electron mobility and good electrical conductivity [3,4]. Except for graphene, as an important and representative 2D material, $MoS_2$ layer has been widely investigated such as its mechanical properties [5–7] and electronic properties [8–10]. Besides, it is found that atomically thin $MoS_2$ can accept up to a tensile strain up to 20% before rupture [11,12], such a high yield strength makes it a promising material for the investigation of mechanical properties of strained 2D material and the application for flexible devices [13,14]. Such exceptional properties of 2D materials make them promising for electronic and mechanical applications [15–18].

The crystalline $MoS_2$ is a layer structure, in which the plane of molybdenum is sandwiched between the planes of sulfide atoms on both sides. Three motifs of $MoS_2$ structure, 3R, 2H, and 1T, have been reported [19]. The number in 3R, 2H, and 1T correspond to the number of layers in the unit cell, and the letter correspond to the type

of symmetry that the R, H, and T stands for the rhombohedral, tetragonal, and hexagonal respectively. There are two coordination of the $MoS_2$ structures, the triangle prismatic coordination and the octahedral coordination. The triangle prismatic coordination makes a 3R or 2H motif, which is semiconducting, as shown in Fig.1.1(a) and (b), respectively. These atomic models are visualized with the software of VESTA [20]. The octahedral coordination makes a 1T motif, which is metallic, as shown in Fig.1(c). Both 2H and 3R motifs are semiconducting, while the 1T phase is reported to be metallic [21]. The most stable state at room temperature is the triangle prismatic coordination in the bulk 2H motif, which has been investigated in this work.

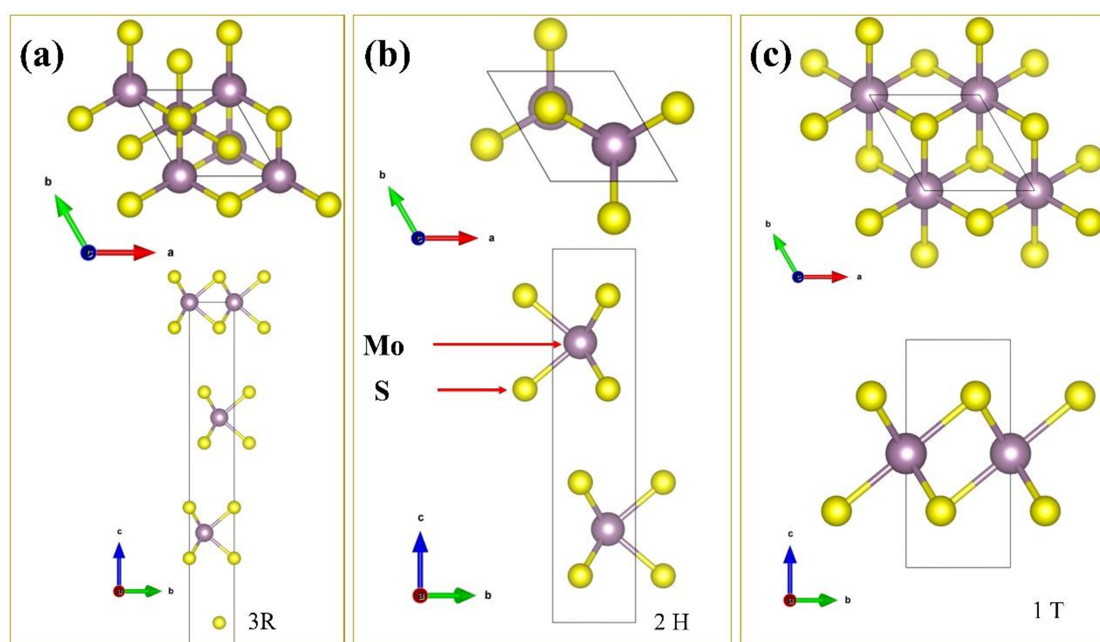


Figure 1.1. (a)-(c) The atomic structure 3R, 2H and 1T phase of $MoS_2$, respectively. Upper: the top view; bottom: the lateral view.

Similar to graphene, the 2D $MoS_2$ can be prepared by the mechanical exfoliation method from bulk. It was reported that the band gap of 2H $MoS_2$ is changed from 1.2 eV (indirect, bulk) [22] to ~1.7 eV (direct, 1 Layer) [23] with the reducing thickness.

### *1.1.2 Influence of strain on the properties of $MoS_2$*

Among the properties of 2D materials, electronic properties have important effects on the electrical behavior, such as bandgaps, carrier density, and mobility, which are keys for the application on the electronic device. Also, the electronic properties of 2D materials are sensitive to strain so that the 2D materials could change both the crystal structure and bandgap structure [24–26]. As for $MoS_2$ structure, its energy band changed from indirect to direct and the carrier mobility can be enhanced significantly by applying the strain [27]. What's more, the bandgap of the bilayer $MoS_2$ was reported to reduce to 0 eV with applied 8% tensile strain [28], as shown in Fig. 1.2. It means that it has the transition from semiconducting to metallic behavior. Although this phenomenon makes it a promising application in low-power and sensor devices, its mechanism has not been clarified. The strain-induced electronic stated change of $MoS_2$ has been mainly reported by the theoretical calculation, while it has been rarely reported by experiments.

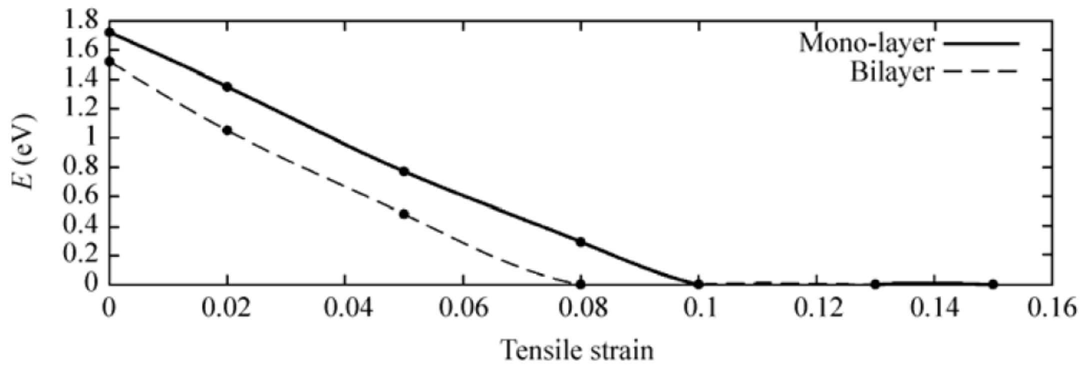


Figure 1.2. Plots of band gap (*E*g) versus strain for mono- and bi-layer $MoS_2$ [28].

### *1.1.3 Rippled structure of 2D materials*

The strain can not only modulate the electronic properties of 2D material, but also their structural properties. Due to the ultra-thin layered structure, 2D materials have been suggested to be not perfectly maintain the flat sheets owing to intrinsic thermal instability [29–31]. Graphene has been reported to form a rippled structure such that the out-of-plane displacement (amplitude) and the fluctuation wavelength (period) of carbon atoms were approximately 1 and 10 nm, respectively [29,30]. Additionally, ripple structures of graphene were observed near the position where the dislocations were intentionally introduced [32], suggesting that the ripple structures can also be formed by internal strain due to the dislocations [33]. Such kinds of ripple structures, which formed due to the thermal instability and internal strain were not periodic structures, as shown in Fig. 1.3.

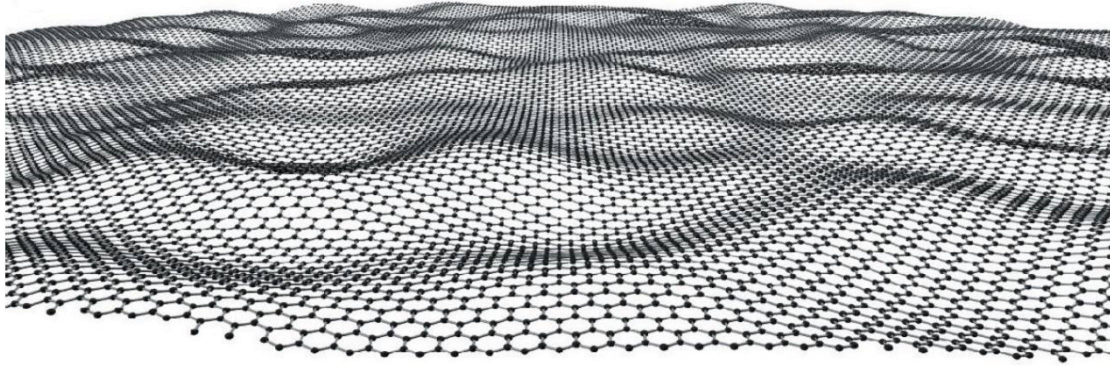

Figure 1.3. The diagram for corrugated graphene [29].

Meanwhile, periodically rippled structures were found in 2D materials, it was reported both in graphene [34–38] and $MoS_2$ [11,39]. Such periodic structure was formed due to externally imposed strains, such as the strain generated from thermally expansion mismatch [36,38] and the strain from substrate straining [39,40]. In the former one, the strain was generated by the difference in thermal expansion coefficient (TEC) between the 2D materials and the substrates. After the heating and cooling process, this mismatch of TEC resulted in the strain in the 2D materials that lead to formation of the periodically rippled structure. As for the latter case, the strain was generated by the pre-strained or stretching substrates. By stretching the substrate in advance before 2D materials was placed on it, the strain was induced and the periodic ripple structures were formed by the shrinking of the substrate. The periodically rippled structure were also formed by stretching the substrate directly that induced the

externally imposed strain. The scanning electron microscope (SEM) image of periodic ripple structures is shown in Fig. 1.4.

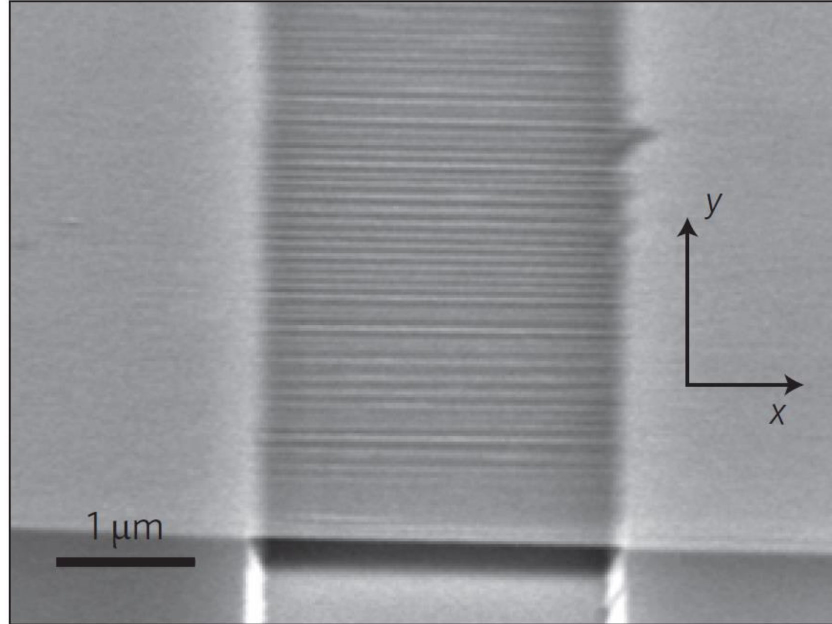


Figure 1.4. SEM image of a bilayer suspended graphene with periodic ripples [36].

The structure of the ripple structures is predicted to be sensitive to the longitudinally tensile strain [41–43], which generates a transverse strain depending on Poisson's ratio to induce an atomic-scale wavy pattern perpendicular to the stretching direction. According to continuum mechanics [41], the relationship between the ripple geometry (the amplitude $A$, and the period $\lambda$) and longitudinal tensile strain ($\varepsilon$) can be described by:

$$\lambda = \frac{(2\pi L t)^{1/2}}{\left[3(1-\nu^2)\varepsilon\right]^{1/4}}, \tag{1.1}$$

$$A = (\nu L t)^{1/2}\left[\frac{16\varepsilon}{3\pi^2(1-\nu^2)}\right]^{1/4}, \tag{1.2}$$

where $L$ is the longitudinal length of the sample, $t$ is the thickness, $\varepsilon$ is the applied tensile strain, and $v$ is Poisson's ratio. Equations (1.1) and (1.2) show the relationships $\lambda \sim \varepsilon^{-1/4}$ and A ~ $\varepsilon^{1/4}$.

The mechanical response of rippled graphene under strain conditions has been extensively studied through theoretical approaches such as molecular dynamics simulations. The stretching of rippled graphene has been approximated with continuum mechanics, according to which the competition between the bending and stretching energy causes the period ($\lambda$) and amplitude ($A$) of the ripple to follow a 1/4-power scaling law [41] for the longitudinally tensile strain ($\varepsilon$), such as $\lambda \sim \varepsilon^{-1/4}$ and $A \sim \varepsilon^{1/4}$. Such a relationship seems to be unique and can be helpful for understanding the mechanical response of 2D materials under stretching.

### *1.1.4 The bending of 2D materials*

The rippling of 2D materials involves their bending behavior, which is related to their thickness, several attempts have been done to clarify the bending of single/multiple layer 2D materials.

The bending of single layer 2D materials, such as graphene and $MoS_2$, is reported to be not involve the in-plane distortion. The molecular dynamics (MD) simulations of

monolayer graphene suggested that the monolayer graphene could be bended by π-orbital misalignment instead of in-plane σ-bond deformations [44], which means there is no in-plane distortion occurred in the bending of single layer graphene. And, the MD simulations of monolayer $MoS_2$ also showed that the bending does not change the Mo–Mo atomic distance even when the bending radius is greater than 4 nm [45]. Also, the Mo–Mo atomic interaction has been reported not to contribute to the bending modulus of monolayer $MoS_2$ [46]. Thus, the in-plane distortion is suggested to be negligible in the bending of single layer of 2D materials.

In the meanwhile, the bending of multilayer 2D materials is complicate than that of single layer, due to the interaction between the layers. Depending to the interlayer interaction, there are two bending models for describing the bending behavior of 2D materials, the plate model and the layer model [47], as demonstrate in Fig.1.5 (a) and (b). The plate model assumes a strong interlayer interaction that the layers act as the glued interfaces, thus, the extension/compression of bond length occur in the outer/inner part of bending region that result in the in-plane distortion, as shown in Fig.1.5 (a). Whereas the layer model assumes a weak interlayer interaction that the different layer acts as the bending of a single layer without in-plane distortion, as shown in Fig.1.5 (b). The bending stiffness (D) was suggested to be the function of the number of layers (N) such as $D \sim N^3$ and $D \sim N$ in the case of plate and layer model, respectively.

Previous experimental studies using pressurized bubbles have reported that the multilayer 2D materials showed an intermediate behavior corresponding to the two models [47] according to the measured bending stiffness, as shown in Fig.1.5 (c).

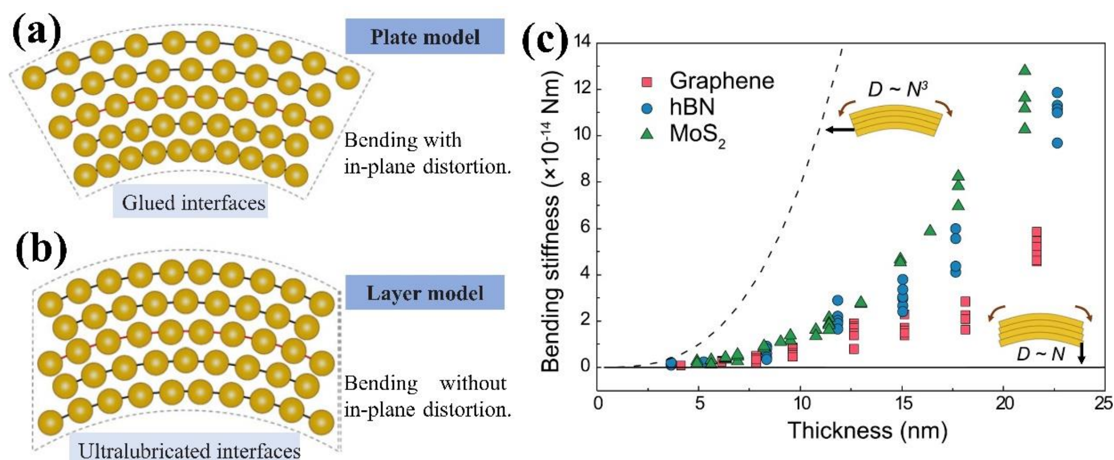


Figure 1.5. Bending of multilayer 2D materials [47]. Illustration of the deformation of bended multilayer 2D materials with plate model (a) and layer model (b), which shows glued and ultra-lubricated interfaces, respectively. (c) The thickness dependence (N: number of layers) of bending rigidity (D) of 2D materials, the dash-dotted and solid lines indicate the theoretical predictions of bending rigidity in the plate and layer bending model, respectively.

Although the MD simulation or experimental methods have been achieved to clarify the bending of 2D materials, the structural characterization of the bending behavior on atomic scale has been rarely reported. To clearly comprehend such atomic-scale

mechanics, ripple structures of 2D materials in the subnanometer range should be studied.

## 1.2 Strain engineering and characterization methods of 2D materials

To clarify the influence of strain on the properties of 2D material, several experimental methods have been developed to apply strain in 2D materials.

One of the common methods to induce the strain in 2D materials is to deform the substrate, such as the bending or stretching of the flexible substrate [48–51], as shown in Fig 1.6. By applying strain on the flexible substrate and combining with spectroscopy methods, such as Raman spectra, and photoluminescence spectroscopy, the strain-induced energy bandgap modulation has been investigated [52]. Also, the morphology can be obtained with scanning electron microscope and atomic force microscope (AFM). Additionally, the electrodes can be deposited on the flexible substrate that makes it possible for analyzing the influence of strain on the application of flexible electronic devices, as shown in Fig 1.6.

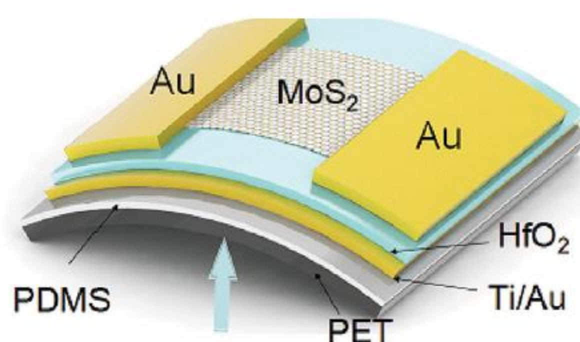


Figure 1.6. The schematic image of the bending device of $MoS_2$ [49].

For the suspended sample, the indentation of a tip can also induce the strain for the 2D materials [53], as shown in Fig.1.7, in which the STM/AFM tip was also used to introduce the strain in the 2D materials. With the help of the AFM tip, which can reflect the information of stress, the mechanical properties can be obtained. Experimentally, the Young's modulus and the elastic constant of the exfoliated graphene was calculated to be 1.0 TPa and 342 N/m [2], respectively. Moreover, the Young's modulus and the tensile strength was estimated to be 270 ± 100 GPa, and 23 GPa in the monolayer $MoS_2$, respectively, with the ultimate strain of 11% [6].

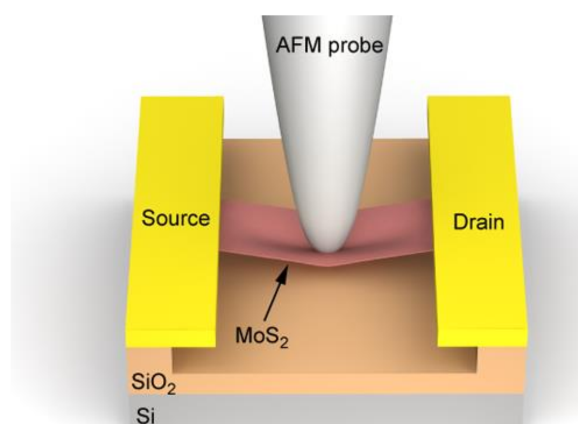


Figure 1.7. The schematic of the indention of $MoS_2$ monolayer with AFM tip [53].

While, it is difficult to realize direct observation of atomic structural change during the straining process. Transmission electron microscopy (TEM), which is a powerful tool to study the structural properties of materials on atomic scale, is attractive for investigating the strain in 2D materials. It was achieved by combining with different

types of TEM sample holder for inducing the strain, such as AFM based [54] and Micro-Electro-Mechanical Systems (MEMS) chip-based [55–57] TEM holders as shown in Fig.1.8. These methods could analyze the strain-induced structural change during the stretching by TEM observation. But limited to the operation of the AFM cantilever and the actuator of the MEMS chip, it is difficult to get stable atomic-scale resolution during observation. It is worth to establish an experimental characterizing method with the atom-scale resolution for quantitative analysis of 2D materials under strain conditions.

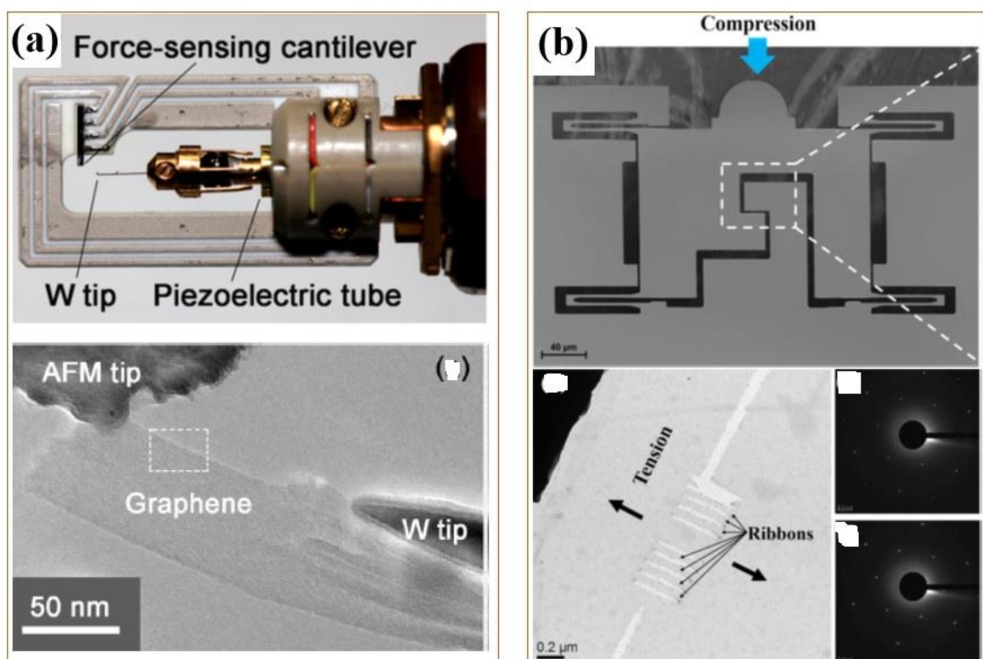


Figure 1.8. (a) Image of the AFM based TEM holder and the TEM image of a stretched graphene nanosheet [54]. (b) SEM image of the MEMS chip and TEM image of the patterned graphene nanoribbons with diffraction patterns from the nanoribbons [56].

## 1.3 Purpose and contents this research

Understanding the physical properties of 2D materials is the key to their application. However, experimental results about the straining process on atomic scale have been rarely reported and corresponding structural change has not been clarified. Experimental investigations are extremely important in clarifying their strain dependence of physical properties. Therefore, to address these issues, the main purpose and contents of this research aim to:

1. Development of in situ stretching TEM holder for 2D materials characterization. The in situ TEM holder has the stretching function, which is driven by a piezo actuator, and must be stable and effective for the TEM observation on atomic scale.
2. By in situ stretching of $MoS_2$ layers, the fracture process of a multilayer $MoS_2$ nanosheet is studied.
3. Exploring the method analyzing the atom-resolved TEM images to estimate the ripple structure in the $MoS_2$ nanosheet quantitatively. Considering the projective feature of TEM images, the ripple structure is thought to be identified by estimating the apparent strain.
4. Investigation of the mechanical response of $MoS_2$ nanosheets under strain conditions. The geometric evolution of rippled $MoS_2$ nanosheets with

increasing tensile strain is investigated. We estimate the strain dependence of the Poisson's ratio of $MoS_2$ nanosheet.

## 1.4 Conclusion

In this chapter, we introduce the background of our research. In Chapter 1.1, we discussed the unique properties of 2D materials and the influence of strain on the properties of 2D materials, the rippled structures in 2D materials and the bending behavior of single and multilayers were also introduced. In Chapter 1.2, we briefly reviewed the recent research progress on the strain engineering and characterization of 2D materials. We introduced the previous method to explore the structure and properties of 2D materials in the experimental aspect of view, corresponding advantages and limitations were analyzed. In Chapter 1.3, we clarified the purpose of our research, the method, and the main point of this thesis.

# Chapter 2 Experimental method

## Introduction

This chapter describes the experimental methods which are related to this work. In Chapter 2.1, we introduce the basic principle of TEM characterization methods, which including the component and the imaging of TEM, the geometric phase analysis method, and the visibilities of the TEM images. In Chapter 2.2, the fabrication process of Si chip for 2D material is introduced. In Chapter 2.3, we will introduce the method of sample preparation and transfer.

## 2.1 Transmission electron microscopy

To investigate the properties of 2D materials on atomic scale, the transmission electron microscope (TEM) is performed, which is a powerful tool to characterize the structure on atomic scale. The ultra-high vacuum TEM (UHV-TEM) (JEM-2000VF, JEOL), with the accelerating voltage of 200 kV, is used in our experiment, it is maintained with a high vacuum (~$0.8 \times 10^{-6}$ Pa) to avoid the adsorption of carbon contaminants during electron beam irradiation, the photograph is shown in Fig. 2.1

Figure. 2.1. The photograph of the TEM (JEM-2000VF, JEOL).

### *2.1.1 The component of TEM*

TEM is an electron microscopy method that using transmitted electrons for imaging. Comparing to the optical microscope (OM), the electron beam is used as the

light source and the magnetic lens is used as the lens. Similar to the OM, the image resolution of TEM can be approximately estimated by the Rayleigh criterion with the following [58]:

$$\delta = \frac{0.61\lambda}{\mu \sin \beta}, \tag{2.1}$$

where $\lambda$ is the wavelength of the electron waves, $\mu$ is the refractive index of the viewing medium, and $\beta$ is the acceptance angle of the objective lens. The Eq. (2.1) expresses the limitation of the resolution, thus, reduce the $\lambda$ is the effective way to improve the image resolution. As for a TEM with the accelerating voltage of 200 kV, the wavelength of the electron waves is 0.00251 nm, which is much less than the diameter of the atom, that it can achieve an atomic-scale resolution. The structure of the conventional TEM [59] is shown in Fig. 2.2 (a), compared to that of the OM, as shown in Fig 2.2(b).

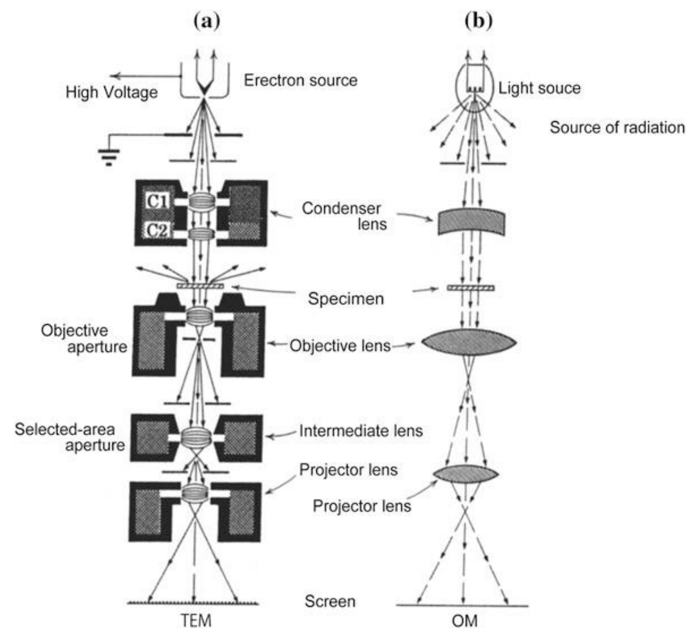


Figure 2.2. The structure of the transmission electron microscope (TEM) (a) and an optical microscope (b) [59].

As demonstrated in Fig. 2.2, a typical TEM is composed of the electron gun, the vacuum system, the electromagnetic lenses, the sample stage, the apertures, and the image recording system. The electron gun is acted as the source of the electron beam. The vacuum system is used for maintaining the high vacuum of the TEM chamber to reduce the influence of gas molecules on the electrons (reducing the mean free path of the electrons) and samples (reducing the electron beam-induced deposition). The electromagnetic lenses in TEM are used to focus the electrons, and it is divided into condenser lens, objective lens, intermediate lens, and the projector lens, as shown in Fig.2.2(a). The sample stage is used to clamp the sample holder in the TEM chamber, in order to produce the image/ diffraction pattern of the sample through the objective lens. The sample stage allows the insertion of different types of sample holders, with which we can achieve specific TEM observation of the specimen. The apertures are used to filtered the electron beams. The image recording system is used to record the image from the electrons.

### *2.1.2 The imaging of TEM*

The TEM imaging is achieved with the transmitted electrons. The basic imaging process is described as following.

a. The electron gun emits and accelerates electrons, and the emitted electrons are focused by the condenser lens.

b. Then, the incident electrons interacted with the sample, and the electrons will transmit/scatter through the specimen.

c. These transmitted/scattered electrons are focused by the objective lens for imaging. With the help of the intermediate lens and the projector lens, TEM images will be obtained.

There are two working methods for TEM, the imaging mode and diffraction mode, as shown in Fig.2.3(a) and (b). The diffraction pattern is formed in the back focal plane by the objective lens, and the image generates in the image plane (it is called intermediate image). The imaging and diffraction modes are changed by the intermediate lens, as the focusing of the intermediate lens can adjust the image or diffraction pattern showing in the second intermediate image, then magnified by the projective lens. Finally, the image or diffraction pattern is present on the screen, or recorded by the camera. In this study, the TEM images which represent the atomic structure of samples are obtained by imaging model and recorded by a CCD camera.

To obtain the atomic structure of samples, high-resolution transmission electron microscopy (HR-TEM) is used in our experiments. The imaging contrast of HR-TEM is origin from the interference between scattered electron waves with transmitted electron wave. For the very thin sample, it can be treated as an object that the amplitude of the incident electron wave is not changed but the phase of the wave slightly changed

after the interaction. In this case, due to the interaction between sample and incident electron wave, and the interference of the electron exit waves, the phase change that occurred is relative to the incident wave peaks at the location of the atomic columns. By recording the amplitude of the phase interference, the HR-TEM image is recorded with a CCD camera, it is represented the projected structure of sample.

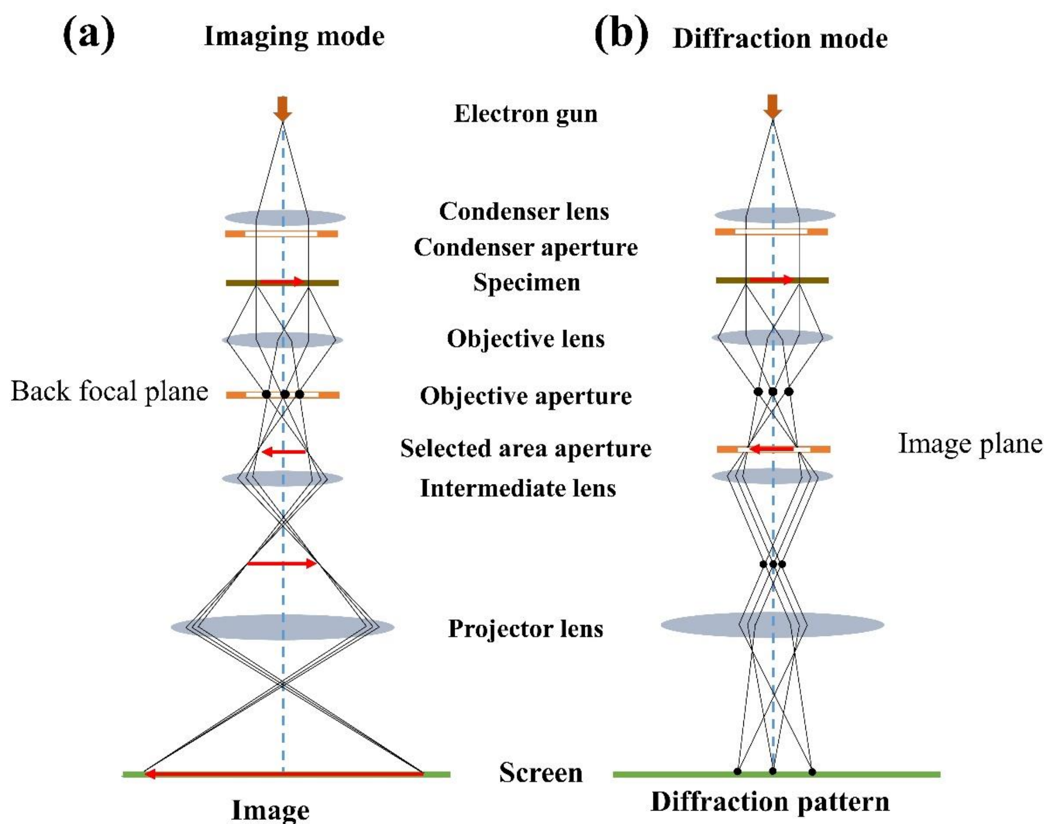


Figure 2.3. Schematic of the imaging mode (a) and diffraction mode (b) of TEM. Imaging/diffraction mode is adjusted when the image/diffraction pattern is showing in the plane of the second intermediate image by adjusting the intermediate lens.

### *2.1.3 The geometric phase analysis of TEM image*

The atomic image can be obtained by HR-TEM, which makes the possibility to reveal the structural deformation of materials on an atomic scale. To obtain the atomic-scale structural deformation (strain) mapping, we introduce the geometric phase analysis (GPA) [60,61] method to the HR-TEM images. The basic principle of GPA is that the displacement of the lattice can be measured by calculating the Fourier components of the lattice fringes in the HR-TEM image, therefore, the corresponding strain map can be revealed.

The intensity of an HRTEM image, $I(\boldsymbol{r})$, can be described as:

$$I(\boldsymbol{r}) = \sum_{g} I_g(\boldsymbol{r}) e^{2\pi i g \bullet \boldsymbol{r}} \ , \qquad (2.2)$$

where, $\boldsymbol{g}$ are the reciprocal lattice vectors of the lattice without distortion. The local Fourier components can be obtained as:

$$I_g(\boldsymbol{r}) = A_g(\boldsymbol{r}) e^{iP_g(\boldsymbol{r})} , \qquad (2.3)$$

where, $A_g(r)$ is the amplitude that indicates the local contrast, $P_g(r)$ is the phase that indicates the position. The phase is representing to the displacement field $\boldsymbol{u(r)}$ of the lattice, as following:

$$P_g(\boldsymbol{r}) = -2\pi g \bullet \boldsymbol{u}(\boldsymbol{r}) \ . \qquad (2.4)$$

Therefore, by measuring two different phases, such as $P_{g1}(r)$ and $P_{g2}(r)$, which present two different reciprocal lattice vectors of the image, the 2D displacement field

is determined as:

$$\boldsymbol{u(r)} = -\frac{1}{2\pi}[P_{g1}(\boldsymbol{r})\boldsymbol{a}_1 + P_{g2}(\boldsymbol{r})\boldsymbol{a}_2], \tag{2.5}$$

where, $\boldsymbol{a}_1$ and $\boldsymbol{a}_2$ are the basis vectors of the lattice in real space corresponding to the $\boldsymbol{g}_1$ and $\boldsymbol{g}_2$. Then, the strain field can be retrieved from the gradient of the displacement field:

$$\varepsilon = \begin{pmatrix} \varepsilon_{xx} & \varepsilon_{xy} \\ \varepsilon_{yx} & \varepsilon_{yy} \end{pmatrix} = \begin{pmatrix} \frac{\partial u_x}{\partial x} & \frac{\partial u_x}{\partial y} \\ \frac{\partial u_y}{\partial x} & \frac{\partial u_y}{\partial y} \end{pmatrix}. \tag{2.6}$$

Thus, the 2D strain map on atomic scale can be retrieved from the HR-TEM image. In this study, we can reveal the deformation of the atomic structure during the in situ TEM observation by applying the GPA on the HR-TEM images.

### *2.1.4 The influence of thickness on the visibility of HR-TEM image*

Generally, the HR-TEM image represents the projection of the electrostatic potential ($\varphi(\boldsymbol{r})$) of atoms making up the crystal [58], that is, intensity of the HR-TEM image is related to the projected electrostatic potential ($\varphi'(\boldsymbol{r})$) along the parallel direction to the incident electron beam. The projected electrostatic potential is related to the electrostatic potential and the thickness of the sample ($t$), and can be described as:

$$\varphi'(\boldsymbol{x}, \boldsymbol{y}) = \int_0^t \boldsymbol{dz}\varphi(\boldsymbol{x}, \boldsymbol{y}, \boldsymbol{z}). \tag{2.7}$$

And the intensity of HR-TEM image ($I(\boldsymbol{r})$) can be expressed as following:

$$\boldsymbol{I}(\boldsymbol{r}) = 1 - 2\sigma\varphi'(\boldsymbol{r}), \tag{2.8}$$

where σ is the interaction constant between sample and the electrons. Therefore, the changes in the thickness will result in the modulation of the (*φ'(**r**)*), correspondingly, the intensity of the HR-TEM image is modulated. Previous report has shown that the intensity of the N and Al column in the HR-TEM images increased with increasing thickness [62].

Thus, the changes in the intensity of HR-TEM image will result in the changes in the visibility of the sample. Hence, the visibility of the HR-TEM image is defined as the function of the intensity of atomic column ($I_{max}$) and the spacing between atomic column ($I_{min}$). The visibility of the atomic column ($Vis_{Atom}$) is described as:

$$Vis_{Atom} = \frac{I_{max} - I_{min}}{I_{max} + I_{min}} . \tag{2.9}$$

As shown in the Fig.2.4(a), the simulated HR-TEM images of the sample shows a contrast of lattice, and the corresponding intensities was obtained from the profile of the marked region, as shown in Fig.2.4(b). We should also notice that there is a Fresnel fringes appears in the edges of the sample, as shown in both Fig.2.4(a) and (b), the visibility of the Fresnel fringes ($Vis_{Fres}$) can be described by the bright ($I_F$) and dark ($I_D$) intensity of the Fresnel fringes, as following:

$$Vis_{Fres} = \frac{I_F - I_D}{I_F + I_D} . \tag{2.10}$$

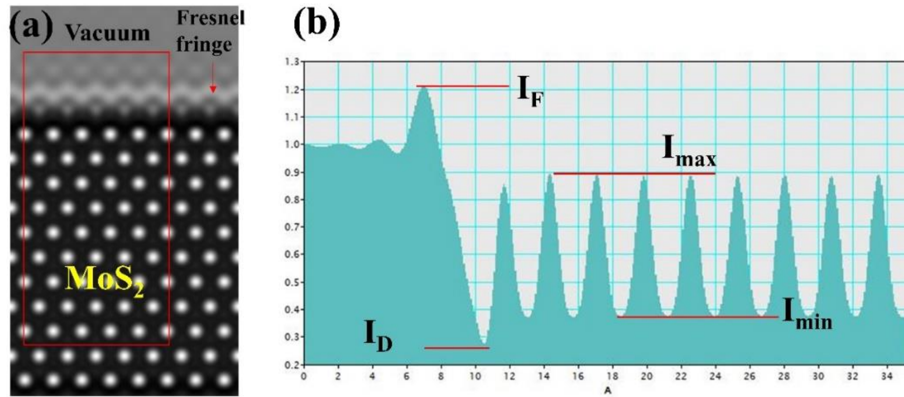


Figure 2.4. (a) The simulated HR-TEM image of $MoS_2$, with a thickness of 4.92 nm, and focus of -55 nm. (b) Profile of the HR-TEM image marked with red frame in (a).

According to the Eq. (2.8), the intensity of HR-TEM image is modulated with the thickness, obviously, the intensity of the columns and the Fresnel fringes will change. Thus, both the $Vis_{Atom}$ and $Vis_{Fres}$ are sensitive to the thickness.

To estimate the thickness of $MoS_2$ layers by the visibilities, we simulated HR-TEM images with different layers (thickness) of $MoS_2$ crystal. The simulation conditions were set to be the same as the observation ones: with the accelerating voltage of 200 kV, the spherical aberration of 0.7 mm, beam convergence of 3.4 mrad, defocus value of -55 nm (under-focus). The thickness of the $MoS_2$ layers were range from 1 to 10 layers. The visibilities were calculated based on the Eqs. (2.9) and (2.10), and the relationship between the visibilities and the thickness (number of layers) of $MoS_2$ layers is shown in Fig.2.5. Consequently, the number of layers (thickness) of the $MoS_2$ layers can be identified based on such a relationship.

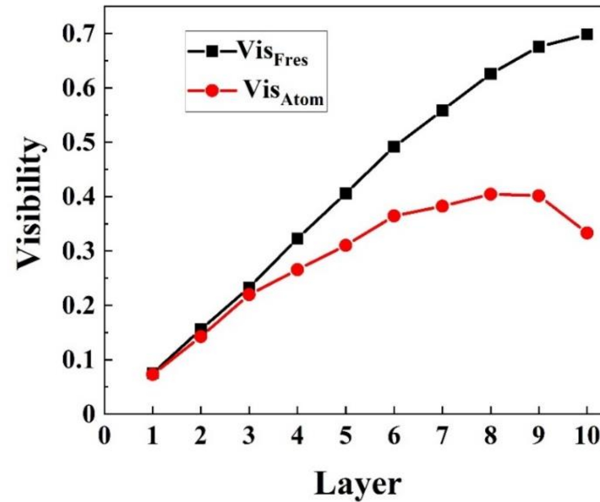


Figure 2.5. Relationship between visibilities and the number of layers of $MoS_2$.

## 2.2 Fabrication process of Si chip for 2D material

To mount the 2D materials for the experiment, a Si chip is introduced for providing a flat surface on atomic scale. The fabrication process of the Si chip consists of a standard electron beam lithography (EBL) process, the wet etching process, the dry etching process, and the electron beam deposition (EBD) process.

### *2.2.1 The experimental equipment used in the fabrication process*

**EBL system**

The EBL process is carried out with the EBL machine (ELIONIX, ELS-3700), as shown in Fig.2.6. The EBL is used to produce the designed pattern on the sample by using a focused beam of electrons. The surface of the sample is covered with the electron-sensitive film (which is called a resist, and here we using Polymethyl methacrylate: PMMA), the solubility of the PMMA changed with the electron exposure.

Then the exposed regions of PMMA can be removed by solvent, and the designed patterns are shown.

Figure 2.6. Photograph of Electron Beam Lithography system (ELS-3700, ELIONIX).

**Dry etching system**

The dry etching is carried out with the reactive ion etching system (RIE-10NR, SAMCO), as shown in Fig.2.7. In the dry etching process, the active plasma is generated by the electromagnetic field and it is used to remove specific materials. In our experiment, dry etching is used to remove the $Si_3N_4$ film on the surface of the Si chip for the further etching.

Figure 2.7. Photograph of the reactive ion etching system (RIE-10NR, SAMCO).

**EBD system**

EBD is a deposition method by using electron beams to evaporate the target materials. In our experiment, the EBD system (MUE-ECO-EB, ULVAC) is used to deposit the chromium/gold (Cr/Au) on the Si chip to fabricate the electrodes, as shown in Fig. 2.8.

Figure 2.8. Photograph of the EBD system (MUE-ECO-EB, ULVAC).

### *2.2.2 The overall fabrication process of Si chip*

The Schematic fabrication process of the Si chip is shown in Fig.2.9. The Si wafer (<100>, N-type, 0.2 mm of thickness) with 50nm silicon nitride ($Si_3N_4$) is used to fabricate the Si chip,

The detailed process is described as follows.

1. Substrate cleaning. The Si wafer is cleaned with solutions in the order of isopropyl alcohol (iPA), acetone, and deionized water, each for 3 min.

2. PMMA coating. The cleaned substrate is coated with PMMA by spin coating,

the spinning speed is 4000 rpm, and the time is 60 s. Then, it is baked with 180 °C for 5 min.

3. EBL process. The EBL system (ELS-3700, ELIONIX) is used in this process, with the beam current ($I_{beam}$) of 1.5 nA, and the dose time ($t_{dose}$) of 7 s. The accelerating voltage of the electron gun is 30 kV, the scan area is 500 $\mu m^2$, and the size of a dot is 25 nm, and the Pitch is 4. After the pattern is drawn by EBL, the development is carried out in the solution of methyl isobutyl ketone (MIBK) and iPA. It is developed with the solutions in the order of MIBK:iPA=1:3, MIBK:iPA=1:1, for 2min and 20 sec, respectively. Finally, it rinses with iPA for 45s.

4. Dry etching. The dry etching is performed with the reactive ion etching system (RIE-10NR, SAMCO) to remove the $Si_3N_4$ membrane for patterning. The etching is carried out with the carbon tetrafluoride ($CF_4$, 20 sccm) gas, operated with a pressure of 4 Pa, the power of 30W for 2 min.

5. Wet etching. The wet etching is performed with KOH solution (33 wt%, Kanto chemical) to make a trench in the Si chip. The KOH solution is maintained with a temperature of 80°C and lasts for 4h. The etching occurrs at the region where $Si_3N_4$ membrane is etched in the dry etching process. Due to the anisotropic etching rate of the Si, in which the (111) plane shows the lowest

etching rate, a trench with a slop of (111) plane is fabricated, as shown in Fig.2.9.

6. EBD process. It is an optional process and specific for fabricating Au electrodes on the Si chip for the conductance measurement. The electrodes deposit on the Si chip are performed by the EBD system (MUE-ECO-EB, ULVAC). Firstly, a Cr layer is deposited, 5 nm thick with a 1.0 Å/s deposition rate, as the adhesion layer. Secondly, the Au layer is deposited, 40 nm in thickness at a deposition rate of 2.0 Å /s.

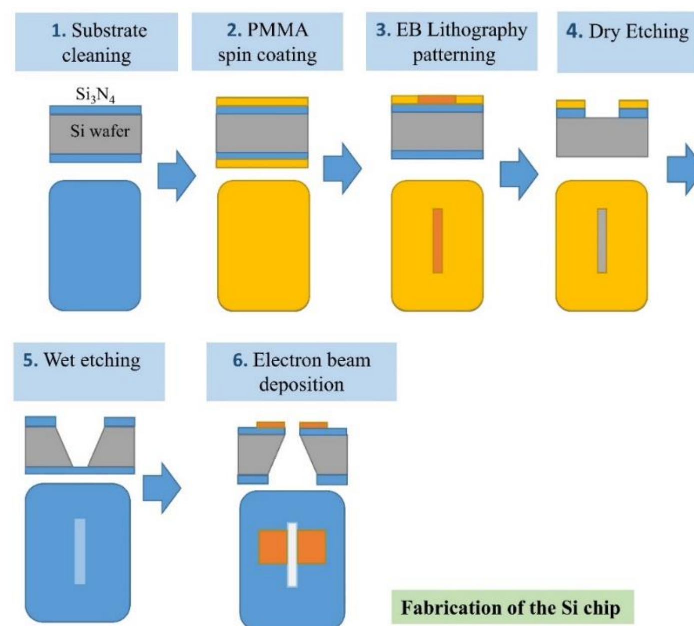


Figure 2.9. Schematic of the fabrication process of the Si chip.

After the fabricating process, the Si chip with a trench is prepared, a Si chip mounts on TEM holder is showed in Fig.2.10(a). The width of the trench can be achieved to ~5

μm by the wet etching. The Si chip can be cracked along the trench by applying stress, the cracked region can also act as the trench for stretching the 2D materials, as shown in Fig.2.10(b).

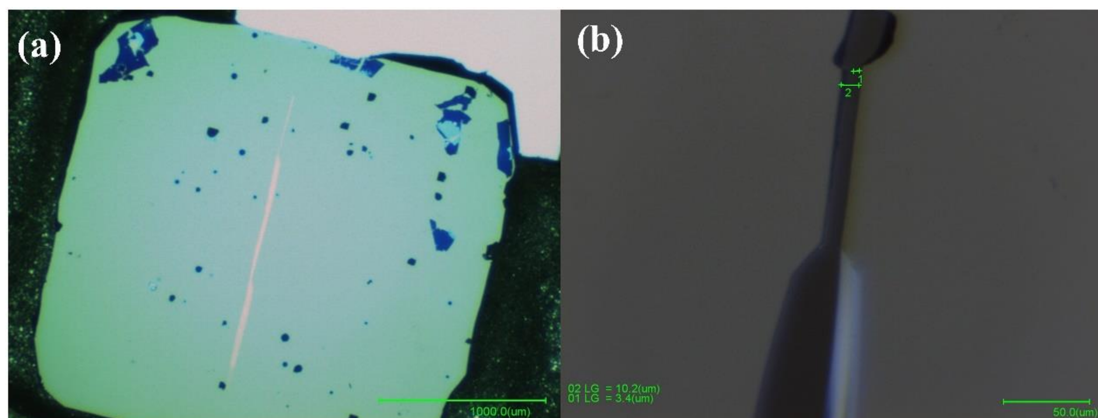


Figure 2.10. Photograph of the Si chip. (a) Si chip with a trench. (b) Si chip after cracking, mark 1 and 2 indicate the initial and stretched width of the cracked trench, respectively.

## 2.3 Sample preparation and transfer

The $MoS_2$ nanosheet is prepared with the mechanically exfoliate method [63,64], in which the natural $MoS_2$ is exfoliated by scotch tape. Then, the target sample is transferred to Si chip by the dry transfer method [65,66].

### *2.3.1 Preparation*

The natural $MoS_2$ (produced in Shirakawa) bulk is used for preparing the sample,

as shown in Fig. 2.11 (a). The $MoS_2$ is exfoliated with the tape (Nitto) several times, as shown in Fig. 2.11 (b). Then, the $MoS_2$ flake is transferred on a polydimethylsiloxane (PDMS, Gel-Pak) stamp, as shown in Fig. 2.11 (c)-(d).

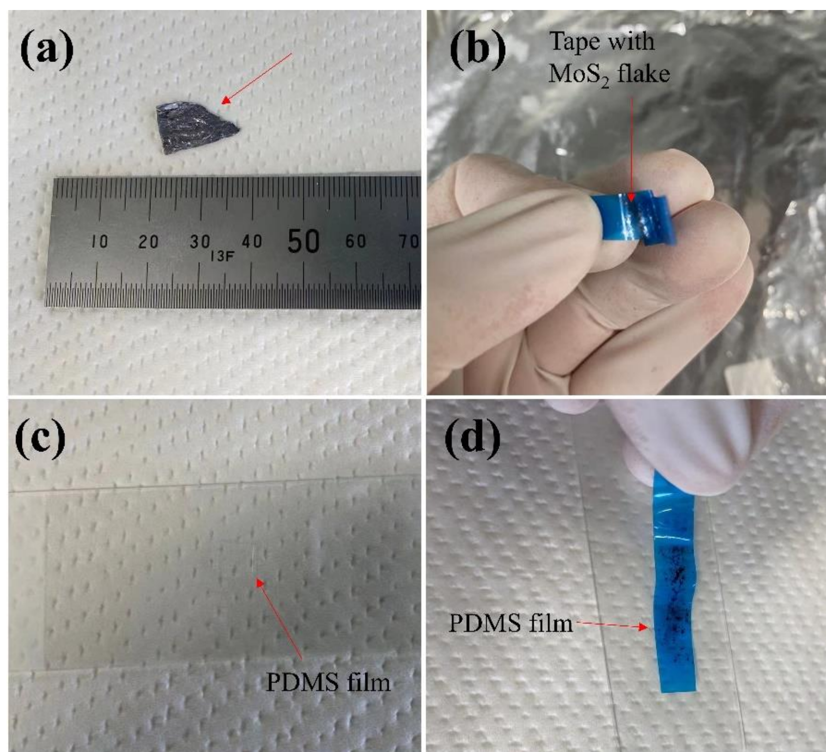


Figure 2.11. Mechanical exfoliation of $MoS_2$. (a) Photograph of the natural $MoS_2$ bulk. (b) Exfoliating the $MoS_2$ flake with tape. (c) PDMS stamp on the glass slide. (d) Transferring $MoS_2$ flake on PDMS stamp.

The optical microscope (Axis Pro2, Micro Support) is used to check and select the target sample, as shown in Fig.2.12(a). The PDMS with $MoS_2$ flake is mounted on the manipulator of the optical microscope, as shown in Fig.2.12(b), for assessing the thickness of the sample.

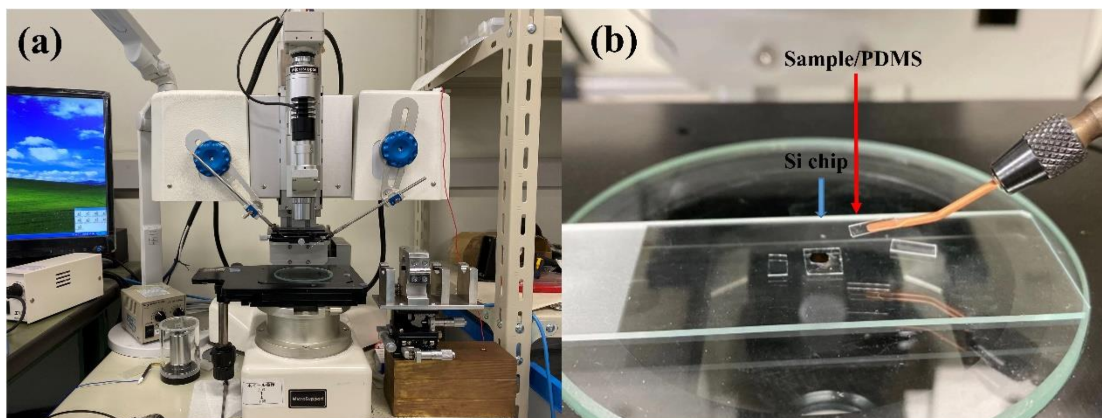


Figure 2.12. (a) Photograph of the optical microscope. (b) Checking of the sample.

### *2.3.2 Dry transfer process*

After the $MoS_2$ flake is prepared and inspected, the target sample can be transferred on Si chip by controlling the movement of the manipulator, as shown in Fig.2.13. The dry transfer process is described as follows.

1. Assessing and focusing the target sample on the PDMS stamp with the optical microscope.

2. Moving the target sample to the top of the Si chip, then aligning the sample to the target Si chip.

3. Focusing on the Si chip and lowering the height of sample/PDMS, approaching the sample to the Si chip slowly.

4. Making the contact between the Si chip and the sample/PDMS.

5. Removing the PDMS stamp slowly, the sample is transferred on the Si chip.

After the transfer process, the sample, which is mounted on the Si chip in the holder should be baked for removing the contaminants, then, it can be observed in TEM.

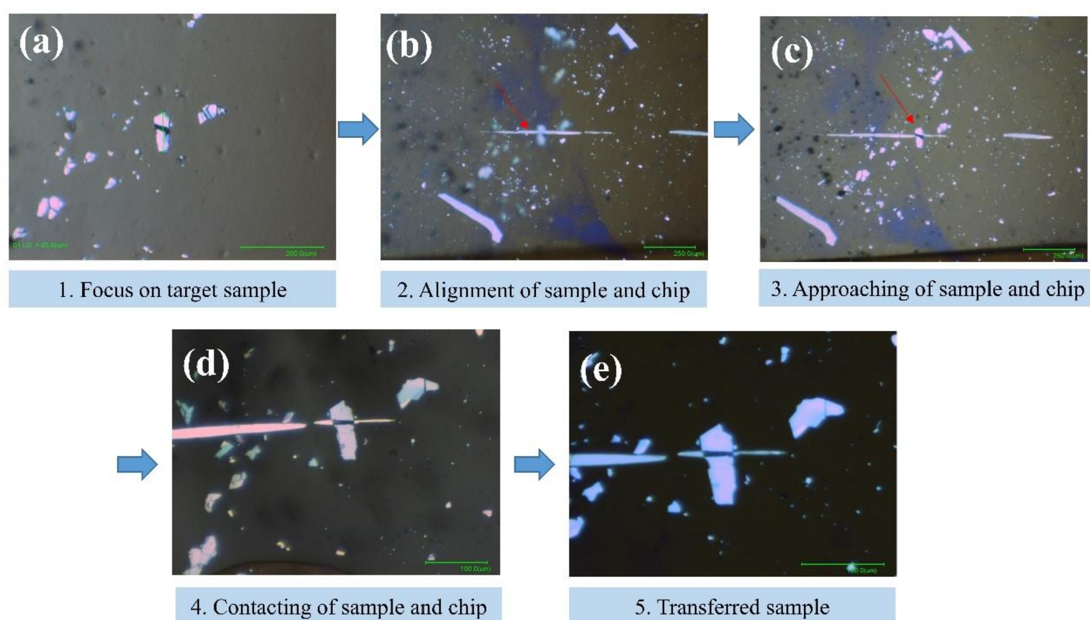


Figure 2.13. The transfer process. (a) Assessing and focusing on the target sample. (b) Alignment of target sample to the Si chip. (c) Approaching of the sample to the Si chip. (d) Contacting of the sample and Si chip. (e) Removing the PDMS stamp.

## 2.4 Conclusion

In this chapter, we have introduced the mainly experimental methods used in the work of this thesis, for the better understanding of our experimental results.

The principle of the transmission electron microscopy is introduced. The basic component and the imaging methods of TEM are present. Then the principle of high-resolution TEM is also explained, and the corresponding GPA of the HR-TEM image is introduced for retrieving the strain distribution on atomic scale. The relationship between the thickness (number of layers) of $MoS_2$ and visibilities of HR-TEM image are also revealed.

The fabrication process of the Si chip is introduced. The Si chip is specific fabricated for the stretching and TEM observation of the 2D materials. The related experimental methods are also discussed.

Finally, the sample preparation and transfer process is explained. The sample is prepared with the mechanical exfoliate method, and transferred on Si chip by the dry transfer method.

# Chapter 3 Development of stretching TEM holder for 2D materials

## Introduction

This chapter introduces the development of stretching TEM holder for 2D materials. In Chapter 3.1, we describe the design of the in-situ stretching TEM holder and clarify the working mechanism of stretching. In Chapter 3.2, we carry out the in-situ testing of the stretching holder. The stability and stretching ability of the holder are characterized, the corresponding atomic TEM image and linear relationship between applied bias voltage and gap distance are revealed. In Chapter 3.3, the conductance measurement system is introduced.

## 3.1 The design of the in situ stretching TEM holder

As for an in situ stretching TEM holder for 2D materials, it should be mechanically stable that can obtain the atomic image, proving the mechanical force for stretching sample and a flat surface for placing the 2D sample.

Considering the planar structure of 2D materials, we introduced a Si chip, which can provide a flat surface, to mount the sample for the stretching of 2D materials. The Si chip is fabricated with a trench by the etching method, and the sample is suspended across the trench. It means the strain can be applied to the sample by stretching the trench. In the meanwhile, the gold (Au) electrodes can be fabricated on the surface of the Si chip, for the measurement of electrical conductance. For the stretching of the Si chip, a titanium (Ti) plate is used for generating the planar deformation. To obtain an atomic-scale resolution, the stretching process should be stable. Therefore, we use a piezo actuator for introducing the displacement during stretching, as it is more controllable and stable at small displacement than the mechanical one.

Thus, the holder consists of four parts, the frame, the Ti plate, the piezo actuator, and the Si chip. The design of the stretching holder is shown in Fig. 3.1. Such a specific design is made for the purpose of stretching for 2D materials.

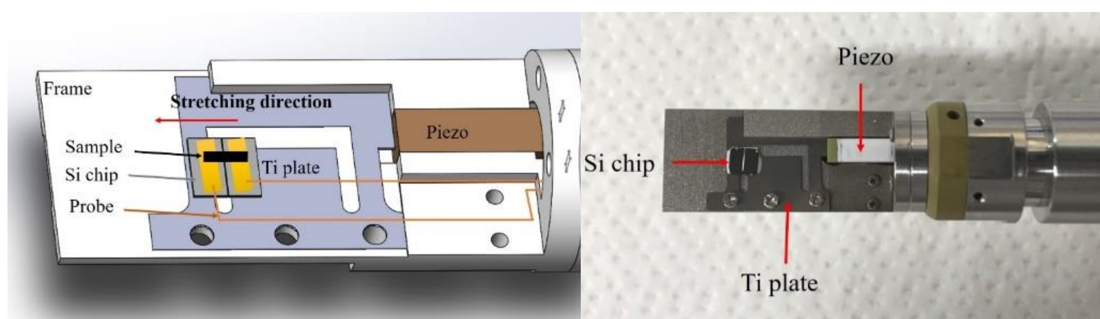


Figure 3.1. Diagram (left) and photograph (right) of the stretching TEM holder.

The assemble of the stretching TEM holder is showed as the diagram in Fig. 3.1. The piezo actuator is fixed with the frame of holder and contact with the Ti plate, the Ti plate is mounted on the frame and fixed by three screws. The Si chip, which is etched with a trench, is mounted on the Ti plate with silver paste. The stretching is achieved by applying bias voltage on the piezo actuator, which the length is extended that generates a longitudinal displacement. Then, the piezo actuator drives the deflection of the left beam of the Ti plate, the motion of the Ti beam stretches the trench of the Si chip, correspondingly, both the trench of the Si chip and the sample across the trench are stretched.

In the stretching holder, the key is the deflection of the Ti plate, which drives the stretching of the Si chip and sample. Therefore, we simulate the deformation of the Ti plate under load by the software Ansys 2019, as shown in Fig. 3.2. With the load from the piezo actuator applying from the right side and the bottom is fixed with screws, the deformation of the Ti plate differs in parts that can lead to the stretching. As we can see

the simulated deformation with a 1 N load in Fig. 3.2, the deformation of the position 1 is zero, while it deforms in the position 2, it means the left beam moves to the left side and the central part keeps static that result in a stretching between the position of 1 and 2. The simulation result indicates our design works.

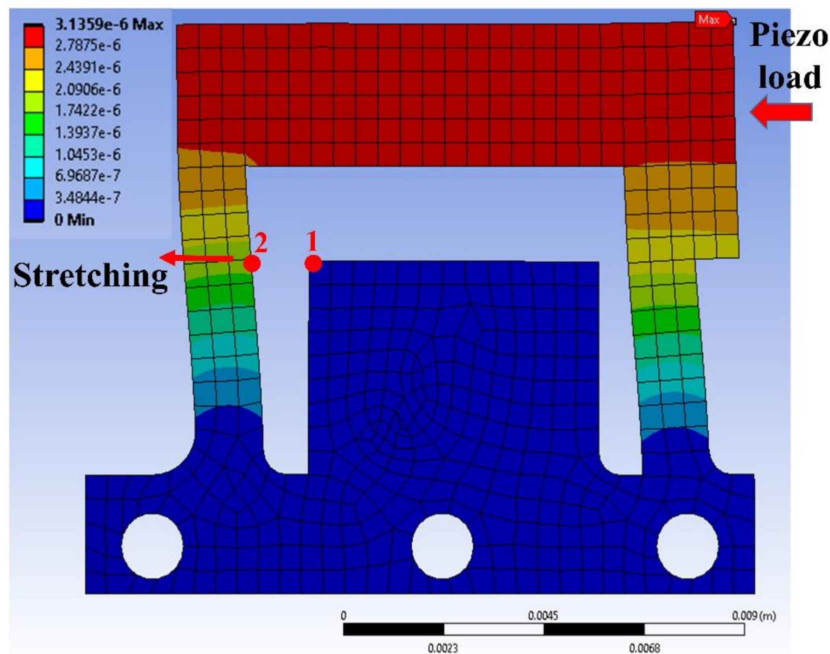


Figure 3.2. Deformation of Ti plate under load. Simulated by the software Ansys 2019 with a load of 1 N on the right side marked with the red arrow, the fixed positions are the three screw holes in the bottom. The color bar indicated the deformation.

## 3.2 The calibration of the in situ stretching TEM holder

With the TEM holder assembled, we carried out the calibration experiments for evaluating its performance during the in situ stretching. The motion of the stretching

holder was combined with a piezo actuator and a piezo driver. The piezo actuator (KEMET AE0203D16DF, YAGEO company) was used in our holder, it can work with a maximum voltage of 150 V (DC) and a corresponding maximum displacement of 17.4 μm. A piezo driver was used to drive the piezo actuator (MESS-TEK, M-2680), as shown in Fig. 3.3, it can control the applied voltage with a minimum step of 1 mV that adjust the strain rate during the stretching.

Figure 3.3. Photograph of the piezo driver.

The stretching test was performed with the Si chip which contains an open trench (85 μm wide). By recording the image of the trench with different applied bias voltage on piezo, as shown in Fig. 3.4. In the TEM holder, the gap distance changed in proportional to the applied bias voltage, which was from the initial 85 μm to 102 μm

when the voltage was 142 V. By recording the bias voltage and corresponding trench width, the relationship between the displacement of the trench and applied voltage was obtained, as shown in Fig. 3.5.

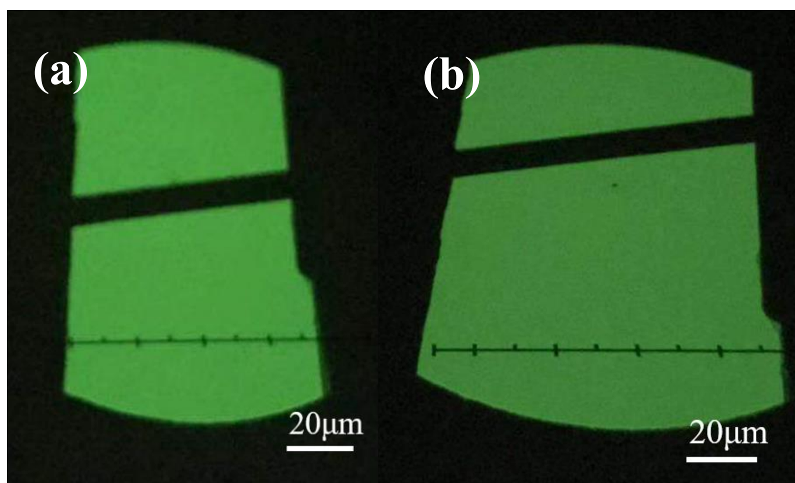


Figure 3.4. (a)-(b) Image of the trench with the applied bias voltage of 0 V and 143 V, respectively.

The relationship between trench width and the applied bias voltage was linear, it indicating that the holder was effective for stretching.

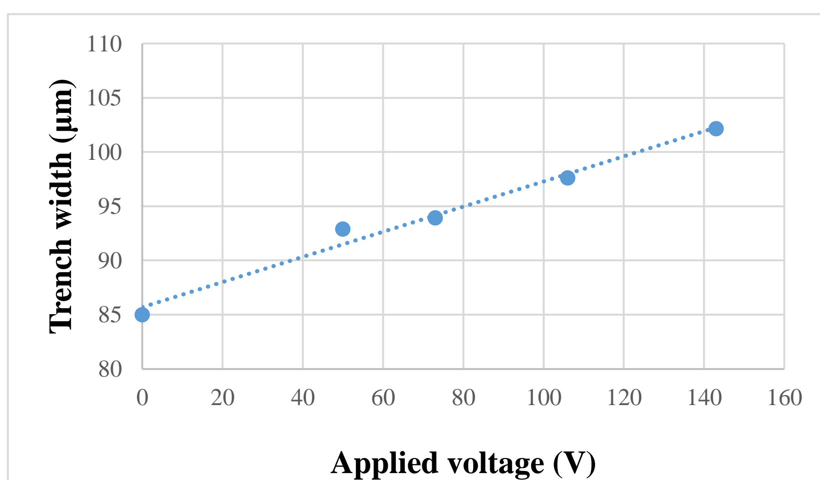


Figure 3.5. Relationship between trench width and applied bias voltage.

In order to characterize the stability of the TEM holder, which is a key factor for obtaining the atomic image, we carried out an in situ stretching test of a gold (Au) wire, as shown in Fig. 3.6. The fast Fourier transform (FFT) pattern indicating a [110] zone axis of Au. The TEM image showed clear atom contrast, which means the holder is stable for the atomic-scale observation.

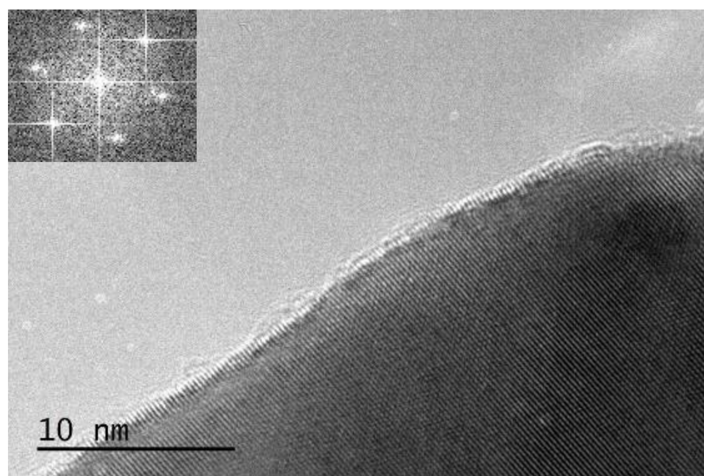


Figure 3.6. Atomic TEM image of Au wire. Inset is the corresponding FFT pattern, indicating a [110] zone axis.

To characterize the displacement step during the stretching, we recorded the position of the tip of the Au wire and the corresponding applied bias voltage. As shown in Fig. 3.7, it showed a displacement of ~60.0 μm within 1 V applied voltage, implied a displacement step of 16.7 mV per nm. With the minimum step of 1 mV of the piezo driver, the minimum displacement step can achieve to 0.06 nm, such a step is applicable for stretching on atomic scale.

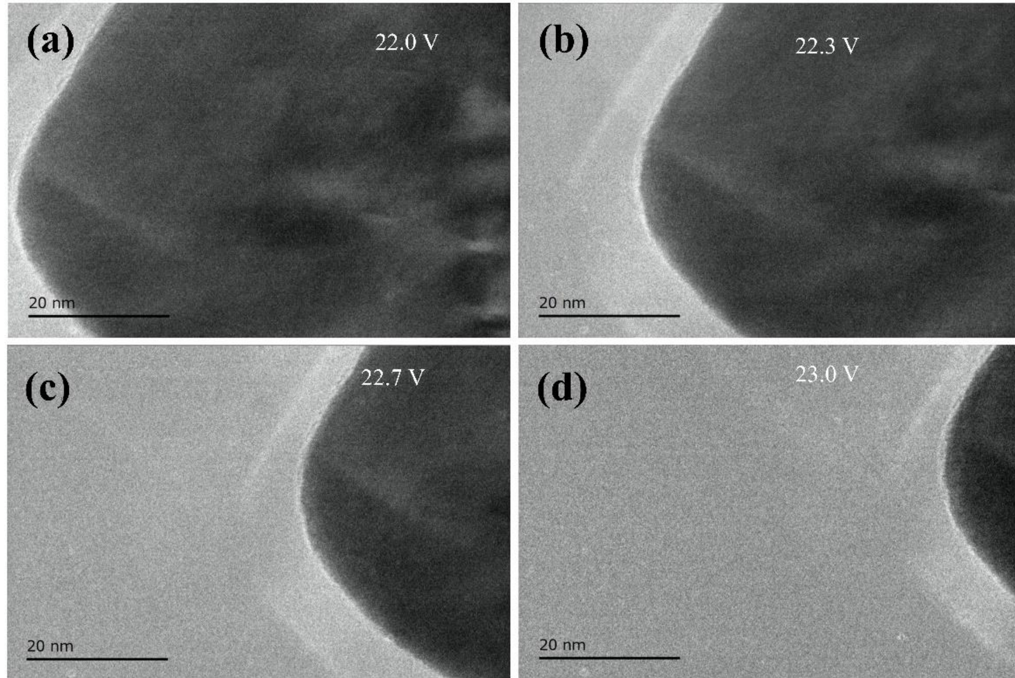


Figure 3.7. (a)-(d) TEM image of the tip of Au wire with applied bias voltage of 22.0V, 22.3V, 22.7V, and 23.0V.

### 3.3 Electrical conductance measurement

The conductance measurement of 2D materials can be performed at the same time during the stretching measurement. As the Au electrodes are fabricated on the Si chip, by contacting the conductance wires to the electrodes, the conductance of 2D materials can be measured. The electrical conductance measurement system consists of the Source Measurement Units (Keithley Model 2635A) and the test LabVIEW program, as shown in Fig.3.8. The measurement system can perform the measurement on the resistance and the current-voltage characteristic curve (I-V curve).

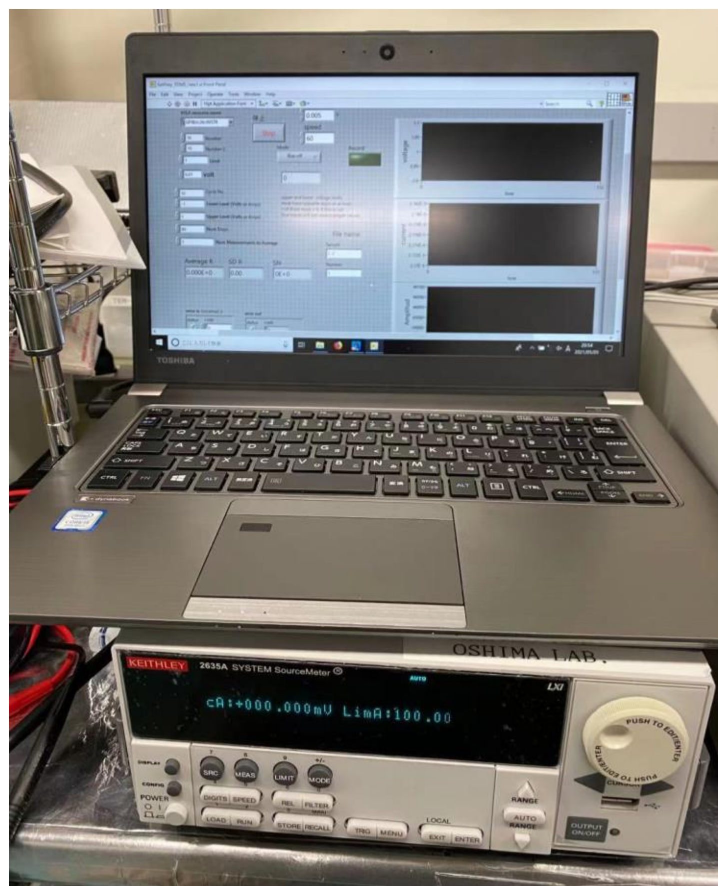


Figure 3.8. Photograph of the electrical conductance measurement system.

Applying strain can modify the electronic properties of 2D materials, since it changes the band structure that results in the change of the conductance behavior. Herein, we carried out experiments to measure the conductance behavior of $MoS_2$ flake during the stretching. The setup of the stretching TEM holder for measuring the conductance behavior of the $MoS_2$ flake is showed in Fig. 3.9(a). The sample was transferred across the trench, and attach with the Au electrodes on the Si chip, as shown in Fig. 3.9(b). The electrodes were in contact with the conductance wires for the measurement.

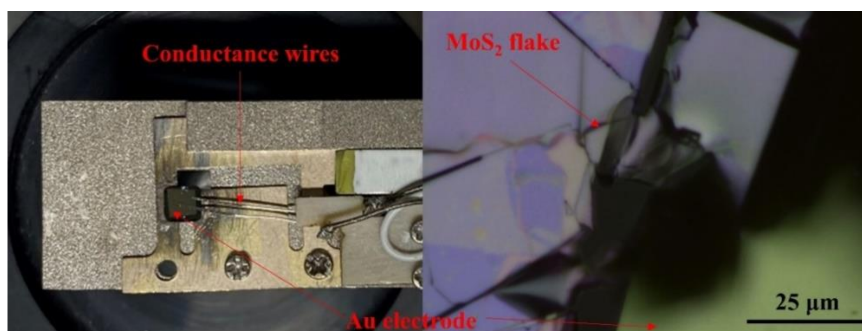


Figure. 3.9. (a) Image of the stretching TEM holder for 2D materials. (b) Optical image of the $MoS_2$ flake transferred on the Si chip mounted on TEM holder.

The relationships between the applied voltage and electrical current (the I-V curve) during stretching were measured, as shown in Fig.3.10. It is found that the conductance reduced with the increasing tensile strain. Such a phenomenon is not consistent with the previous report that the conductance increases with increasing strain, this situation might be originated from the contact resistance change during stretching.

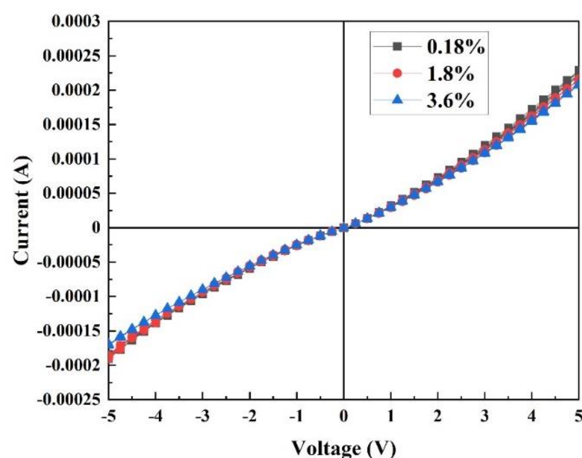


Figure.3.10. The relationships between the applied voltage and electrical current of the $MoS_2$ flake with the tensile strain of 0.18%, 1.8% and, 3.6%, respectively.

## 3.4 Conclusion

In this chapter, a stretching TEM holder was developed for the purpose of investigating the strain dependence of physical properties in 2D materials. The working method of the holder is introduced.

The design of the holder is introduced. The holder consists of four parts, the frame, the Ti plate, the piezo actuator, and the Si chip. The stretching function is performed with the piezo actuator, which generates a displacement by applied bias voltage and drives the motion of the Ti plate that stretching the trench in the Si chip. The Si chip was introduced for placing 2D materials and corresponding stretching and conductance measurement.

The in situ stretching experiment was carried out successfully for calibration. The atomic TEM images and linear relationship between applied bias voltage and gap distance indicated that it was stable and effective for the observation of 2D materials. The displacement step of the holder was measured, which is 0.06nm /mV. Our testing result indicating the stretching holder is applicable for stretching 2D materials on atomic scale.

The strain dependence of the conductance behavior of $MoS_2$ flake was measured with in situ TEM holder. The conductance of $MoS_2$ flake is found to be reduced with increasing tensile strain.

# Chapter 4 The stretching and fracture of $MoS_2$ nanosheet

## Introduction

This chapter contains the observation and analysis of the structure of the $MoS_2$ nanosheet by in-situ stretching TEM holder. The fracture and stretching of $MoS_2$ nanosheet are studied.

In Chapter 4.1, we show the TEM observation of the $MoS_2$ nanosheet, its atomic structure is revealed. In Chapter 4.2, we show the structural modulation of $MoS_2$ nanosheet under a small strain condition. In Chapter 4.3, we show the results of in situ stretching $MoS_2$ nanosheet, and the fracture mechanism is investigated.

## 4.1 The structure of the of $MoS_2$ nanosheet observed in TEM.

With our developed TEM holder, the suspended $MoS_2$ nanosheet can be observed with/without the strain condition. The $MoS_2$ nanosheet was prepared by mechanical exfoliation and transfer on the Si chip by the dry transfer method, as described in Chapter 2. The sample was suspended between the trench after being transferred on the Si chip, as shown in Fig. 4.1. The width of the trench in Si chip where the sample mounted was ~5 μm.

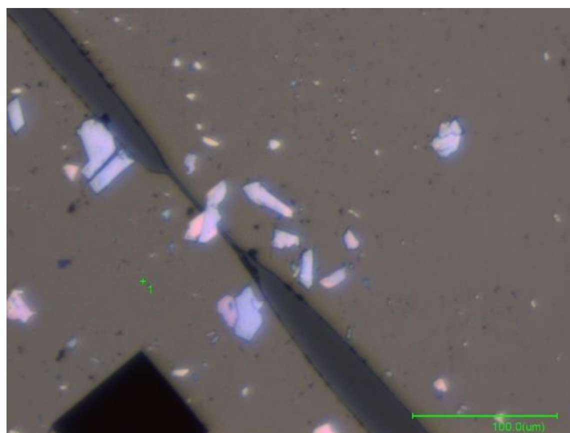


Figure 4.1. Optical image of $MoS_2$ nanosheet suspended across the trench of the Si chip.

After baking in the vacuum for 48 h, the sample was observed in UHV-TEM for TEM observation. Fig. 4.2 shows the typical TEM image of $MoS_2$ at low and high magnification. The TEM image shows that the $MoS_2$ nanosheet is suspended across the trench, as shown in Fig. 4.2 (a). The dark contrast region corresponds to the Si chip. The high magnification image shows clear atom columns, as shown in Fig. 4.2 (b). The FFT pattern shows a hexagonal pattern viewing from the [001] zone axis of $MoS_2$ layers.

In the TEM image, we observe contrast of contaminant, which is probably adsorbed on the nanosheet when transferring by PDMS. Since the contrast of contamination is relatively sharp (not blurred), the nanosheet is thought to be only a few layers in thickness. Actually, the thickness could be confirmed to be 2.5 nm (four layers) by estimation of the visibility (0.265±0.05).

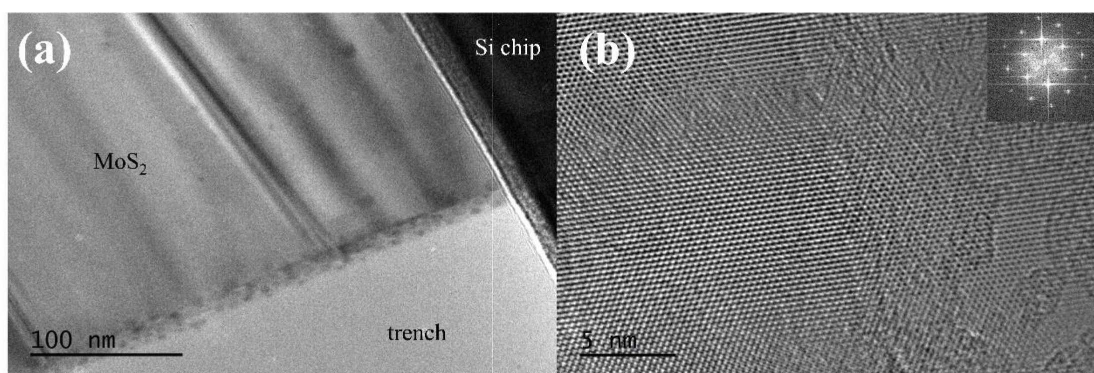


Figure 4.2. TEM image of $MoS_2$ nanosheet with low magnification (a) and high magnification (b), inset is the corresponding FFT pattern.

In the dry transfer method, when transferring the nanosheet adsorbed on PDMS to the Si chip, it is necessary to press the nanosheet strongly against the chip. Such press results in the stress left in the nanosheet and lead to the deformation after the transfer. Actually we often observed Moiré patterns in the nanosheet, as shown in Fig. 4.3. The Moiré patterns are original from the superposition of two different lattices, which have a suitable mutual orientation but a small difference in lattice spacing with each other. The appearance of Moiré patterns indicates there is a lattice mismatch or orientation

difference between the layers of $MoS_2$ nanosheet. The Fig. 4.3 (a) shows that the lattice mismatch/orientation difference in the $MoS_2$ layers were not uniform. The high magnification TEM image, which was taken at the region marked by red rectangle in Fig.4.3(a), did not show Moiré patterns and its FFT pattern was a single hexagonal pattern, indicating there is no lattice mismatch or orientation difference, as shown in Fig.4.3(b). At the edge region, The TEM image of more complicated Moiré patterns was obtained as shown in Fig. 4.3(c). Its FFT patterns consisted of two sets of hexagonal patterns with a rotation angle of 12°, which means that the rotation has occurred between the layers of the sample. The mismatch and rotation between layers may be caused by the transfer process, considering the layered structure of $MoS_2$ has weak interlayer interaction.

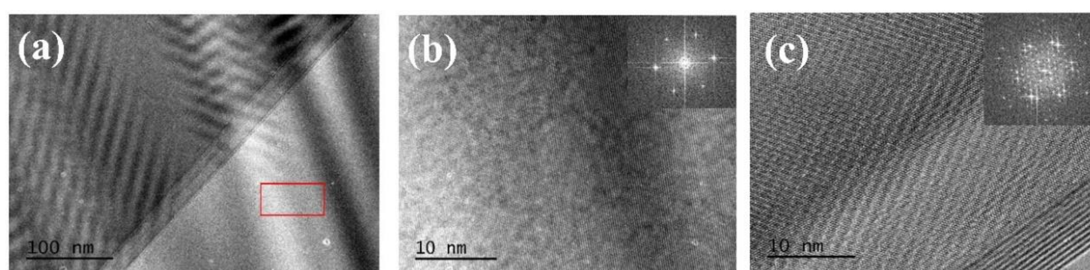


Figure 4.3. TEM images of $MoS_2$ nanosheet with Moiré patterns. (a) Low magnification image in the central part of the sample. (b)High magnification image of the marked region in (a). (c) High magnification image of the sample near the edge. Insets are the corresponding FFT patterns.

Meanwhile, we notice that the samples, which were obtained by the exfoliated

$MoS_2$ film, have a tendency to be stepped structure with zigzag edges, as showed in Fig. 4.4 (a)-(d). It suggests that the zigzag edge is more easily formed by the exfoliation. We think that the crack may propagate along the zigzag configuration more frequently than along the armchair configuration. Our experimental results agrees with the MD simulation result [67], in which the simulation was performed with a 50 × 50 nm monolayer $MoS_2$ model. They discussed about the energy release, which was defined as the total energy change per unit length of the crack. The energy release along the zigzag direction (2.09 eV/Å) was lower than the armchair direction (2.48 eV/Å), so that the crack propagation presented predominant zigzag edges, indicating that the crack is more easily propagated along the zigzag direction.

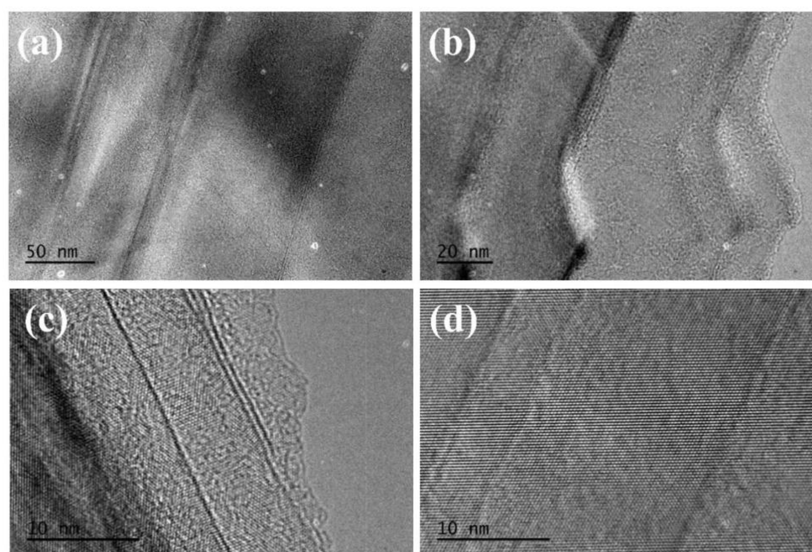


Figure 4.4. TEM images of $MoS_2$ nanosheet. (a)-(b) Low magnification images of the central region and the stepped structure. (c)-(d) High magnification image of the stepped edges and the central region.

Moreover, the stepped structures of the edge in Fig. 4.4 (b) and (c) demonstrate the interlayer fracture of $MoS_2$ layers. Such a phenomenon is conflicted with the previous report [68], in which the MD simulation results showed a brittle fracture of multiple layer $MoS_2$ (six layers or thicker) by assuming the combination between every layer is tight, the crack of fracture was penetrated layer by layer that is called intraplanar fracture. The difference between the report and our results should come from the pre-stretching conditions in the MD simulation, which assumed a strong interlayer interaction that the cracks could penetrate the adjacent layers. Our results showed clear stepped edges imply an interlayer fracture of $MoS_2$ nanosheet, such an interlayer fracture indicates the interlayer interaction between $MoS_2$ layers should be weak in the experiment.

### 4.2 The structural modulation of $MoS_2$ nanosheet under stretching

The structural response of the 2D materials under stretching is important for understanding their mechanical properties. To understand such kind mechanical response, the in situ stretching of the $MoS_2$ nanosheet with a small tensile strain (~0.7%) was performed.

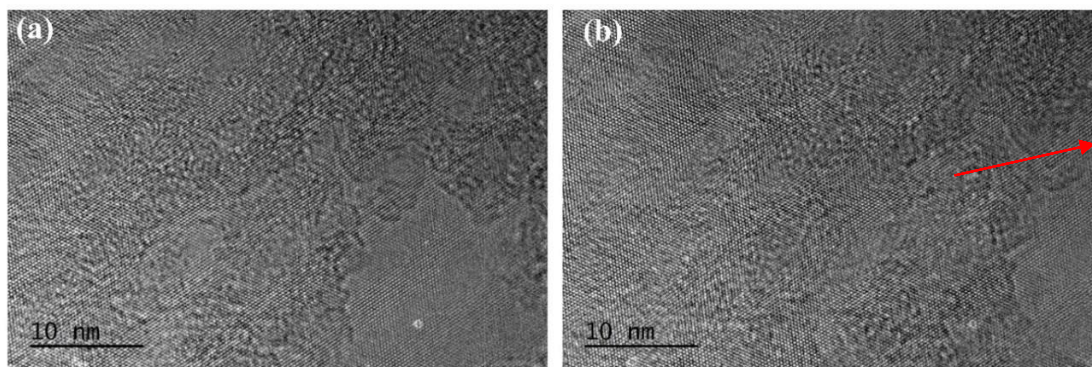


Figure 4.5. Atomic images of a three-layer $MoS_2$ nanosheet. (a) Before stretching. (b) Stretched with a ~ 0.7% tensile strain. The arrow indicates the stretching direction.

Figure 4.5 (a) and (b) show the atomic images of the $MoS_2$ nanosheet without and with stretching (0.7% tensile strain), respectively. The thickness of $MoS_2$ nanosheet was estimated to be 1.8 nm (three layers) according to the visibility of atomic columns. In order to reduce the contrast of contaminates which might be induced during the dry transfer process, we performed the fast Fourier transform (FFT) filtered process on the atomic TEM image, as shown in Fig.4.6 (a)-(b).

We found that the contrast of the sample was periodically modulated along the armchair direction of $MoS_2$ structure, which showed a clear/unclear contrast of atomic columns, as shown Fig.4.6(a). With applying a 0.7% tensile strain, the atomic contrast was modulated that the inverse contrast was occurred, as marked with the white and black dots in Fig.4.6 (b). The FFT patterns of the nearby regions, which were marked with white and black frames that corresponding to original and inversed atomic

contrasts, showed the same pattern. It suggests that such an inverse contrast should origin from the changes in focus due to the out-of-plane displacement.

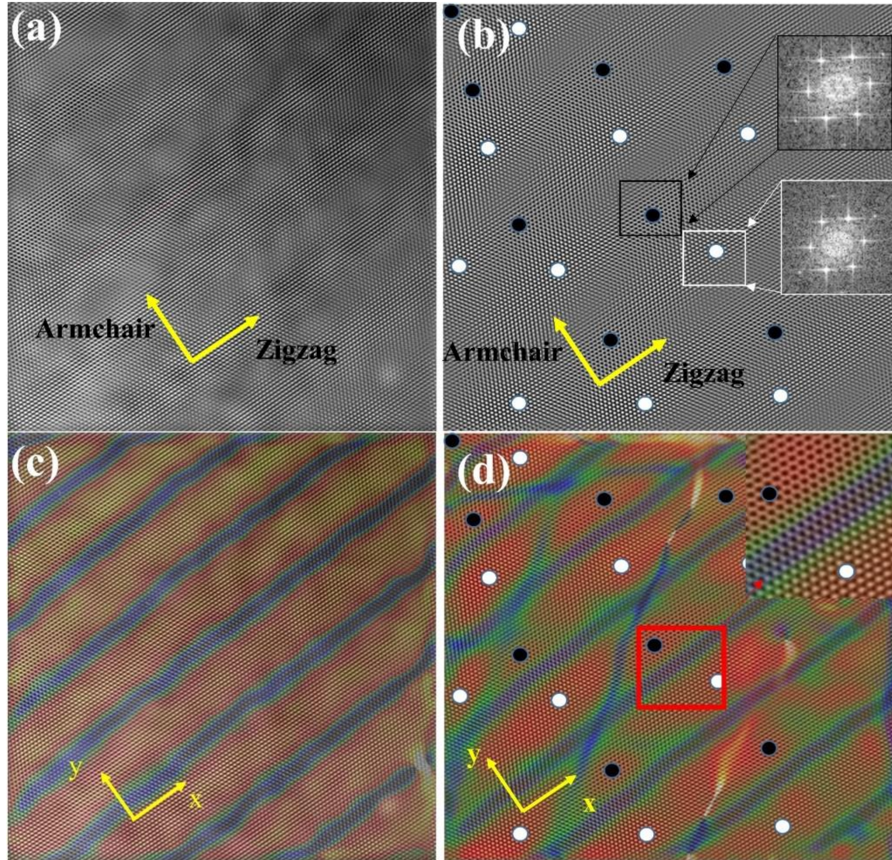


Figure 4.6. (a)-(b) Filtered HR-TEM images of the thin $MoS_2$ layers, corresponding to the Fig. 4.5 (a)-(b), respectively. The insets show the FFT pattern of marked regions. (c)-(d) Overlap of filtered TEM images and corresponding strain map ($\varepsilon_{yy}$) of (a) and (b), respectively, the inset is the enlarged image of the region marked with red box. The white and dark dots indicate the original and inverse contrast.

For the further analysis of the structural modulation, we carried out the GPA on the TEM images of Fig.4.6 (a) and (b) to obtain the strain ($\varepsilon_{yy}$) distribution by choosing a

clear-contrast region as the reference, the x- and y-direction are defined along the zigzag and armchair direction of $MoS_2$ structure, respectively. The overlapping of the atomic images and corresponding strain maps were showed in Fig.4.6 (c) and (d). The periodic pattern of the strain map indicated the periodic modulation of the projected atomic distance in TEM image, the blue/yellow region of the strain map indicates the compressive/tensile strain that corresponding to the relatively shorter/longer atomic distance in the TEM image. Since we found that the contrast modulation was original from the out-of-plane displacement of the $MoS_2$ nanosheet, such a kind of periodic strain distribution was attributed to the periodically ripple structure in the TEM image of the $MoS_2$ nanosheet. It is because the projected structure of the wavy ripple can form the periodic modulation of the atomic distance in TEM image, resulting in the periodic strain map. The details will be discussed in Chapter 5. Therefore, the contrast changes in the $MoS_2$ nanosheet under stretching is attribute to the wavy pattern of ripple structure.

### 4.3 The fracture of $MoS_2$ nanosheet

To get a further understanding of the mechanical response of $MoS_2$ under strain condition, we have studied the fracture of multilayer $MoS_2$ at large tensile strain condition (~30%) by in-situ stretching TEM observation. We found that the fracture of

multilayer $MoS_2$ should be an interlayer fracture with a preferred zigzag orientation.

Figure 4.7 shows the recorded TEM images of the $MoS_2$ nanosheet during stretching, with a stretching rate of ~1nm/s. The in situ stretching experiment showed that the fracture of multilayer $MoS_2$ was cracked layer by layer, which was an interlayer fracture, as shown in Fig. 4.7 (a)-(f). The fracture started at the position marked with the dark dash line in Fig. 4.7 (a), then the crack in the fracture region was propagated and the cracked layer was slid with stretching, as it was shown in Fig. 4.7 (b)-(f). Finally, the $MoS_2$ nanosheet was break, as shown in Fig. 4.7(g). We found that the broken part, which was fractured and separated from the $MoS_2$ nanosheet, was consist of a layered structure, suggesting an interlayer fracture. The area, marked with the yellow lines, of the broken parts was kept a crystal structure, and the left part was amorphous which may be damaged by the electron beam. Such an interlayer fracture could also be observed in the propagated break of the nanosheet, as shown in Fig. 4.7(i) and (j). The left $MoS_2$ layers were finally broke with increased stretching, and the edge of fracture was maintained as a single layer, as shown in Fig. 4.7(j). It confirmed that the fracture in the multilayer $MoS_2$ was broken layer by layer.

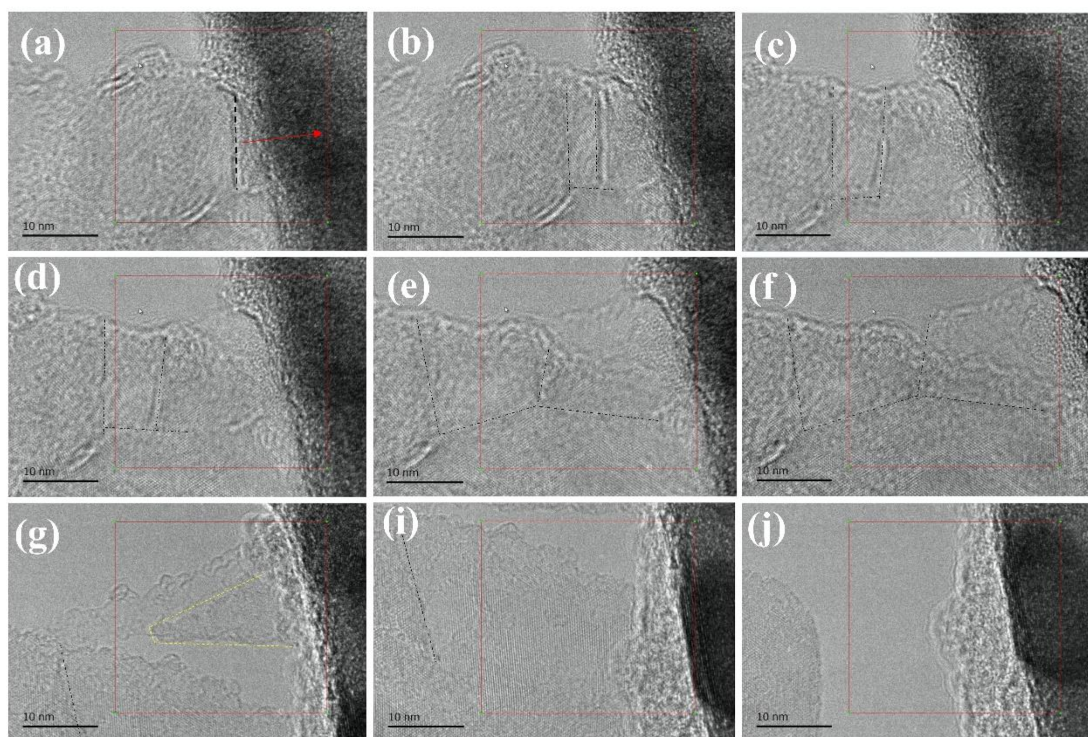


Figure 4.7. Screenshots of the in situ stretching TEM images of $MoS_2$ nanosheet. (a)-(i) TEM images recorded the fracture of multilayer $MoS_2$ during the stretching. (j) The TEM image of the $MoS_2$ nanosheet after fracture by stretching. The stretching direction is marked with the red arrow. The dark dash line indicates the fracture edge of the sample; the yellow dash line indicates the edges of the sample after the fracture.

We checked the fracture edge of the same broken sample and noticed that the edges of the fractured $MoS_2$ was clearly showed the same layered fracture, as shown in Fig. 4.8. The thickness of the regions, which were marked with III, II, and I in Fig.4.8, were identified to be 1.85 nm (three layers), 1.23 nm (two layers), and 0.62 nm (single layer), respectively, according to the visibility of atomic columns. Additionally, we found that

the fracture presented a preferred zigzag edges, which were marked as red dashed line the Fig.4.8.

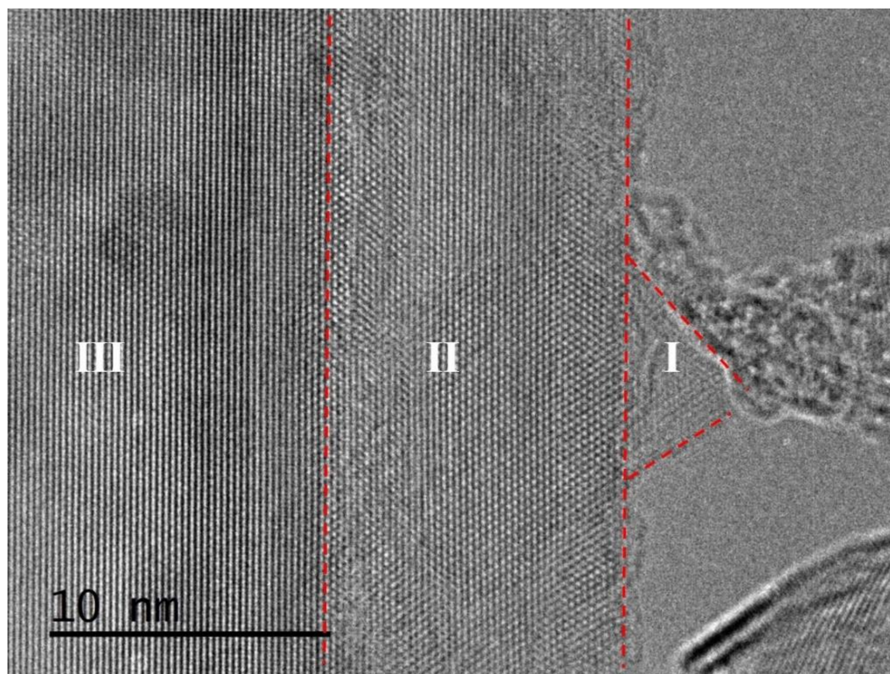


Figure 4.8. Atomic TEM image of $MoS_2$ nanosheet after fracture. The red dash line indicates the fracture edges, and the regions in different thickness are marked with I, II, and III.

Therefore, the fracture process of the multilayer $MoS_2$ nanosheet under stretching is demonstrated in Fig.4.9. It can be described by the following four process: (a) the initial nucleation of crack in the layer of $MoS_2$ under stretching, (b) the slid and propagation of the initial crack, meanwhile, the crack nucleated in the second layer, (c) the further the slid and propagation of the cracks, (d) the finally break of the fracture, resulting in a stepped structure, as shown in Fig.4.9 (a)-(d).

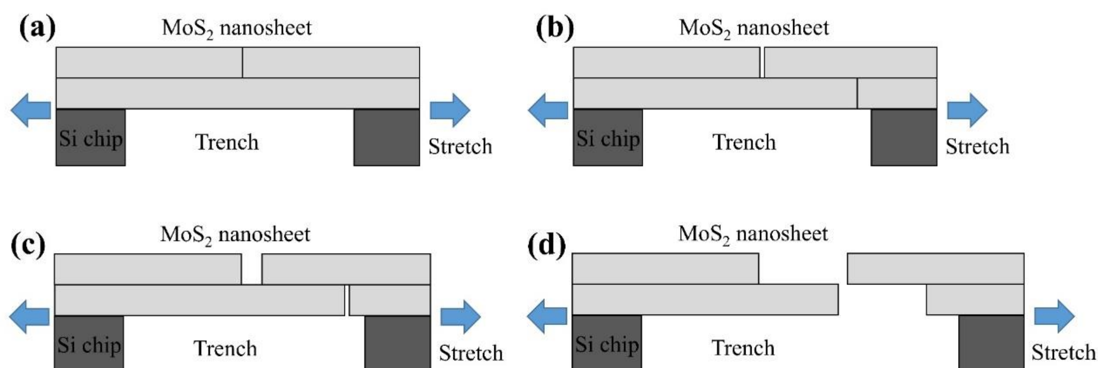


Figure 4.9. Illustration of the fracture of $MoS_2$ naosheet under stretching. (a) The initial nucleation of crack in the first layer. (b) The slid and propagation of the initial crack, meanwhile, the crack nucleated in the second layer. (c) The further sliding and propagation of the cracks. (d) The finally break of the fracture.

For further study the fracture property of $MoS_2$ layers, we checked the structure of fracture in other samples and confirmed the stepped structure with the preferred zigzag edges. Fig. 4.10 shows the morphology of the fracture region of another $MoS_2$ nanosheet. The low-magnification image of the fracture showed serrated edges, as shown in Fig.4.10 (a). With the TEM observation of the fracture region in a higher magnification, we found that the fractures should cracked layer by layer in the $MoS_2$ nanosheet. The steeped structures were formed on micrometer scale (the distance between the edges was ~1 μm), as shown in Fig.4.10 (b) and (c). With the atomic-scale TEM observation, we found that the stepped structure in micrometer scale was consist of several nanometer-scale steeped structures. As we found nanometer-scale stepped

structures in Fig.4.10 (d)-(e), which corresponding the region marked in Fig.4.10 (b). Also, the nanometer steeped structures showed predominant fracture edges along the zigzag direction, as marked by the red dashed line in Fig.4.10 (d)-(f), it confirmed that the break of $MoS_2$ nanosheet should be an interlayer fracture.

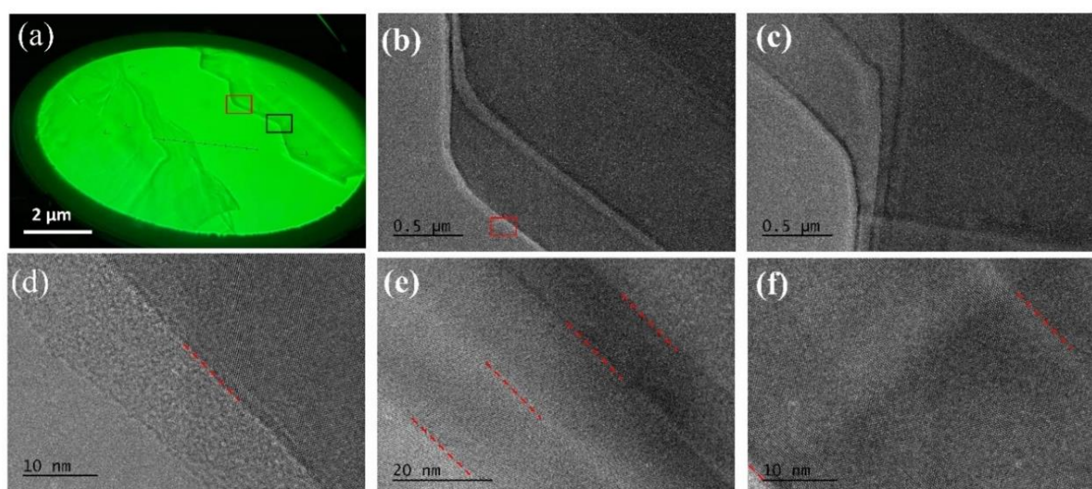


Figure 4.10. Images of $MoS_2$ nanosheet after the fracture. (a)The image of the fracture region at low magnification. (b)-(c)The edges in the crack region of marked with red and black in (a), respectively. (d)-(e) The atomic images of the sample from fracture edges to center region. The red dash line indicates the edges of the different layers in the sample.

Such an interlayer fracture with stepped structure $MoS_2$ layers is reasonable, since the zigzag edge is more easily formed during the crack propagation in the fracture. As we mentioned in Chapter 4.1, previous MD simulation and calculation results [67] showed that energy release along the zigzag direction (2.09 eV/Å) was lower than the

armchair direction (2.48 eV/Å), that makes a preferred zigzag edges in fracture. Additionally, another DFT calculations [55] showed similar results that the edge energy and surface energy (the energy cost for creating the edge/surface) of the zigzag orientation in $MoS_2$ monolayer were 0.71 eV $Å^{-1}$ and 1.83 J $m^{-2}$, respectively, which were lower than that of armchair orientation (0.72 eV $Å^{-1}$ and 1.87 J $m^{-2}$, respectively). Therefore, the zigzag edge is the preferred crack propagation orientation that consistent with our experimental results.

## 4.4 Conclusion

In this chapter, the suspended $MoS_2$ nanosheets were observed with our developed TEM holder, and the in situ stretching TEM observations were performed for investigating the mechanical response of $MoS_2$ under stretching.

We performed the TEM observation of the exfoliated $MoS_2$ nanosheet. The hexagonal FFT patterns of the TEM images indicated they were viewed from the [001] zone axis. The Moiré patterns were also obtained and suggested that there were lattice mismatch or rotation between the layers, it may be caused by the transfer process due to the weak interlayer interaction in the layered structure. Moreover, the $MoS_2$ naosheets were found to have the tendency to form the stepped structures with the zigzag edges, since the propagation of cracks along the zigzag configuration is preferred. It demonstrates the interlayer fracture in multilayer $MoS_2$ and confirms that the interlayer interaction between $MoS_2$ layers should be weak.

With the in situ stretching experiment under a small tensile strain condition, we observed the structural modulation of the $MoS_2$ nanosheet. The periodic contrast modulation during stretching with an approximately 0.7% tensile strain was revealed, it was attributed to the out-of-plane displacement of the ripple structure during stretching.

The in situ stretching experiments under the large tensile strain were performed for

understanding the fracture process of the multilayer $MoS_2$ nanosheet. The in situ TEM observation of the fracture process showed the propagation, the sliding, and finally the break of the crack, suggesting an interlayer fracture. Moreover, the crack region of other sample showed serrated edges and stepped structures. Such stepped structures were observed on both micrometer and nanometer scale, and the nanometer stepped structures showed predominant fracture edges along the zigzag direction.

Our results suggested that the fracture of the $MoS_2$ nanosheet is an interlayer fracture that presented stepped structures with zigzag edges.

# Chapter 5 The atomic-scale ripple structure in $MoS_2$ nanosheet

## Introduction

This chapter contains the observation and identification of the periodically rippled structure of the $MoS_2$ nanosheet. We demonstrate a strain-analysis method for the quantitative estimation of the ripple structure in the sub-nanometer scale from TEM image.

In Chapter 5.1, we show the TEM observation of the ripple structure of the $MoS_2$ nanosheet. In Chapter 5.2, we clarify the origin of the apparent strain in the HR-TEM image of the rippled structure and demonstrate the strain-analysis method to identify the rippled structure on atomic scale with HR-TEM images. In Chapter 5.3, we retrieve the ripple structure from experimental results. In Chapter 5.4, we will discuss the application of the strain analysis method, which shows the layer bending of the observed $MoS_2$ layers.

### 5.1 The TEM observation of the ripple structure of $MoS_2$ nanosheet

In the TEM observation of the suspended $MoS_2$ nanosheet, an atomic-resolved TEM image was observed near the side of the trench, as shown in Fig. 5.1. This nanosheet was identified to be 3 layers in thickness, according to the visibility of the atomic column. It is found that the contrast of the lattice fringes was modulated such that areas where the lattice fringes were clearly visible and areas where they were not arranged alternately. Such kind of contrast seemed to correspond to a rippled structure in the $MoS_2$ nanosheet.

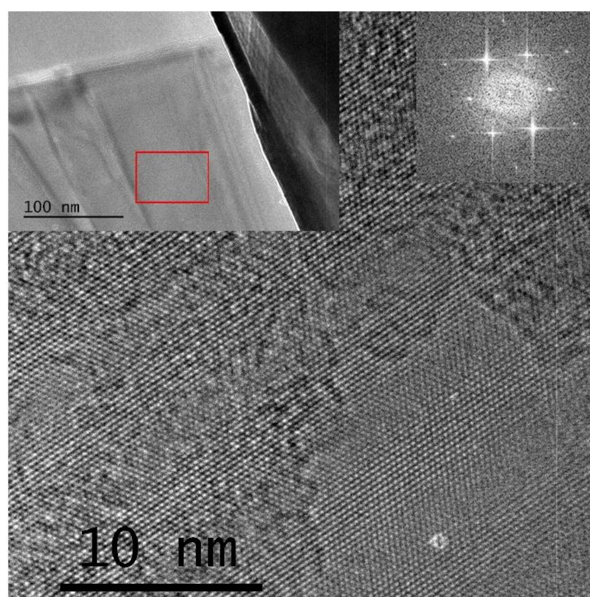


Figure 5.1. HR-TEM image of $MoS_2$ nanosheet with rippled structure. The left and right inserted images represent the low-magnification TEM image and the FFT pattern of the HR-TEM image, respectively. The HR-TEM image was obtained at the region marked with red frame.

The filtered HR-TEM image of Fig. 5.1 and the corresponding apparent strain map, which was obtained by using the GPA method to the HR-TEM image, were shown in Fig. 5.2 (a) and (b). Such kind of periodically modulated strain distribution indicated the spacing of the lattice was modulated along the y-direction (armchair direction) due to the projected information of the TEM image. It was suggested a rippled structure in the suspended $MoS_2$ nanosheet.

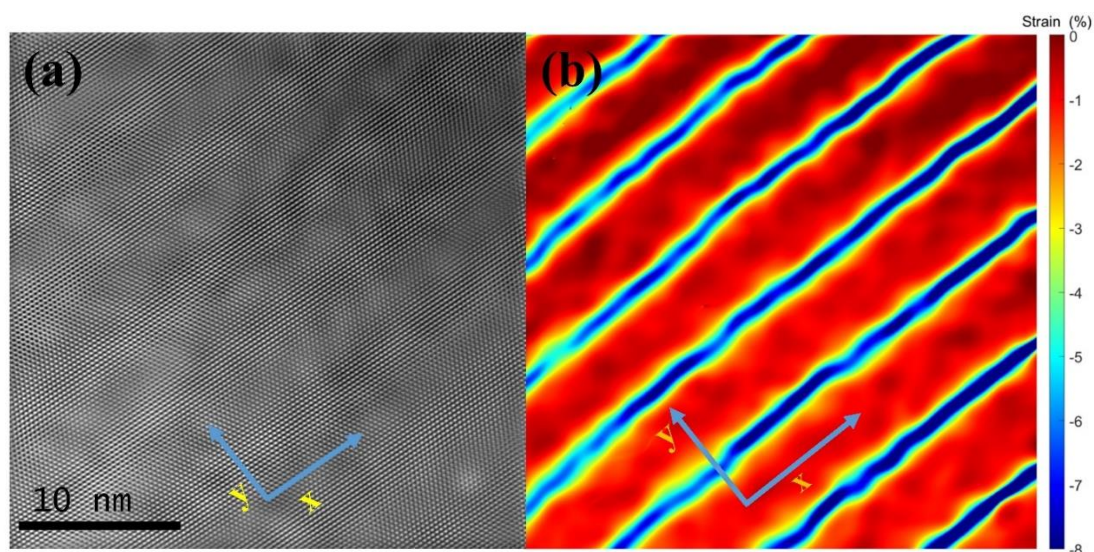


Figure 5.2. (a) Filtered HR-TEM image of the $MoS_2$ nanosheet in Fig.5.1. (b) Corresponding apparent strain map of the $MoS_2$; the periodically distributed pattern suggests the rippled structure.

The periodical ripple structures have been reported in suspended 2D materials due to imposed external strain [36,69]. Considering the exfoliate preparation and dry transfer process in our experiment, it seems that the rippled structure may be strain-

induced ripples. The strain was induced to the $MoS_2$ nanosheet during the dry transfer process, because of the contact between sample and the PDMS substrate. The $MoS_2$ nanosheet, which was adsorbed on the PDMS, may be stretched between the trench when it was pressed to the Si chip for making contact with the substrate. Furthermore, the $MoS_2$ nanosheet may be stretched longitudinally between two anchored boundaries of the trench, as showed in Fig 5.1, such a longitudinal stretching enhances the transversely compressive stress on the sample that may lead to the formation of the rippled structure.

To explain the periodical structure induced by the strain, theoretically, the sinusoidal function has been suggested to be suitable for describing ripple structure [34,35,70–72], since the sinusoidal structure showed the lowest energy. According to the reports in both supported graphene [40,73,74] and suspended graphene [36,75], the height profiles of strain-induced ripple structures also showed sinusoidal patterns. Therefore, it is reasonable to describe the rippled structure by the sinusoidal function.

Thus, based on our experiment results, we propose that the atom-scaled ripple structures can be identified from the strain distribution of the ripples that retrieved from their HR-TEM images.

## 5.2 Strain-analysis method to identify the atomic-scale ripples with TEM images

The projected information is obtained in the TEM image, when observing the rippled structures, as showed in Fig 5.3(a). Here the lattice spacing of the ripple structure of 2D materials is assumed to be the same, as we mentioned in Chapter 1.14. While, due to the wavy pattern of the ripple structure, the projected structure is modulated, which means the projected lattice spacing of the slop region is reduced, as marked with blue frame in Fig.5.3(a). In the meanwhile, the lattice spacing of the crest and trough region, marked with red frame, is almost unchanged. Based on the modulation of the projected lattice spacing, the apparent strain can be obtained, as shown in Fig.5.3(b). It is found that the compressive strain appears in the slope region, the period and the value of the apparent strain is related to the geometry of the ripple structure.

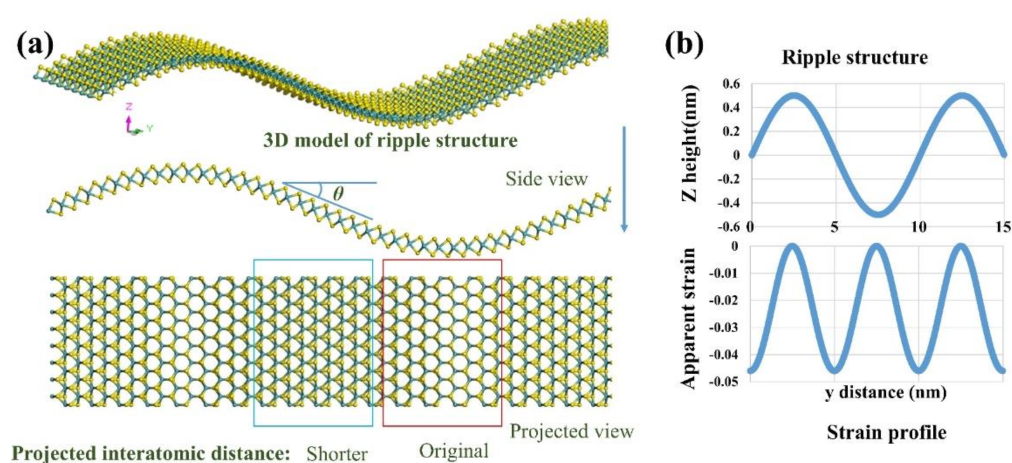


Figure 5.3. (a) Diagram shows the modulation of the projected structure to the ripple structure. (b) The relationship between the ripple structure and corresponding apparent strain, the amplitude and period of the ripple structure are 0.5 and 10 nm, respectively.

Therefore, following such a relationship, we demonstrate that the atomic-scale ripple structure can be quantitatively estimated by analyzing the apparent strain in the TEM image, since the apparent strain can be obtained by applying the GPA method to the TEM image. Note that the apparent stain is originated from the modulation of projected lattice spacing in TEM image, it is not a real strain in the ripple structure of $MoS_2$ nanosheet.

### *5.2.1 Apparent strain of the rippled structure*

When the rippled structure is formed along the y-direction and observed from the perpendicular z-direction; the projected lattice spacing (d') of the ripple structure is slightly reduced than the original one (d) at the region where the lattices are inclined due to the rippled pattern, and it can be described as the following equation:

$$d' = d\cos\theta, \tag{5.1}$$

where $\theta$ indicates the tilt angle of the tangent of ripple structure. Then, the apparent strain ε appears in the HR-TEM image of the ripple structure is defined with:

$$\varepsilon = \frac{(d' - d)}{d} = cos\theta - 1. \tag{5.2}$$

The derivative of the out-of-plane displacement, z, in the ripple structure along the y-direction ($\frac{dz}{dy}$) is defined by the tangent of the tilt angle $\theta$:

$$\frac{dz}{dy} = tan\theta. \tag{5.3}$$

By combining the above formulas (5.1), (5.2), and (5.3), the apparent strain ($\varepsilon_{GPA}$)

is described as the following equation:

$$\varepsilon = \frac{1}{\sqrt{(\frac{dz}{dy})^2 + 1}} - 1. \tag{5.4}$$

The formula (5.4) indicates that the apparent strain, which origin from the projected structure of the ripple, depends on the geometric structure of the ripple. It means that the amplitude, the period, and the shape of the ripple structure can be identified by mapping the apparent strain $\varepsilon$.

Considering that the ripple structure can be represented by the sinusoidal pattern with amplitude $A$ and period $\lambda$; the out-of-plane displacement, $z$, can be described along the y-direction as follows:

$$z = A sin \frac{2\pi y}{\lambda}. \tag{5.5}$$

Therefore, the apparent strain in the TEM image of the sinusoidal ripple can be described with following:

$$\varepsilon = \frac{1}{\sqrt{(\frac{2A\pi}{\lambda} \cos \frac{2\pi y}{\lambda})^2 + 1}} - 1. \tag{5.6}$$

The Eq. (5.6) shows that the period of apparent strain is half to that of ripple, $\lambda$, and its value is related to the $A$ and $\lambda$ of the ripple structure.

### *5.2.2 Apparent strain in the HR-TEM image of the rippled structure*

To investigate the apparent strain of the ripple structure in HR-TEM image, we made the atomic models of the rippled structure with $MoS_2$ monolayer. The apparent

strain was obtained by applying GPA method to the simulated HR-TEM images of ripple structures. Thus, the relationship between the geometric structure of the ripple and the apparent strain mapping was quantitatively investigated.

The atomic models of the rippled $MoS_2$ structure were obtained by using the software Material Studio. Regarding the simulated HR-TEM image in Fig. 5.4, the supercell was set to $30 \times 0.63 \times 1.5$ nm$^3$ when the amplitude was 0.5 nm and the period was 10 nm. In the simulation of HR-TEM image, the cut-off wavenumber was set to 15 nm$^{-1}$ and the Mott formula with the Doyle-Tuner X-ray scattering factor was used as the atomic scattering factor. Image calculation was performed by dividing the rippled $MoS_2$ structure into 10 slices. When the direction of the incident electron beam was tilted from the c-axis, the $MoS_2$ nanosheet was divided on the plane perpendicular to the incident direction to create slices, and then the image calculation was performed. The parameters of the simulation were set according to our observation conditions, that the accelerating voltage, spherical aberration, beam convergence, defocus value, and the defocus spread were set to 200 kV, 0.7 mm, 3.4 mrad, 50 nm (underfocus), 5 nm, respectively. The HR-TEM images simulated with the focus of -50 nm well reproduced the experimental HR-TEM images. The apparent strain mappings of the rippled structures were obtained with the software xHREM by applying the GPA method to the simulated corresponding HR-TEM images.

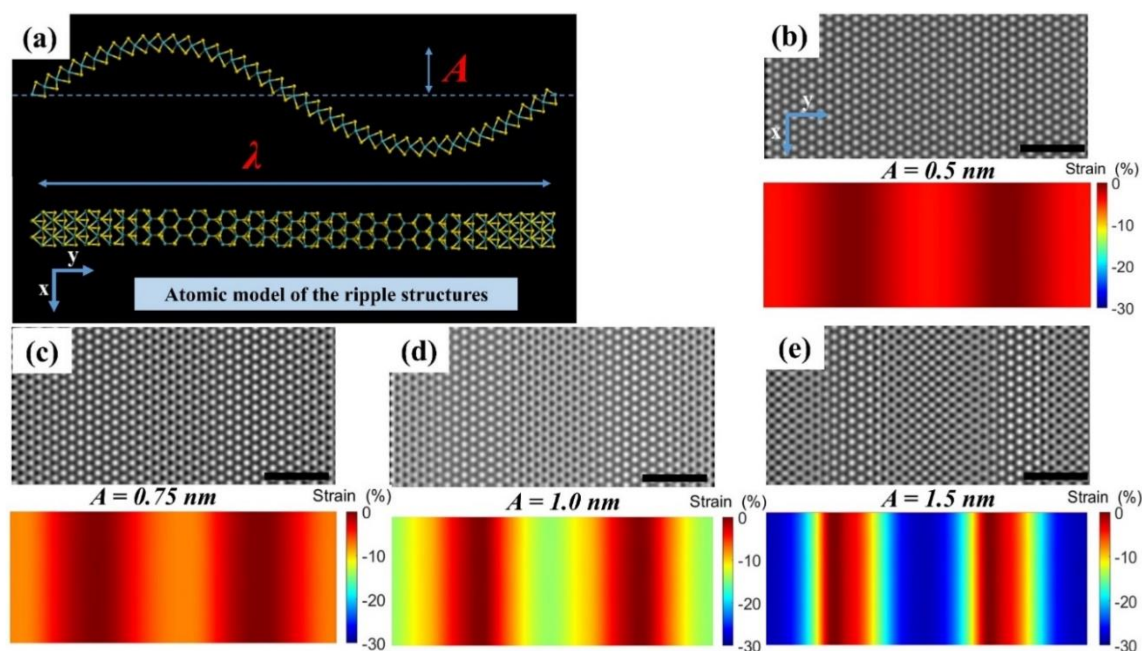


Figure 5.4. (a) Atomic model of the rippled structure of $MoS_2$ monolayer, which is aligned along the x (zigzag) direction and modulated along the y (armchair) direction. (b)–(e) The simulated HR-TEM image (upper) and the corresponding strain map (lower) of the ripple structure with a period of 10 nm and amplitude of 0.5, 0.75, 1.0, and 1.5 nm, respectively. The apparent strain is almost zero near the maximum out-of-plane displacement, and the period in the strain map is shown to be half of that structure model. Scale bar: 2 nm.

Thus, by making the atomic models of the ripple structures of $MoS_2$, simulating the HR-TEM images, and obtaining corresponding apparent strain mappings, the relationship between the geometric structure of the ripples and apparent strain mappings was quantitatively investigated. As shown in Fig. 5.4(a), a rippled structure of monolayer $MoS_2$ sheet was described with a sinusoidal pattern of 10 nm in period ($\lambda$).

The amplitude (out-of-plane displacement) was set from 0.1 nm to 1.5 nm in a 0.1-nm step. In the simulated HR-TEM images, the contrast of Mo or S atoms was found not to be slightly modulated due to the small amplitude. As shown in Fig. 5.4(b)–(e), the apparent strain mappings were obtained by applying the GPA method to the simulated HR-TEM images of the ripples with the amplitudes of 0.5 nm, 0.75 nm, 1.0 nm, and 1.5 nm, respectively.

To estimate the apparent strain from the HR-TEM image with the GPA method, the region where the strain is zero should be selected as the reference. However, owing to the wavy pattern of ripple structure, there is no flat area that perpendicular to the direction of incident electron beam. Therefore, we selected the region of lattice spacing at the crest/trough region of the ripple structure in the HR-TEM images, where the ripple slope was gentle, as the reference to obtain the apparent strain mapping. Additionally, considering that the ripple structure should have only compressive strain because the projected lattice spacing of the ripple was always reduced than of the flat region, the obtained strain was adjusted so that the maximum strain was zero, as demonstrated in Fig. 5.4. The apparent strain mappings show periodical patterns with half of the period of the ripple structure as mentioned above. In the area of the crest/trough region of the ripple, the apparent strain becomes zero in the apparent strain mappings. Moreover, the maximum compressive strain appears in the slope regions.

When the incident electron beam is perpendicular to the z-direction of the sinusoidal ripple of $MoS_2$ monolayer, the maximum compressively apparent strain is obtained to be -0.045, -0.90, -0.155, and -0.275 for the amplitudes of 0.5, 0.75, 1.0, and 1.5 nm, respectively, as shown in the line profiles of Fig.5.5(a). It is found that he maximum compressive apparent strain is almost proportional to the amplitude, as shown in Fig. 5.5(b). We observed that the change in apparent strain (the maximum compressive strain) is sufficiently sensitive to the amplitude at the sub-nanometer scale. Since it is reported that the accuracy of GPA method in the measurement of the strain was approximately 0.01 [61], that means the small variation of amplitude, such as 0.05 nm, can be precisely measured. In Fig. 5.5(a), when the amplitude is larger than 1.0 nm, we found that there is a small deviation of data points from the smooth fitting curve. Also, we observed that the apparent strain profile is slightly distorted when amplitude is 1.5 nm. We suppose that such a deviation in data is not intrinsic, it is origin from the limited pixel size in the simulation, it seems not small enough to appropriately describe the ripple structure when increasing the amplitude (out-of-plane displacement).

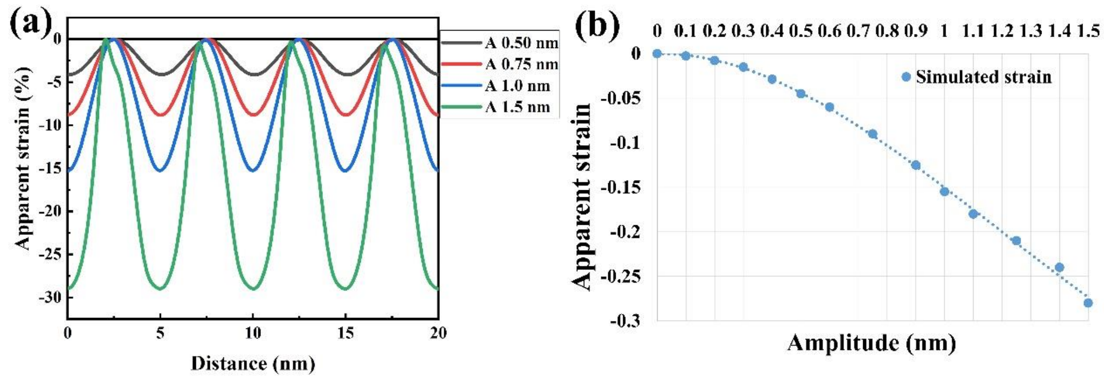


Figure 5.5. (a) Line profile of the apparent strain map for the amplitudes of 0.5, 0.75, 1.0, and 1.5 nm, respectively. (b) Relationship between the amplitude of the sinusoidal ripple and the simulated maximum compressively apparent strain.

Considering that the rippling plane of the rippled structure may inclined to the perpendicular plane of the incident electron beam, that is the ripples may incline around the x axis, we analysed the influence of the tilting angle on the strain profile, as showed in Fig.5.6. It is found that the period of ripple is the same with the strain profile, the value of strain increased with inclination, and the shape of strain profile was modulated by the inclination. Such a phenomenon is a result of the projected structure of ripples was modulated due to tilting.

Thus, based on our strain analysis method, by analyzing the value and distribution of the apparent strain profile, the structure of the ripple, including the amplitude, period, and inclination angle, can be quantitatively estimated on sub-nanometer scale.

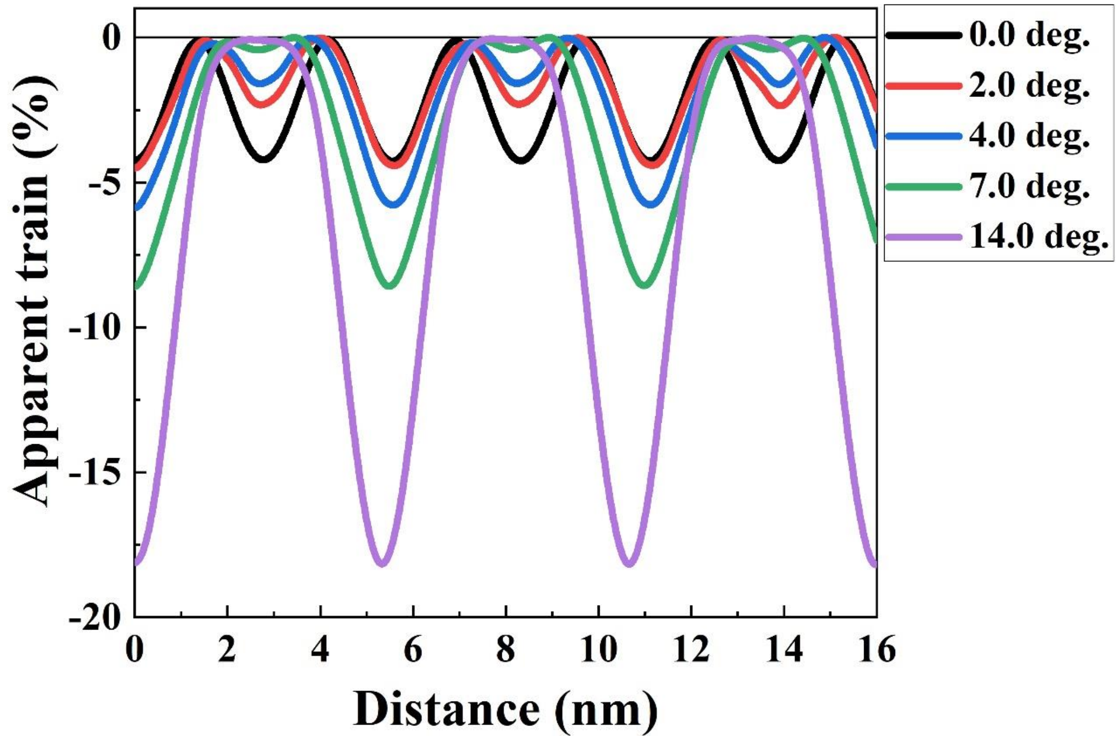


Figure 5.6. Inclination angle dependence of the apparent strain of rippled structure. With the period and amplitude of 5.5 and 0.5 nm, respectively

### 5.3 Retrieving ripple structure from experimental result

#### *5.3.1 Analysis of the observed $MoS_2$ rippled structure*

To retrieve the rippled structure, as shown in Fig 5.2 (a), we analyzed the rippled structure on atomic scale and measured the profile of the apparent strain, as shown in Fig 5.7. Fig. 5.7(a) and (b) showed the atomic image and corresponding apparent strain mapping, and the superimpose of the atomic image with the apparent strain mapping was shown in Fig. 5.7(c). It is found that the ripple structures were aligned parallel to

the x-direction, which defined along the zigzag configuration, and the ripple structures were periodically modulated to the y-direction, which is along the armchair configuration. This result agrees with the previous report, in which the simulation demonstrated that the rippled structure formed along the armchair configuration is more stable [75].

To obtain the apparent strain distribution, it was measured by averaging along the y-direction within a black frame in the apparent strain map of Fig. 5.7(b), and the corresponding profile of the apparent strain was estimated along the y-direction, as shown in Fig. 5.7(d). We noticed that there are fluctuated values of maximum compressive strain between different periods, such a phenomenon might be attributed to the slight amplitude modulation or the measurement error. Regarding the former, the apparent strain could change by about 1.6% when the amplitude differed by 0.1 nm. This suggests that the amplitude may slightly fluctuate from a place to another. Regarding the latter, the error of the GPA method for measuring the strain has been reported to be approximately 1% by Hÿtch et al [60]. For simplification, the average value of the maximum compressive strain, which was indicated by an arrow in Fig. 5.7(d), was used to reproduce the out-of-plane displacement of the ripple structure.

The profile of apparent strain, as shown in Fig5.7(d), shows a clearly periodic pattern, but it is a little different from a standard sinusoidal pattern as it shows sharp

grooves. This suggested that the periodic profile includes not only a certain frequency component, $k$, but also those of higher frequencies, such as $2k$ and $3k$. Therefore, we carried out Fourier transform (FT) analysis on the apparent strain profile of Fig. 5.7(d). It is found that it comprises with three major frequencies, $k$, $2k$, and $3k$, which have amplitude (out-of-plane displacement) ratios of 1, 0.5, and 0.2, respectively, as given by the following equation:

$$\varepsilon = \varepsilon_0\{\sin(2\pi \boldsymbol{ky}) + 0.5\sin(2\pi \cdot 2\boldsymbol{ky}) + 0.2\sin(2\pi \cdot 3\boldsymbol{ky})\}. \quad (5.7)$$

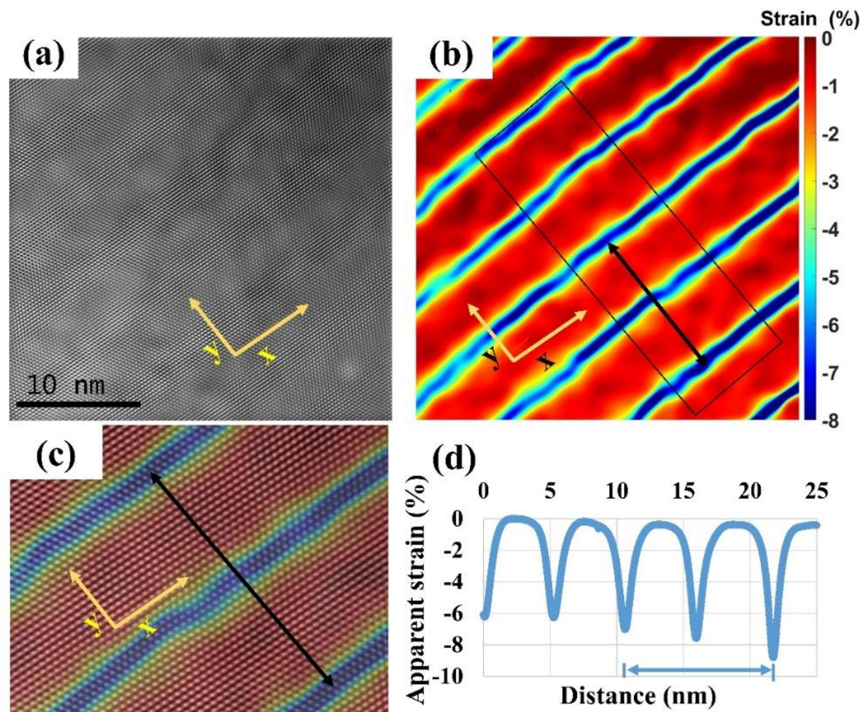


Figure 5.7. (a) Filtered HR-TEM image of Fig.5.1. (b) Corresponding apparent strain map; the periodic pattern indicates the ripple structure. (c) Superimposed apparent strain map and enlarged atomic image, the atomic-scale ripple structure is revealed. (d) Profile of the apparent strain map in the region of black-frame rectangle region in (b).

As we know that the apparent strain is origin from the structure of ripple. Thus, according to the formula (5.7), the amplitude profile, z, was retrieved by combining these three frequency components, as shown in Fig. 5.8(a). We noticed such a structural pattern is asymmetric, which means it was not stable under a strain condition. Instead, we noticed that the profile pattern and the corresponding structural pattern was an inclined sinusoidal pattern with respect to the incident electron beam, as shown in Fig. 5.8 (b). Note that Fig. 5.8 (a) shows the structure (out-of-plane displacement) of the ripple, while Fig. 5.8 (b) shows the displacement including the inclination of the ripple structure. Such an inclination seems to be reasonable, since the incident electron beam does not always perpendicular to the nanosheet. It was confirmed by the FFT pattern of the HR-TEM image in Fig. 5.1, as the larger and blurred FFT spots were observed along the direction of the ripple, indicating the inclination of the $MoS_2$ nanosheet. Therefore, we examined the apparent strain of the ripple structure when the sample was slightly inclined with an angle α. By simulating the HR-TEM image of the ripple structure of $MoS_2$ nanosheet with different inclined angles, we obtained the corresponding profiles of the apparent strain, as shown in Fig. 5.8(c). It is found that one of the two adjacent grooves of the apparent strain profiles tends to be deeper while the other tends to be shallower, when the inclination angle increases. It means that the distribution of apparent strain modulated with inclination, the period of the profile changes to be the

same as that of ripple structure, the maximum compressive strain decreases with inclination. Meanwhile, both the maximum and minimum compressive apparent strain occurred near the slope area of the ripple structure.

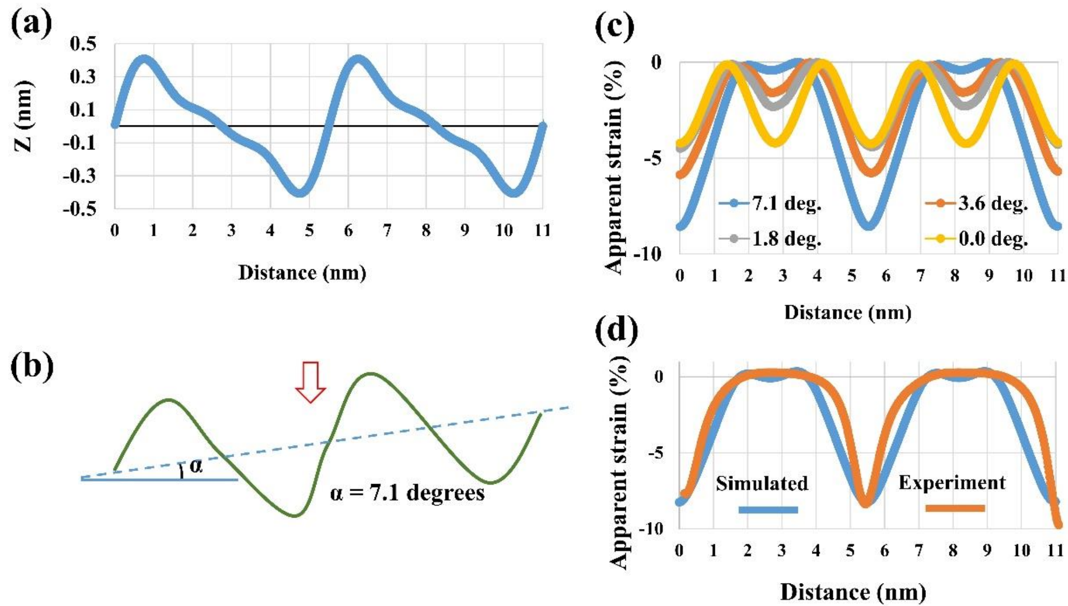


Figure 5.8. (a) The out-of-plane displacement of the ripple structure retrieved from the apparent strain profile. (b) The structure model shows the out-of-plane displacement of the inclined sinusoidal ripple. The red arrow indicates the direction of the incident electron beam. (c) Apparent strain profile of the sinusoidal ripple structure with different inclination angle. (d) Experimental and simulated apparent strain profiles, the inclination angle of the simulated ripple is 7.1°, the experimental result obtained from the region marked with the arrow in Fig. 5.7(d).

### *5.3.2 Estimation of the observed $MoS_2$ ripple structure*

As we mentioned in section 5.2, it is easy to estimate the period and amplitude of rippled structure from the apparent strain, when the nanosheet is not inclined. However,

when the sheet is inclined, the both the shape and value of the apparent strain modulated with the inclination angle. The situation is different. Therefore, firstly, we should identify the amplitude and period based on the geometric information obtained from the apparent strain map and TEM image; then, we can estimate the inclination angle according to the value of the apparent strain.

Firstly, the amplitude can be obtained from the geometric relationship between the (full) length (which is measured within one period of the ripple structure), amplitude, and period of the ripple structure. The length of the ripple structure, *S*, can be obtained by integrating the pattern of ripple along the y-direction as following:

$$S = \int_0^{\lambda} dy \sqrt{1 + (\frac{\partial z}{\partial y})^2} = \int_0^{\lambda} dy \sqrt{1 + \left[ A \frac{2\pi}{\lambda} \cos(\frac{2\pi y}{\lambda}) \right]^2} . \tag{5.8}$$

The length *S* should be equal to multiplying the bond length with the number of lattice spacing within one period. The number of the lattice spacing within one period of the ripple structure was measured to be 21 (marked with black arrow in Fig. 5.7(c)). Thus, the length *S*, could be calculated to be 5.7 nm. Therefore, the amplitude, A, was obtained by solving formula (5.8), which is 0.3 nm.

Secondly, we can estimate the inclination angle based on the value and shape of the apparent strain. We built the atomic model of the ripple structure with the different inclined angles, then correspondingly simulated HR-TEM images and apparent strain

mapping/profiles could be obtained. It is found that when the inclination angle s 7.1°, one adjacent grooves disappeared and became almost flat; that apparent strain profile is a similar pattern to the experimental profiles, as shown in Fig. 5.8(d). Moreover, the simulated results of the apparent strain profile showed a maximum compressive value of -8%, it also reproduced the same value as the experimental result. Therefore, the observed ripple structure could be explained by an inclined sinusoidal ripple.

## 5.4 The bending of multilayer $MoS_2$ nanosheet

### *5.4.1 Apparent strain of ripple structure with a small inclination angle*

In chapter 5.2 and 5.3, we discussed the influence of the inclination angle on the strain profile and showed an experimental result with an inclination angle of 7.1 degrees. As we showed in Fig. 5.6. and Fig. 5.8(c), the inclination angle can modulate both the distribution and the value of the strain profile. Therefore, when the inclination is small, there will be steep and distinctly shallow grooves in the strain profile.

Here, we identified a ripple structure with a small inclination angle, as shown in Fig 5.9 (a)-(c). The thickness of the sample was estimated to be about 2.5 nm (four layers), it showed a small fluctuation in the minimum and maximum strain value, for simplification, we investigated its shape and inclination by using the method we demonstrated in chapter 5.3 with the average value of the four periods marked with the

arrow. The period was measured to be 9.5 nm, and the amplitude and inclination angle was estimated to be approximately 0.28 nm and 3.6 degrees, respectively.

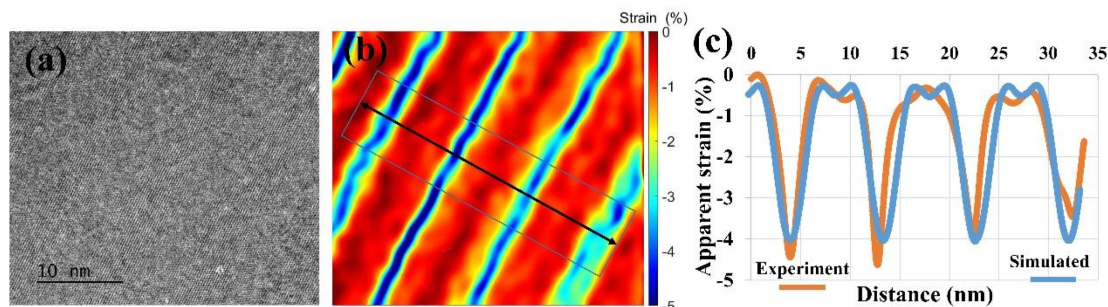


Figure. 5.9. (a) HR-TEM image of $MoS_2$ nanosheet. (b) Apparent train map of (a). (c) Apparent strain profile of the black frame region in (b) and the estimated ripple structure.

### *5.4.2 Bending model of the multilayer $MoS_2$*

The observed ripple structures, as shown in Fig.5.1 and Fig.5.9, were identified to be multilayer $MoS_2$ with three and four layers in the thickness instead of a single layer. While, it was quantitatively estimated based on the simulation with a monolayer model. It is important to verify this estimation when applied to multiple layers, as the bending of single layer and multilayer of 2D material might be different. Therefore, we checked the bending of multilayer $MoS_2$ based on our experimental results.

In the bending of ultrathin 2D materials, there are two structural models for describing the bending behavior, the plate model and the layer model [47], in which the bending was involved and was not involved the in-plane distortion, respectively.

Usually, the bending of the monolayer 2D materials was treated as not with the in-plane distortion. As reported by Zhang et al. [44], the molecular dynamics calculation showed that there was no participation of the σ bond in the bending of monolayer graphene. Instead, the π-orbital misalignment between adjacent carbon atoms occurred, that resulting in the lack of in-plane strain in the bending.

Meanwhile, in the multilayer graphene case, they proposed that the bending can be described as the plate model, in which the atoms in each layers were interacted by van der Waals force. In the plate model, the atom spacing was compressed/stretched in the concave surface /convex surface stretched. Thus, the in-plane strain distribution was occurred in the bending, as the atom spacing in each layer is alternatively extended or shrunken in the ripple structure.

For checking if the plate model were suitable or not to explain the bending multilayer $MoS_2$, the atomic ripple structure with plate model (in-plane distortion model) was designed for the case of triple layers, as shown in Fig.5.10(a). The atomic spacing is extended in the outer layer and shrunken in the inner layer, so the relative atomic positions between the two layers are maintained as much as possible. The corresponding simulated TEM image and apparent strain map were obtained and showed in Fig.5.10(a). It is found that the HR-TEM images is complex and the apparent strain profile shows a complex pattern even when the triple-layer is not inclined, as

shown in Fig. 5.10(b). With the inclination increases, we can observe that the inclination makes a more complex pattern in the apparent strain map.

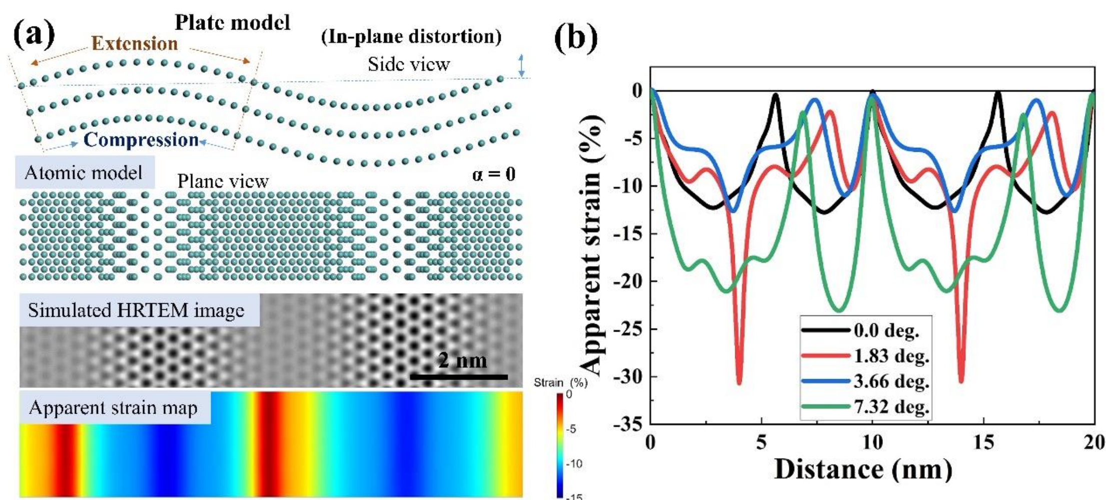


Figure 5.10. (a) Plate model of the triple atomic layers with in-plane distortion, corresponding HR-TEM image and apparent strain map without inclination was shown. (b) Apparent strain profile with inclination of plate model bending within two periods. Atomic models were designed with the period and amplitude of 10 and 0.5 nm, respectively.

Our experimental results always showed simple patterns in the HR-TEM image and apparent strain maps, even though the thickness was different. The multi-layer plate model with in-plane distortion is obviously unsuitable to explain the experimental results. Therefore, by considering that there is very weak interaction between layers, we can make the triple-layer layer model without in-plane distortion, which means each layer of the model have the same atomic arrangement, as shown in Fig. 5.11(a). In this

layer model, the simulated HR-TEM image and corresponding apparent strain show simple patterns. The profiles show the same pattern as the experimental results. Moreover, it also shows the same inclination dependence with the monolayer model, as shown in Fig. 5.11(b). Therefore, our experimental results can be explained by such a layer model, which suggests that interlayer interaction between $MoS_2$ layers may be weak.

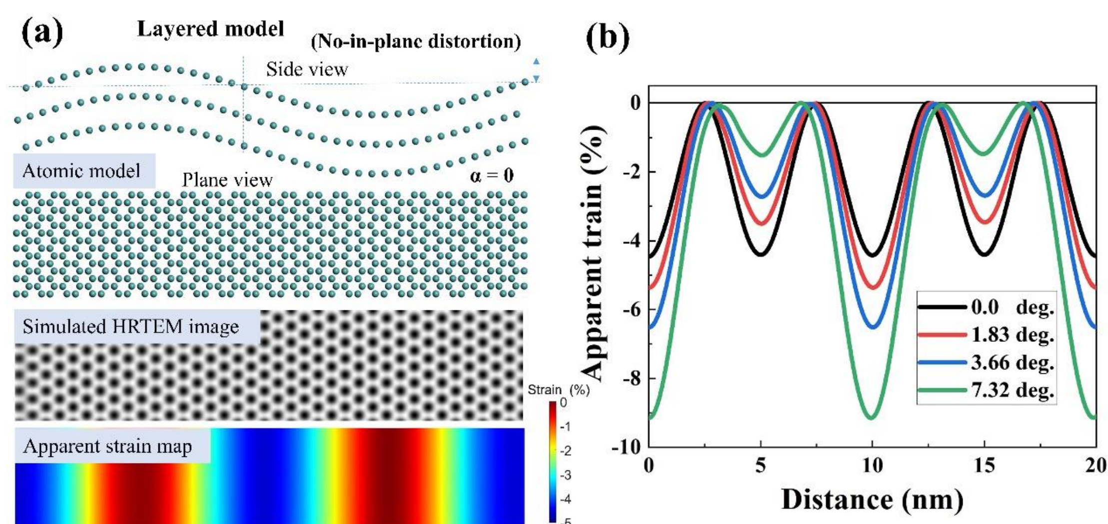


Figure 5.11. (a) Layer model of the triple atomic layers without in-plane distortion, corresponding HR-TEM image and apparent strain map without inclination was shown, the layers were consisting as a AB stacking. (b) Apparent strain profile with inclination of plate model bending within two periods. Atomic models were designed with the period and amplitude of 10 and 0.5 nm, respectively.

Additionally, we compared the strain profile of ripple structure of $MoS_2$ layer in

different thickness, as shown in Fig. 5.12. The thicknesses of the samples (a)-(c) were estimated to be three, five, and eight layers, since their visibilities were measured to be 0.06, 0.08, and 0.12. We find that they show simple patterns in the apparent strain mappings regardless of thickness. Though the samples were inclined and showed fluctuations in their amplitude, but they showed periodicities.

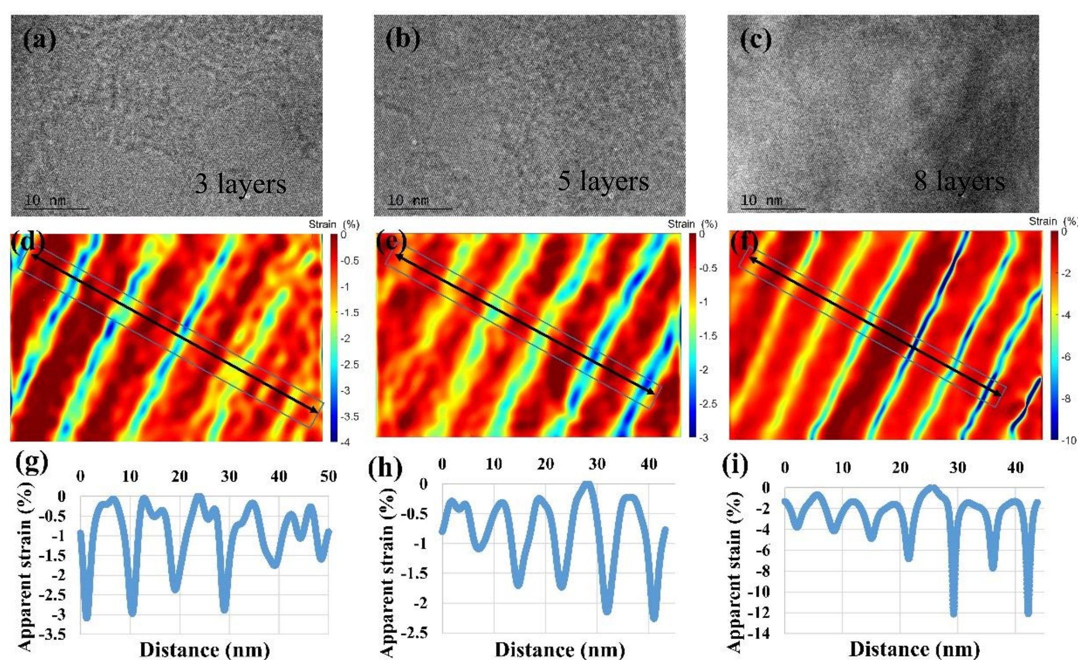


Figure. 5.12. (a)-(c) AR-TEM images of $MoS_2$ nanosheets with different thicknesses. (d)-(f) Strain map of (a), (b), and (c), respectively. (g)-(i) Strain profile of the bold rectangle area in (d), (e), and (f), respectively.

So we suggest the layer model (no-in-plane distortion with multiple layers) is suitable to describe the ripple structures in our observation. And we believe our strain-analysis method is useful for estimating the rippled structures of multiple-layer 2D

materials. As the ripple structures were observed in thicker samples, they showed similar periodic strain profiles. So we believe our method and the layer model are valid when the thickness of 2D materials was thicker than three monolayers.

### *5.4.3 The appearance of the atomic-scale $MoS_2$ ripple structure*

The previous report [36,39] showed that the amplitudes of the ripple structures in 2D materials were in the range from 10 nm to several microns. According to continuum mechanics, the relationship between the ripple geometry and longitudinal tensile strain [41] can be described by:

$$\lambda = \frac{(2\pi L t)^{1/2}}{\left[3(1-\nu^2)\varepsilon\right]^{1/4}}, \tag{5.9}$$

$$A = (\nu L t)^{1/2}\left[\frac{16\varepsilon}{3\pi^2(1-\nu^2)}\right]^{1/4}, \tag{5.10}$$

where $L$ is the longitudinal length of the sample, $t$ is the thickness, $\varepsilon$ is the applied tensile strain, and $\nu$ is Poisson's ratio. Eqs. (5.9) and (5.10) suggest the relationships of $\lambda \propto \varepsilon^{-1/4}$ and $A \propto \varepsilon^{1/4}$, which can be obtained by minimizing the total energies of bending and stretching with respect to $\lambda$. Though such a relationship is retrieved from the macroscale elastic sheet, it has been applied to 2D materials, such as graphene, in previous reports [35,36]. Meanwhile, a sub-nanometer scale ripple structure was reported on graphene [34,69]. It was found that the $\lambda$ and $A$ did not follow such a power

scaling law to $\varepsilon$, which was attribute to the lack of bending resistance in monolayer graphene.

To clarify the appearance of the atomic-scale ripple structure in multilayer $MoS_2$, the bending energy term should be considerate. In the continuum mechanism, the total energy ($U_T$) of the ripples is the sum of the bending energy ($U_B$), due to deformations in the y-direction (i.e., the direction of the periodic ripple pattern), and the stretching energy ($U_S$), $U_T = U_B + U_S$ . Here the bending energy is given by $U_B = \frac{1}{2}\int_A B(\partial_y^2 \zeta)^2 dA$, where $B = Et^3/[12(1-v^2)]$ is the bending stiffness, $\zeta$ is the out-of-plane displacement, A is the area, E is Young's modulus, $t$ is the thickness, and $v$ is Poisson's ratio. The bending energy term implies the energy for bending induced by in-plane strain. The stretching energy ($U_S$), which is loaded as the tension $T(x)$ along the x-direction, can be described as $U_S = \frac{1}{2}\int_A T(x)(\partial_x \zeta)^2 dA$ . When combined with the constraint of inextensibility, which indicates the length of the un-rippled structure and rippled structure is the same, and the sinusoidal function of $\zeta$, then $U_T$ can be minimized with respect to $\lambda$ to obtain the 1/4-power scaling laws described in Eqs. (5.9) and (5.10).

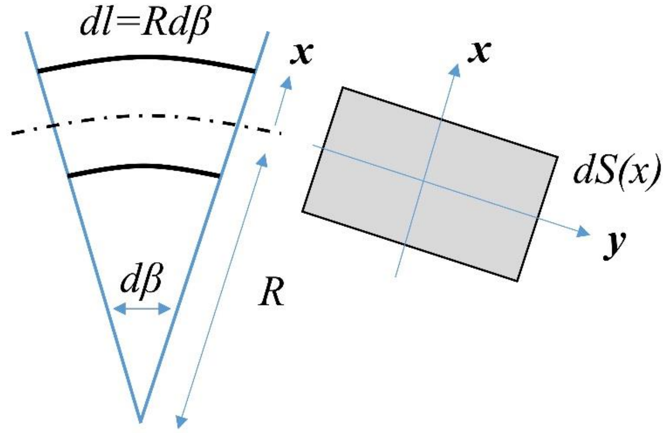


Figure 5.13. Diagram of the plate bending. Left: an infinitesimal part of the bending beam. Right: the cross-section view of the left part. R is the curvature radius, β is the radian due to bending.

We should notice that the bending energy term ($U_B$) of continuum mechanics is related the plate model, in which the bending energy is approximate to the energy induced by the in-plane strain. The diagram of the plate model is shown in Fig.5.13.

The bending energy terms in the plate model can be derived as following, with a segment of a bending beam with a barycentric axis, as shown in Fig. 5.13. The infinitesimal sector of the bending beam: $dl=Rd\beta$, where $R$ is the curvature radius. The in-plane strain of a small bending of the beam:

$$\varepsilon_i = \frac{(R+x)d\beta - Rd\beta}{Rd\beta} = \frac{x}{R}, \tag{5.11}$$

where $x$ is the distance from the barycentric α axis, thus, the bending energy:

$$U_B = \frac{1}{2}\sigma\varepsilon_i = \frac{1}{2}\int\frac{E\varepsilon_i^2}{1-v^2}dldS(x) = \frac{1}{2}\int\frac{E}{1-v^2}\frac{1}{R^2}I_y dl\ . \tag{5.12}$$

Here, $\sigma$ is the stress, $I_y$ is the moment of inertia, $I_y = \frac{bt^3}{12}$, substituting with the thickness ($t$) and width ($b$).Then, we obtain:

$$U_B = \frac{1}{2}\int \frac{E}{1-v^2}\frac{1}{R^2} I_y dl = \frac{1}{2}\int \frac{Et^3}{12(1-v^2)}\frac{1}{R^2} dA . \tag{5.13}$$

It is equivalent to $U_B = \frac{1}{2}\int_A B(\partial_y^2 \zeta)^2 dA$ , as we mentioned above. The retrieved expression indicating the bending energy term of the plate model (continuum mechanics) is related to the bending-induced in-plane strain.

However, our strain analysis showed that the experimental results can be explained by layer model, instead of plate model. It means the bending behavior of the multilayer $MoS_2$ in our experiment was the same with the single layer. Therefore, the failure of the continuum mechanics, which shows the atomic-scale ripple structures in $MoS_2$ nanosheet, is suggested to the invalid plate model in 2D materials, due to the bending behavior of 2D materials is different from bulk materials that no in-plane strain was induced during the bending.

As the ripple structure of graphene at subnanoscale has been reported to have a much smaller amplitude and period [69] than those calculated using Eqs. (5.9) and (5.10), suggesting a breakdown of continuum mechanics approximation. It has been thought to be attributed to the lack of out-of-plane bending resistance in monolayer graphene. Also, MD simulations showed that the plate model assuming in-plane strain distribution broke down for monolayer graphene [44]. It was considered that the bending of

monolayer graphene involved π-orbital misalignment instead of in-plane σ-bond deformations. The MD simulations of monolayer $MoS_2$ also showed that the bending does not change the Mo–Mo distance when the bending radius is greater than 4 nm [45]. And, the Mo–Mo interaction has been reported not to contribute to the bending modulus of monolayer $MoS_2$ [46]. Thus, the strain stored in the monolayer $MoS_2$ was suggested to be negligible, which is contradicted the bending behavior of the plate model in continuum mechanics.

The observed $MoS_2$ nanosheets are multiple layers, which is thought to be different from the monolayer case at a glance. However, we think that even multilayer $MoS_2$ nanosheets do not have in-plane strain distribution in the rippling direction like monolayer graphene. Because the ripple structure of $MoS_2$ nanosheets has been reported to show the same pattern regardless of the thickness in the apparent strain map, as shown in Chapter 5.4.2. It implies that each layer comprising the nanosheet has the same ripple structure, suggesting no in-plane strain in the bending. In this sense, the out-of-plane bending resistance of monolayer or multilayer 2D materials may be so low that the ripple structure can be formed easily at the atomic scale.

These results are consistent with our consideration indicating that the plate model was also invalid in multilayer 2D materials. That is, the invalid plate model indicating the bending energy term in continuum mechanics approximation was inapplicable, it

results in the failure of continuum mechanics and the appearance of atomic-scale ripple structure in 2D materials.

## 5.5 Conclusion

With the TEM holder, the suspended $MoS_2$ nanosheet can be observed under the strain condition. In the TEM observation, the periodic ripple structures of the $MoS_2$ nanosheet, which formed parallel to the armchair configuration, were observed.

According to the geometric structure of ripple and the projective characteristic of TEM observation, we proposed a strain-analysis method for identifying the rippled structure of $MoS_2$ nanosheet on atomic scale from HR-TEM images. We revealed the apparent strain in the HR-TEM image of rippled structure, and found its distribution was sensitive to the geometric structure of ripples. Therefore, the rippled structure can be estimated from the apparent strain of its HR-TEM image, and we demonstrated that the ripple structure could be quantitatively estimated at the sub-nanometer scale.

In the TEM observation, we found the rippled structure in the $MoS_2$ nanosheet, as it showed a periodic contrast and the latticed spacing was apparently modulated along the armchair orientation. By applying the GPA method to the HR-TEM image, the corresponding apparent strain distribution was obtained. By analyzing the apparent strain distribution of the rippled structure, we found that it was inclined sinusoidal ripple (approximately 7.1°) of 0.3 and 5.5 nm in amplitude and period, respectively.

Furthermore, our method is valid for the multilayer of $MoS_2$ nanosheet, since the periodicity of the apparent strain is always simple in the thicker sample. It is found that

the interlayer interaction between layers of $MoS_2$ nanosheet was suggested to be very weak, so that the bending of $MoS_2$ layers can be explained with the layer model, in which the in-plane distortion can be ignored due to weak interlayer interaction in multilayer sample. Additionally, the layer bending in $MoS_2$ nanosheet results in the appearance of atomic-scale ripple, due to the negligible bending resistance.

Therefore, we proposed a method to retrieve the ripple structure of 2D materials from the HR-TEM images, and our results proved such a method is effective for quantitatively estimating the ripple structure in 2D materials on the sub-nanometer scale.

# Chapter 6 Strain dependence of the ripple structure in $MoS_2$ nanosheet

## Introduction

This chapter contains the observation and analysis of the strain dependence of physical property in $MoS_2$ nanosheet. The in situ stretching experiments were conducted on the rippled structures in $MoS_2$ nanosheet and the mechanical response was revealed on atomic scale by analyzing the structural evolution of the ripple structure.

In Chapter 6.1, we show the in situ TEM observation of the $MoS_2$ nanosheet under stretching, the structural evolution of rippled structure is revealed. In Chapter 6.2, the strain dependence of the geometry of the rippled $MoS_2$ nanosheets is investigated. Based on the geometry analysis, the strain dependence of the Poisson's ratio is studied, and a structural model is proposed to reveal the increasing of Poisson's ratio under tensile strain, which is attributed to the change of bond length and angle.

## 6.1 The strain dependence of the ripple structure of $MoS_2$ nanosheet

Previously, the mechanical response of rippled 2D materials, such as graphene, and $MoS_2$, under strain conditions has been extensively studied through theoretical approaches such as molecular dynamics simulations [35,39]. The stretching of rippled graphene has been approximated with continuum mechanics [36], according to which the competition between the bending and stretching energy causes the period (λ) and amplitude ($A$) of the ripple to follow a 1/4-power scaling law with the longitudinally tensile strain ($\varepsilon$), such as $\lambda \sim \varepsilon^{-1/4}$ and $A \sim \varepsilon^{1/4}$. First-principle calculations have shown that the bending stiffness of graphene decreases as the stretching strain increases. However, the mechanical behavior of atomic-scale $MoS_2$ under tensile strain has been rarely reported. In this section, the strain dependence of the atomic-scale ripple structure in $MoS_2$ nanosheet was investigated by using in situ TEM equipped with a stretching function.

### *6.1.1 The initial ripple structure of $MoS_2$ nanosheet before stretching*

The TEM observation was carried out for structural analysis of the rippled $MoS_2$ nanosheet. The TEM image shows a periodic contrast modulation that the areas with and without clearly visible lattice fringes are alternately observed, suggesting the formation of the rippled structure, as shown in Fig. 6.1(a). This periodic structure is

arranged along the armchair direction (y-direction). We fabricated a hole in the $MoS_2$ nanosheet by bombarding it with a convergent electron beam to serve as a marker, as shown in the upper center of the image. The thickness of the $MoS_2$ layers was estimated to be 4.92 nm (8 layers), according to the visibilities of lattice and the Fresnel fringe, as we mentioned in the Chapter 2.1.4.

Figure 6.1(b) shows the corresponding apparent strain ($\varepsilon_{GPA}$) map obtained by applying GPA to the HR-TEM image of Fig. 6.1(a). The periodic distribution of apparent strain attributes to the projected lattice spacing in the HR-TEM image of periodically rippled structure. In the apparent strain map, as shown in Fig. 6.1(b), the regions of tensile (positive value) and compressive (negative value) strains seem to correspond to antinode and node of the ripple structure, respectively. In principle, in order to obtain the apparent strain map, it is required to specify a region in the HR-TEM image of Fig. 6.1(a) where the strain is zero to act as a reference region, but it is difficult to specify such a region due to the wavy structure of ripple. Theoretically, the apparent strain in the antinode region of the ripple structure should be almost zero when the incident electron beam is perpendicular to the sheet. Therefore, the experimental apparent strain is thought to have been shifted as the reference area deflected from the antinode region. We noticed that the ripple structures were always formed along the armchair direction. For simplicity, hereafter, the rippled $MoS_2$ nanosheet is discussed

by defining the zigzag and armchair direction as the x- and y-direction, respectively.

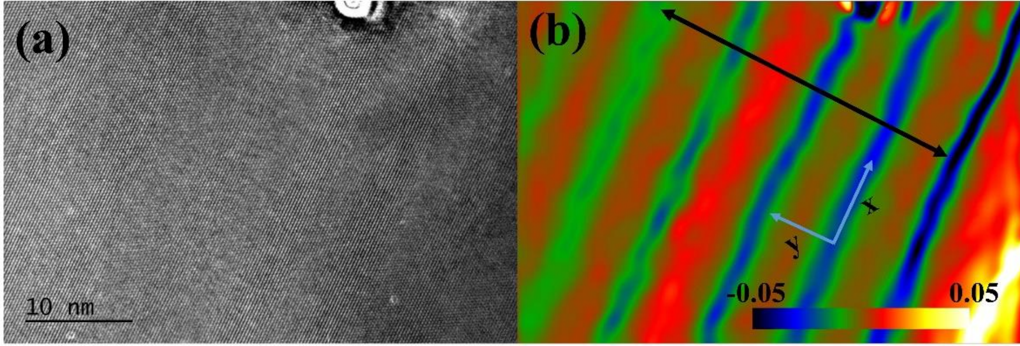


Figure 6.1. (a) TEM image of the rippled $MoS_2$ nanosheet. (b) Corresponding apparent strain map. The obtained strain was not adjusted, so the maximum strain was not zero.

According to the apparent strain map, as shown in Fig. 6.1(b), the amplitude of the ripple structure was obtained by comparing with the experimental HR-TEM image and corresponding apparent strain, as we demonstrate in Chapter 5.2. The ripple structure can be described as a sinusoidal pattern:

$$\zeta = A \sin \frac{2\pi y}{\lambda}, \tag{6.1}$$

where $\zeta$ is the out-of-plane displacement, $A$ is the amplitude, and $\lambda$ is the period. By comparison, the period and amplitude of the observed ripple were estimated to be 7.70±0.04 and 0.14±0.07 nm, respectively. Here, the error of the period indicates the standard deviation of measured data, and the errors of amplitudes are obtained from the estimation process with corresponding range in periods. The abnormal apparent strain in the lower right corner in Fig. 6.1(b) seemed to be attributed to a defect.

We found that the $MoS_2$ nanosheets had a ripple structure, even though they were not stretched by the piezo, indicating the existence of strain in the initial rippled structure. The shear or tensile strain may be induced to the nanosheet, because of the dry transfer method, in which the sample is contacted with the substrate on the Si chip directly. In Fig. 6.1(a), the initial ripple was observed to be parallel to the zigzag configuration, which had an angle of $\alpha$ (45°) to the boundary of the trench. Previously, the shear strain has been reported to generate the ripple structure not perpendicular to the trench for graphene [35,36,76,77] and thin polymer films [43,78]. It suggests that the observed ripple structures may be generated by the shear strain, which induced a tensile strain, because of similar geometrical relation. Taking into account that the ripple structures were 45° with respect to the trench edge, the initial shear-induced tensile strain $\varepsilon_{xsh}$ along with the stretching (x-) direction of the ripples can be described as:

$$\varepsilon_{xsh} = \frac{1}{2}\gamma \sin 2\alpha = \frac{\gamma}{2}. \quad (6.2)$$

Here, the initial shear strain was estimated to be 0.012, which was determined by the relationship between the tensile strain and the geometry of ripple structure in Chapter 6.21. Correspondingly, the total tensile strain, $\varepsilon_x$, which is equal to $\varepsilon_{xsh}$, can be estimated to be 0.60%.

### *6.1.2 The evolution of ripple structure during stretching*

In order to investigate the mechanical behavior of the ripple structure under tensile strain. The stretching of the ripple structure was achieved by increasing the applied bias voltage from zero to 10, 20, 30, and 40 V, which indicating the trench was stretched with corresponding applied strains ($\varepsilon_{appl}$) of 0.51%, 1.02%, 1.53%, and 2.04%, respectively. Fig. 6.3 shows the TEM images and corresponding apparent strain maps of the ripple structure under different stretching conditions. The apparent strain maps show that the period of the ripples decreased with increasing strain: 7.64±0.05, 7.48±0.04, 7.23±0.03, and 6.70±0.02 nm at applied strains ($\varepsilon_{appl}$) of 0.51%, 1.02%, 1.53%, and 2.04%, respectively.

We should notice that the strain applied on the ripple is different from the strain on the trench, as the rippled structure is 45° to the boundary of the trench. Notice that the ripple structure is formed by a tensile stress along the zigzag direction (tensile strain, $\varepsilon_x$) which induces transverse strain ($\varepsilon_y$). As we mentioned above, the zigzag/armchair direction is regarded as the x-/y-direction, since the ripple structures were always observed to form along the armchair direction regardless of the stretching direction, as shown in Fig. 6.2(a). It means we should estimate the applied tensile strain ($\varepsilon_{xap}$) on the sample during the stretching for quantitative analysis. Therefore, the tensile strain applied to the sample is estimated to be:

$$\varepsilon_{xap} = \varepsilon_{appl} \sin^2 \alpha \,, \tag{6.3}$$

where $\varepsilon_{appl}$ is the stretching strain applied on trench caused by the piezo actuator and $\alpha$ is the angle between the x-direction of the sample and the stretching direction, as shown in Fig.6.3(b). Thus, the tensile strain applied on the ripple is estimated from the strain applied on the trench during the stretching.

Therefore, the tensile strain ($\varepsilon_{xap}$) applied on the $MoS_2$ nanosheet during stretching can be estimated to be 0.26%, 0.51%, 0.77%, and 1.02%, when the applied strains ($\varepsilon_{appl}$) are 0.51%, 1.02%, 1.53%, and 2.04%, respectively.

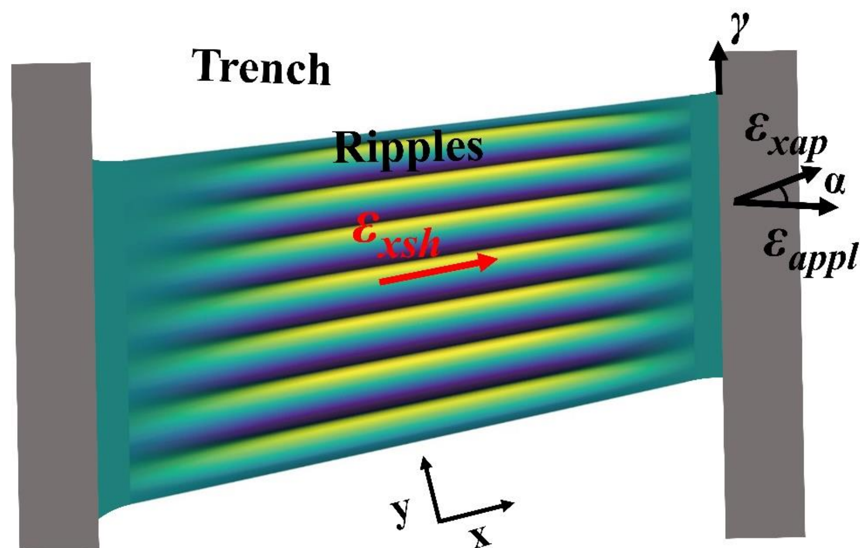


Figure 6.2. (a) Illustration of a $MoS_2$ nanosheet suspended on the trench of the Si chip, showing the ripple structure formed by stretching the nanosheet along the x-direction (corresponds to the direction along the zigzag edge), the ripple structure formed along the armchair edge marked by y. $\varepsilon_{appl}$: tensile strain applied to the trench because of stretching, $\varepsilon_{xap}$: tensile strain along the stretching direction of the ripple.

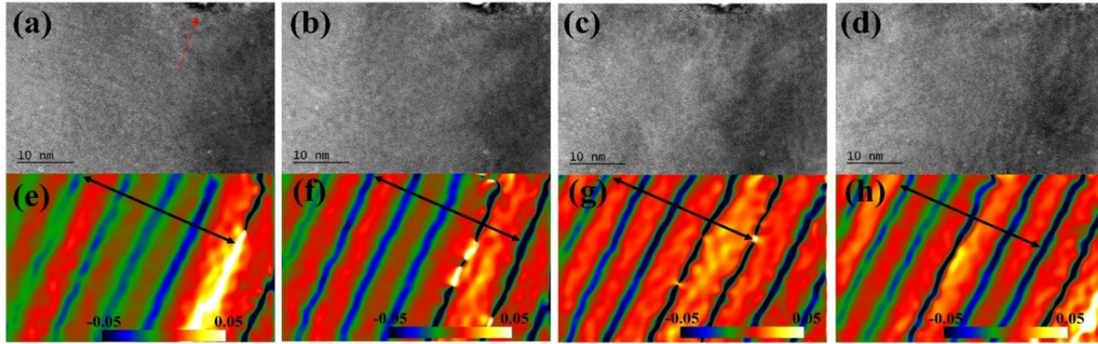


Figure 6.3. TEM images of rippled $MoS_2$ nanosheets with applied tensile strains ($\varepsilon_{xap}$) of (a) 0.34%, (b) 0.68%, (c) 1.02%, and (d) 1.36%, respectively; (e)–(h) Corresponding apparent strain maps. When converted, the $\varepsilon_x$ was estimated to be 0.86%, 1.11%, 1.36%, and 1.61%, respectively.

The period was estimated by averaging the four ripple patterns, as marked in Fig. 6.3. At each pattern, the period was determined by averaging among 6 different regions. Then, the lengths of the ripples within one period were obtained by a multiply of the number of lattice spacing with one period and the lattice spacing in combining the apparent strain map and atomic image, because it was confirmed that there was no in-plane strain in the rippling direction of rippled structures of $MoS_2$ nanosheet. With the period, the length of the ripple, and the Eq. (6.1), we can estimate the corresponding amplitudes, which were 0.16±0.07, 0.19±0.06, 0.26±0.05, and 0.29±0.04 nm, respectively. Thus, the evolution of ripple structure under stretching was revealed. Here, the error of amplitudes is a little larger than that of period, due to the estimation of

amplitude involves not only the statistical error from the period and the value of apparent strain but also the calculated error from the approximate calculation of the amplitude. Additionally, both the locally absorbed contaminate and the noise on the apparent strain can contribute to the error of apparent strain, thus result in the relatively large error of amplitude.

Considering that the initial ripple structure was induced by shear strain, and it was stretched by the tensile strain applied to the trench in our experiment. We estimated the total tensile strain ($\varepsilon_x$) of ripple, which is consisted of the initial shear-induced tensile strain ($\varepsilon_{xsh}$) and the applied tensile strain ($\varepsilon_{xap}$) induced by the stretching ($\varepsilon_{appl}$), to evaluate its mechanical response under stretching. With the ripple structures were stretched, the shear-induced tensile strain $\varepsilon_{xsh}$ changed with the $\varepsilon_{appl}$. The detailed strain analysis can be found in Appendix I. It was evaluated to understand the mechanical response under stretching. During the stretching, the initial tensile strain $\varepsilon_{xsh}$ changed from Eq. (6.2) to the following:

$$\varepsilon_{xsh} = \frac{1}{2}\frac{\gamma}{1+\varepsilon_{appl}}. \tag{6.4}$$

Combining Eqs. (6.3) and (6.4), and the rippled structure is 45° to the boundary of the trench, then the total tensile strain ($\varepsilon_x$) of the ripple during stretching can be defined as the sum of the strain-induced by shear and stretching:

$$\varepsilon_x = \varepsilon_{xsh} + \varepsilon_{xap} = \frac{1}{2}\left(\frac{\gamma}{1+\varepsilon_{appl}} + \varepsilon_{appl}\right). \tag{6.5}$$

Thus, the total tensile strains, $\varepsilon_x$, are estimated to be 0.6%, 0.86%, 1.11%, 1.36%, and 1.61%, respectively, when the applied strains ($\varepsilon_{appl}$) are 0, 0.51%, 1.02%, 1.53%, and 2.04%, respectively. The relationship between the geometric structure of the ripple and total tensile strain is obtained and showed in Fig.6.4.

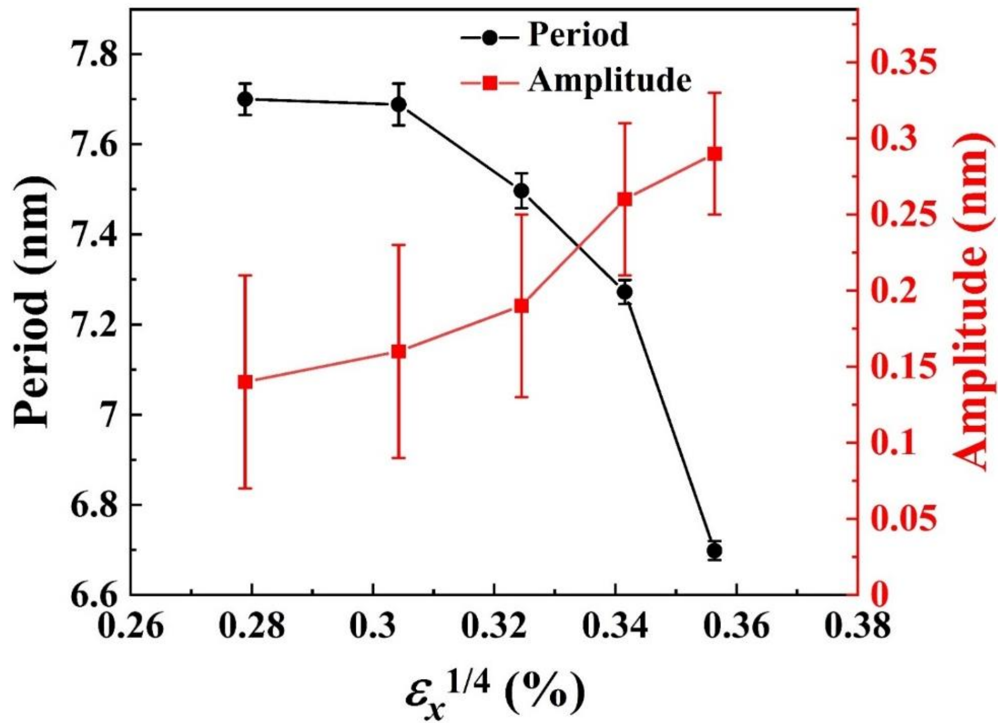


Figure 6.4. Relationships of the period and amplitude with $\varepsilon_x^{1/4}$.

It is found that the amplitude and period are not in proportion to $\varepsilon_x^{1/4}$, indicating that the ripple structure at the subnanometer scale does not follow the continuum mechanics. We think that this discrepancy must come from the inapplicable plate model [79] base on continuum mechanics.

## 6.2 The strain dependence of the Poisson's ratio of rippled $MoS_2$ nanosheet

Our experimental results showed that the evolution of ripple structures was not followed the continuum mechanics, hereby, we perform the analysis on the relationship between the tensile strain and the geometry of ripple structure for clarifying the such a structure evolution.

### *6.2.1 The strain dependence of the geometry of rippled structure*

The rippled structure is formed under a longitudinally tensile strain as schematically illustrated in Fig. 6.5. For simplicity, it is assumed that the nanosheet is stretched along the zigzag edge. The width of the nanosheet should be compressed along the transverse direction by stretching due to the Poisson effect. The transverse strain can be described as $\varepsilon_y = -\varepsilon_x \nu$ . The nanosheet cannot form the ripple structure near the clamped boundary as indicated by red arrows in Fig. 6.5, but it is compressed along the transverse direction (no out-of-plane displacement). While, at the middle, the nanosheet forms the ripple structure along the transverse direction as illustrated in Fig. 6.5. We suppose that out-of-plane displacement is hardly occurred due to physical restrictions near the clamped boundary and the ripple structure is more stable than the compressed structure without out-of-plane displacement.

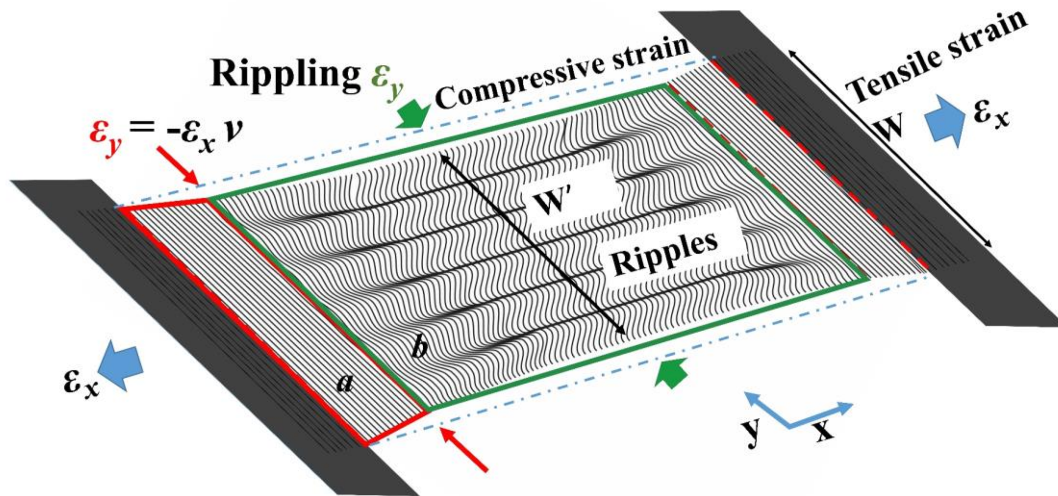


Figure 6.5. Diagram of the formation of the ripple structure under tensile strain. The ripple structure was formed due to the transverse strain ($\varepsilon_y$). *W* is the initial width of the sample before rippling, *W'* is the projected width of the ripple structure. The region ***a*** and ***b*** indicate the non-rippled and rippling region.

The transverse strain ($\varepsilon_y$) induced by total tensile strain ($\varepsilon_x$), which is the sum of $\varepsilon_{xsh}$ and $\varepsilon_{xap}$, is related by Poisson's ratio (ν) as follows,

$$\varepsilon_y = -\varepsilon_x \nu \,. \tag{6.6}$$

Substituting Eq. (6.6) into Eq. (6.5), we obtained:

$$\varepsilon_y = -\varepsilon_x \nu = -\frac{1}{2}\left(\frac{\gamma}{1+\varepsilon_{appl}} + \varepsilon_{appl}\right)\nu \,. \tag{6.7}$$

Taking the geometry of the ripple structure into account, the transverse strain ($\varepsilon_y$) (as shown in region ***a*** of Fig. 6.5), which is equal to the transverse strain due to rippling (as

shown in region ***b*** of Fig. 6.5), can be also described by the ratio of both widths of the sheet before and after rippling ($W$ and $W'$, which is shown in Fig.6.5) as follows.

$$\varepsilon_y \equiv -\frac{\Delta}{W} \equiv \frac{W' - W}{W}. \tag{6.8}$$

Assuming that the in-plane strain in the ripple structure is negligible, the length of the rippled sheet should be equal to the width of the non-rippled sheet, such as:

$$W = \int_0^{W'} \sqrt{1 + (\partial_y \zeta)^2} dy \approx \int_0^{W'} \left[ 1 + \frac{1}{2} (\partial_y \zeta)^2 \right] dy. \tag{6.9}$$

Also, the relation between these two widths can be described by:

$$\int_0^W \left[ \frac{1}{2} (\partial_y \zeta)^2) - \frac{\Delta}{W} \right] dy = 0, \tag{6.10}$$

where $\Delta$ is the difference in width, $\Delta = W - W'$. This assumption satisfies the inextensibility condition. From this condition, the following formula about the transverse strain $\varepsilon_y$ [41]:

$$\varepsilon_y = -\frac{\pi^2 A^2}{2\lambda^2}. \tag{6.11}$$

Equation (6.11) shows the relationship between the ripple geometry and transverse strain. From combining Eqs. (6.7) and (6.11), we obtain:

$$\varepsilon_y = -\varepsilon_x \nu = -\frac{1}{2} \left( \frac{\gamma}{1 + \varepsilon_{appl}} + \varepsilon_{appl} \right) \nu = -\frac{\pi^2 A^2}{2\lambda^2}. \tag{6.12}$$

Thus, the relationship between the strain and the geometry of the ripple structure was revealed. The initial shear strain was estimated to be $\gamma \approx 0.012$, when $\varepsilon_{appl}$ is zero, and Poisson's ratio was assumed to be the bulk value of $\nu = 0.27$ [6,80], by using Eq. (6.12).

### *6.2.2 The strain dependence of Poisson's ratio*

The relationship between the total tensile strain and the transverse strain was obtained, as shown in Fig. 6.6(a). Here the error bar indicates the errors obtained from the estimation process by Eq. (6.12), which origin from the errors in the periods and amplitudes. It shows nonlinear behavior that suggests the Poisson's ratio is not constant when increasing the tensile strain by considering Eq. (6.16). According to Eq. (6.12), $v$ can be obtained from experimental results as follows:

$$v = \frac{\pi^2 A^2}{2\varepsilon_x \lambda^2} = \frac{\pi^2 A^2}{(\frac{\gamma}{1+\varepsilon_{appl}} + \varepsilon_{appl})\lambda^2}. \tag{6.13}$$

Each Poisson's ratio ($v$) was determined by substituting the experimental values to Eq. (6.13) as shown in Fig. 6.6(b). The error bars were caused not only the statistical errors but also by variation in the amplitudes and periods of the ripple structures. Even if the errors are taken into consideration, we can confirm that the Poisson's ratio changes with respect to the tensile strain. It is found that the Poisson's ratio ($v$) is almost constant when the total tensile strain ($\varepsilon_x$) is small (~1.1%). When the total tensile strain is increased to ~1.6%, $v$ increases from 0.27 to ~0.57. The variable value of $v$ during the increase in strain represents a nonlinear elastic response of $MoS_2$ nanosheet, and it could contribute to the failure of continuum mechanics at the atomic scale because the Poisson's ratio is not constant when the strain is increasing.

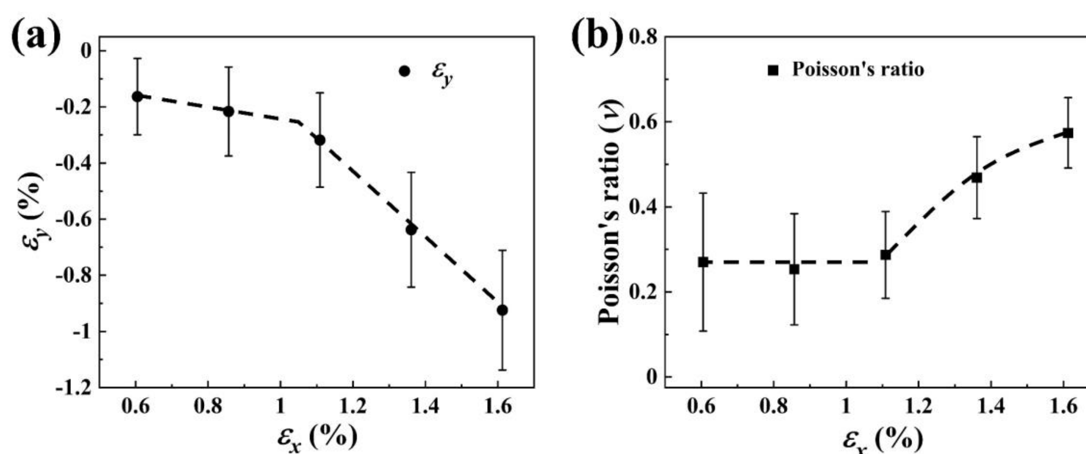


Figure 6.6. Relationships between the (a) total tensile strain $\varepsilon_x$ and imposed transverse strain $\varepsilon_y$ and (b) total tensile strain $\varepsilon_x$ and estimated Poisson's ratio.

Our results showed that atomic-scale $MoS_2$ nanosheets have nonlinear elastic properties. Regardless of the direction of the stretching, the ripple structure was formed along with the armchair (y-) direction by stretching the nanosheet along the zigzag (x-) direction. The observed ripple structure had the period and amplitude at the subnanometer scale. We found that the Poisson's ratio, which was estimated by the ratio of the longitudinal tensile and transversely compressive strains, was variable depending on the stretching.

Previously, the first-principles calculations [81,82] expected that the Poisson's ratio decreased with increasing the strain in 2D honeycomb materials such as graphene, silicene, h-BN, and h-GaN. However, there is no experimental report on this issue. Our results showed the tensile strain dependence of the Poisson's ratio even when the strain

was quite small (~1%), as shown in Fig. 6.6(b). The Poisson's ratio is found to be close to 0.27, which corresponds to the bulk value, when the total tensile strain is below ~1.1%. Meanwhile, it increases gradually with the tensile strain above ~1.1%. Such a strain dependence of Poisson's ratio revealed the nonlinear mechanical response of $MoS_2$ layers on atomic scale.

The ripple structure of the $MoS_2$ nanosheet is bridged between the two substrates via non-ripple regions near the clamped boundary, as shown in the illustration of Fig. 6.5. In such non-ripple regions, the ripple structure does not occur due to physical restrictions as described above. But the width in the transverse direction is narrowed, when the $MoS_2$ nanosheet is stretched along the x-direction. It means that, in the non-ripple regions, the strain occurs in the plane, such as changes in the bond length of Mo atoms and changes in the bond angle. Therefore, we think that the bond length of Mo atoms and the bond angle will change depending on the tensile strain and the width of the non-ripple regions will be determined by these changes. Taking into account that the width of the non-ripple regions should be the same with one of the ripple structure due to smooth connection, we suppose that the amplitude and period of the ripple structure are determined by the width of the non-ripple regions.

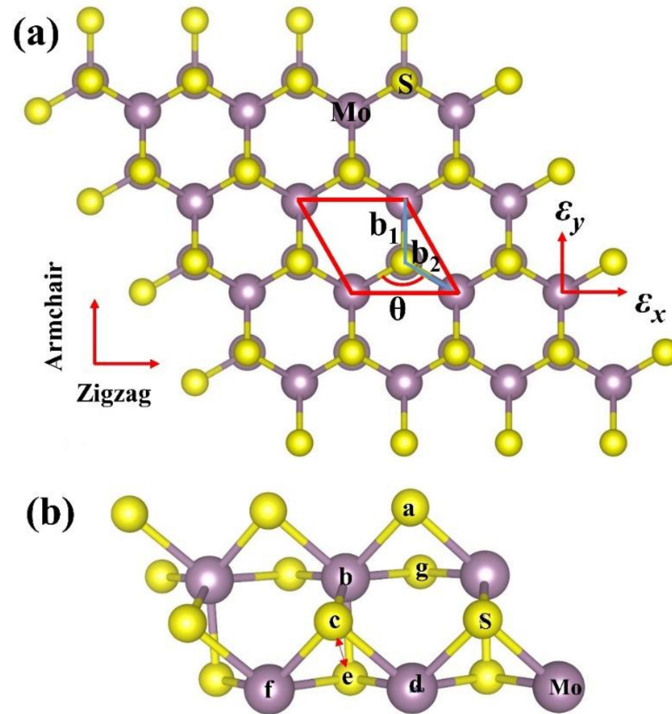


Figure. 6.7. (a) Top view of the lattice structure of $MoS_2$ with projected geometry parameters ($b_1$, $b_2$, and θ), The $\varepsilon_x$ and $\varepsilon_y$ represent the tensile strain by stretching and compressive strain due to Poisson's effect. The purple and yellow atoms indicate the Molybdenum and sulfur atoms, respectively. (b) Stereogram of the $MoS_2$ structure, a-d present different atoms.

We consider that the Poisson's ratio of $MoS_2$ nanosheet is related to its atomic arrangement, which is determined by the bond length between two neighbor Mo atoms and the bond angle under the tensile strain, as shown in Fig. 6.7 (a) and (b). We analyze the in-plane strain of the $MoS_2$ (Fig. 6.7) to explain the experimental strain dependence of the Poisson's ratio in Fig. 6.6(b). In the structural model of Fig. 6.7(a), we assume

that the bond length of Mo atoms perpendicular to the zigzag direction ($b_1$), the bond length of Mo atoms along with the zigzag configuration ($b_2$), and the bond angle between two neighbor bonds along with the zigzag configuration ($\theta$) changes as a function of the tensile strain ($\varepsilon_x$). By applying the tensile strain, when the changes in the bond length ($b_1$, $b_2$) and angle ($\theta$) are defined as $\Delta b_1$, $\Delta b_2$, and $\Delta\theta$, respectively. And, the change rate of the bond lengths are defined by $\varepsilon_1 = \frac{\Delta b_1}{b}$ and $\varepsilon_2 = \frac{\Delta b_2}{b}$, respectively. The lattice constant along the x-direction (zigzag) and y-direction (armchair) are $2b_2 \sin\frac{\theta}{2}$ and $b_1 + b_2 \cos\frac{\theta}{2}$, respectively. Thus, the tensile strain $\varepsilon_x$ can be expressed as:

$$\begin{aligned}\varepsilon_x &= \frac{2(b_2+\Delta b_2)\sin\frac{\theta+\Delta\theta}{2} - 2b_2\sin\frac{\theta}{2}}{2b_2\sin\frac{\theta}{2}} \approx \frac{\Delta b_2}{b_2} + \frac{\Delta\theta}{2}\cot\frac{\theta}{2} \\ &= \varepsilon_2 + \frac{\Delta\theta}{2}\cot\frac{\theta}{2}\end{aligned} . \quad (6.14)$$

And the corresponding transverse strain $\varepsilon_y$:

$$\begin{aligned}\varepsilon_y &= \frac{b_1+\Delta b_1+(b_2+\Delta b_2)\cos\frac{\theta+\Delta\theta}{2} - b_1 - b_2\cos\frac{\theta}{2}}{b_1+b_2\cos\frac{\theta}{2}} \\ &= \frac{\Delta b_1 - b_2\frac{\Delta\theta}{2}\sin\frac{\theta}{2} + \Delta b_2\cos\frac{\theta}{2}}{b_1+b_2\cos\frac{\theta}{2}}\end{aligned} . \quad (6.15)$$

By taking into account that the initial projected bond length $b=b_1=b_2$ and $\theta$=120°, the Poisson's ratio can be demonstrated as:

$$v = -\frac{\varepsilon_y}{\varepsilon_x} = -\frac{1}{\varepsilon_x}\left(\frac{2}{3}\varepsilon_1 - \frac{\sqrt{3}\Delta\theta}{6} + \frac{1}{3}\varepsilon_2\right) . \quad (6.16)$$

Here the Poisson's ratio is expressed by the function of $\varepsilon_1$, $\varepsilon_2$, and $\Delta\theta$. At constant Poisson's ratio ($\nu$ = 0.27), the rate of change in the bond length along the direction orthogonal to the zigzag direction shows almost a linear relation with that along the zigzag direction ($\varepsilon_1 \sim -0.02\ \varepsilon_2$). Therefore, as shown in Fig. 6.8(a), the dependence of $\varepsilon_x$ on $\varepsilon_2$ is considered by the following three assumptions: (1) $\varepsilon_2$ is proportional to $\varepsilon_x$, (2) $\varepsilon_2 = 0$, and (3) $\varepsilon_2$ is proportional to $\varepsilon_x$ up to 1% and becomes constant for values beyond 1%. Using Eq. (6.14), the dependence of the $\varepsilon_x$ on the change in bond angle, $\Delta\theta$, is obtained for the three assumptions, as shown in Fig. 6.8(b). With respect to assumption (1), $\Delta\theta$ is also observed to be proportional to $\varepsilon_x$. In assumption (2), $\Delta\theta$ is proportional to the $\varepsilon_x$ with higher slope than the one calculated in assumption (1). In the case of assumption (3), the slope of $\Delta\theta$ shows an increase when the $\varepsilon_x$ is 1.1%.

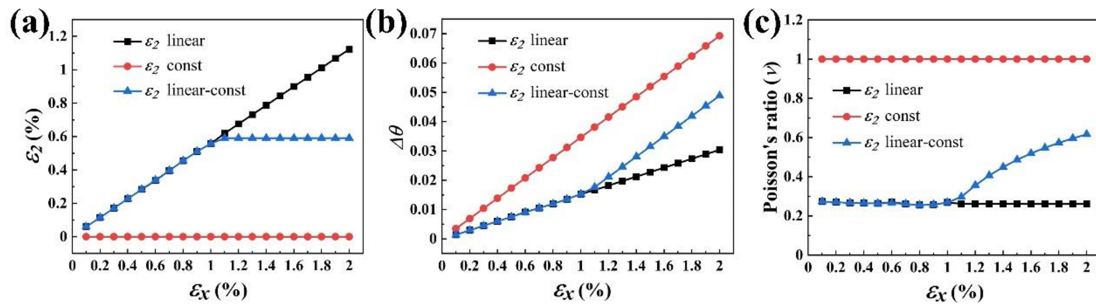


Figure. 6.8. (a) Three relationships between $\varepsilon_x$ and $\varepsilon_2$ ( $\varepsilon_2$ is the rate of change in the $b_2$: $\varepsilon_2 = \frac{\Delta b_2}{b_2}$ ) obtained by three different assumptions as shown in the legend (liner, constant and linear-constant). (b) The three relationships between $\varepsilon_x$ and $\Delta\theta$ ($\Delta\theta$ is the change in bond angle $\theta$). (c) The three relationships between $\varepsilon_x$ and the calculated Poisson's ratio.

The dependence of the tensile strain on Poisson's ratio for the three different assumptions are calculated using Eq. (6.16), as shown in Fig. 6.8(c). In the cases of assumptions (1) and (2), $v$ is noticed to be almost constant at 0.27 and 1, respectively, regardless of $\varepsilon_x$. On the other hand, in the case of assumption (3), $v$ is found to be almost constant at 0.27 for the $\varepsilon_x$ below 1.1% and it gradually increases above $\varepsilon_x$ of 1.1%. These results indicate that an increase in $v$ is contributed by the constant $\varepsilon_2$ when $\varepsilon_x$ is larger than 1%. As the constant $\varepsilon_2$ with increasing $\varepsilon_x$ will lead to the raising increment of $\theta$, as demonstrated in Eq. (6.14), that results in the reduced $\varepsilon_y$ and correspondingly increased $v$, as shown in Eqs. (6.15) and (6.16). We find that the model based on the assumption (3) matches well with the experimental results as shown in Fig. 6.6(b). The results seem to be reasonable, as we consider that the energy required to alter the bond angle may be lower than the energy required to change the bond length in the stretching. The strain dependence of Poisson's ratio also agrees well with the previous studies based on first-principles calculations [83,84],, which showed an increase in Poisson's ratio of $MoS_2$ layer by stretching the nanosheets along the zigzag direction.

In conclusion, by analyzing the rippled structure under stretching, we experimentally revealed the geometric evolution of the atomic-scale$MoS_2$ nanosheet, which have been subjected to stretching using in situ TEM. It was found that the continuum mechanic was inapplicable for the atomic-scale ripple structures, because of the invalid plate

model, and it can be explained by the layer model. Additionally, we retrieved the nonlinear mechanical response of the $MoS_2$ layer: Poisson's ratio was constant below the tensile strain of 1.1%, while it gradually increased for the tensile strain higher than 1.1%. This nonlinearity can be explained by the structural model that the bond length does not change in proportion to the tensile strain above 1.1%. Although the strain dependence of Poisson's ratio for 2D materials has been reported by MD simulations or first-principles calculations [85], experimental results have been reported rarely. In this sense, our experimental results are extremely important in clarifying the mechanical response of $MoS_2$ or 2D materials on atomic scale.

## 6.3 Conclusion

In this chapter, we experimentally investigated the mechanical response of $MoS_2$ nanosheets under strain conditions. By applying GPA to TEM images, the ripple structure of $MoS_2$ nanosheets being stretched was obtained based on its apparent strain. We studied the geometric evolution of rippled structure with the increased tensile strain, and investigated the strain dependence of its mechanical behavior.

The strain dependence of the ripple structure of the $MoS_2$ nanosheet is revealed based on the in situ stretching experiment. It was found that the relationship between the tensile strain $\varepsilon_x$ and the amplitude/period was not followed with the 1/4 power scale low, which means the continuum mechanics is failed in explaining the behavior of 2D materials at the atomic scale.

By analyzing the strain dependence of the geometry of the ripple structure, we obtained the relationship between the applied tensile strain and the estimated Poisson's ratio. Thus, the strain dependence of Poisson's ratio of $MoS_2$ nanosheet was revealed, it was found that the $\nu$ was constant below the tensile strain of 1.1% and it increased to 0.57 with the strain increased to ~1.6%. Based on our structural model, such a nonlinear strain dependence of Poisson's ratio was found to be originated from the atomic-scale bonding response under stretching, due to the bond length does not change in proportion to the tensile strain. The results of our geometric analysis indicate that it can potentially

be applied for estimating the Poisson's ratio of 2D materials.

Such a strain-dependent mechanical property is important for understanding the physical and chemical properties of 2D materials. The in situ TEM observation in this study clarified the inherent nonlinearity, which is important in understanding the specific mechanical properties of 2D materials. The obtained mechanical behavior of 2D materials under strain conditions can potentially be used for understanding their mechanical properties at the atomic scale and developing future applications.

# Chapter 7 Summary

Understanding the physical properties of $MoS_2$ under strain conditions is essential for its application in electronic devices. In this work, we developed an intuitively experimental method to investigate the strain dependence of physical properties of $MoS_2$ on atomic scale.

We developed an in situ stretching TEM holder, which was designed for the purpose of investigating the strain dependence of 2D materials. The atomic-scale TEM image and a linear relationship between the applied bias voltage of the piezo actuator and the trench distance were achieved, indicating that it was stable and effective for the in situ stretching TEM observation. The displacement step of the holder was measured to be 0.06 nm/mV that is applicable for stretching on atomic scale.

We performed in situ stretching TEM observations of the $MoS_2$ nanosheet by our developed TEM holder for investigating the mechanical response of $MoS_2$ under stretching. The fracture process of a multilayer $MoS_2$ nanosheet was studied, in which the crack of the sample was propagated along the zigzag edge layer by layer. Our results suggested that the fracture of $MoS_2$ nanosheet is an interlayer fracture with a zigzag propagated orientation. In the meanwhile, the structural modulation of the $MoS_2$ nanosheet under 0.7% tensile strain was also found. The periodically atomic-contrast

change during stretching was revealed, it was attributed to the out-of-plane displacement of the sample during stretching.

The periodic ripple structures of the $MoS_2$ nanosheet, which formed parallel to the armchair configuration, were observed in the $MoS_2$ nanosheet. According to the geometric structure of ripple and the projective characteristic of TEM observation, we proposed a strain-analysis method for identifying the rippled structure of $MoS_2$ nanosheet on atomic scale from HR-TEM images. We revealed the apparent strain in the HR-TEM image of rippled structure, and found its distribution was sensitive to the geometric structure of ripples. Therefore, the rippled structure can be quantitatively estimated from the apparent strain of the HR-TEM image at the sub-nanometer scale. By analyzing the apparent strain distribution of the rippled structure, we found that it was described to be inclined sinusoidal function (approximately 7.1°) of 0.3 and 5.5 nm in amplitude and period, respectively. Furthermore, our method is valid for the multilayer of $MoS_2$ nanosheet, since the periodicity of the apparent strain is always simple in the thicker sample. The interlayer interaction between layers of $MoS_2$ nanosheet was suggested to be very weak, so that the bending of $MoS_2$ layers can be explained with the layer model, in which the in-plane distortion can be ignored due to weak interlayer interaction in multilayer sample. Due to the layer bending, the bending resistance of multilayer $MoS_2$ nanosheet should be quite small that the atomic-scale

ripple structures could formed.

We experimentally investigated the mechanical response of $MoS_2$ nanosheets under strain conditions. By using our strain-based analysis on TEM image. The geometric evolution with increasing tensile strain was revealed. The relationship between the total tensile strain $\varepsilon_x$ and the amplitude/period did not follow the 1/4-power scaling law, indicating the continuum mechanics was failed in explaining the ripple structure of 2D materials at the atomic scale. We investigated the relationship between the applied tensile strain and geometry of the rippled structure, by analyzing the strain dependence of the geometry of the ripple structure. We estimated the Poisson's ratio of $MoS_2$ nanosheet from such experimental results and found that the $\nu$ increased to 0.57 with the strain increased to ~1.6%. We proposed the structural model, which revealed that the increase of the Poisson's ratio was originated from the bond length that does not change in proportion to the tensile strain.

In summary, this study provides an experimental method for investigating the strain dependence of physical properties of 2D materials. We propose a strain-analysis method for identifying the rippled structure with TEM images. Based on the revealed rippled structure, we can analyze the strain dependence of the geometry of the ripple structure of $MoS_2$ layers and obtain the relationship between the tensile strain and Poisson's ratio. The results of our geometric analysis indicate that it can potentially be applied for

estimating the strain dependence of the structural and mechanical properties of 2D materials, which can potentially be used for understanding their mechanical properties at the atomic scale and developing future applications.

# References


[1] K. S. Novoselov, A. K. Geim, S. V. Morozov, D. Jiang, Y. Zhang, S. V. Dubonos, I. V. Grigorieva, and A. A. Firsov, *Electric Field Effect in Atomically Thin Carbon Films*, Science **306**, 666 (2004).

[2] C. Lee, X. Wei, J. W. Kysar, and J. Hone, *Measurement of the Elastic Properties and Intrinsic Strength of Monolayer Graphene*, Science **321**, 385 (2008).

[3] A. K. Geim and K. S. Novoselov, *The Rise of Graphene*, Nature Mater **6**, 183 (2007).

[4] K. S. Novoselov, A. K. Geim, S. V. Morozov, D. Jiang, M. I. Katsnelson, I. V. Grigorieva, S. V. Dubonos, and A. A. Firsov, *Two-Dimensional Gas of Massless Dirac Fermions in Graphene*, Nature **438**, 197 (2005).

[5] A. Castellanos-Gomez, M. Poot, G. A. Steele, H. S. J. van der Zant, N. Agraït, and G. Rubio-Bollinger, *Elastic Properties of Freely Suspended $MoS_2$ Nanosheets*, Adv. Mater. **24**, 772 (2012).

[6] S. Bertolazzi, J. Brivio, and A. Kis, *Stretching and Breaking of Ultrathin $MoS_2$*, ACS Nano **5**, 9703 (2011).

[7] T. Mukhopadhyay, A. Mahata, S. Adhikari, and M. Asle Zaeem, *Effective Elastic Properties of Two Dimensional Multiplanar Hexagonal Nanostructures*, 2D Mater. **4**, 025006 (2017).

[8] K. Kaasbjerg, K. S. Thygesen, and K. W. Jacobsen, *Phonon-Limited Mobility in n-Type Single-Layer $MoS_2$ from First Principles*, Phys. Rev. B **85**, 115317 (2012).

[9] K. F. Mak, C. Lee, J. Hone, J. Shan, and T. F. Heinz, *Atomically Thin $MoS_2$: A New Direct-Gap Semiconductor*, Physical Review Letters **105**, (2010).

[10] Y. Zhang, J. Ye, Y. Matsuhashi, and Y. Iwasa, *Ambipolar $MoS_2$ Thin Flake Transistors*, Nano Lett. **12**, 1136 (2012).

[11] A. Castellanos-Gomez, R. Roldán, E. Cappelluti, M. Buscema, F. Guinea, H. S. J. van der Zant, and G. A. Steele, *Local Strain Engineering in Atomically Thin $MoS_2$*, Nano Letters **13**, 5361 (2013).

[12] R. C. Cooper, C. Lee, C. A. Marianetti, X. Wei, J. Hone, and J. W. Kysar, *Nonlinear Elastic Behavior of Two-Dimensional Molybdenum Disulfide*, Phys. Rev. B **87**, 035423 (2013).

[13] Q. H. Wang, K. Kalantar-Zadeh, A. Kis, J. N. Coleman, and M. S. Strano, *Electronics and Optoelectronics of Two-Dimensional Transition Metal Dichalcogenides*, Nature Nanotechnology **7**, 699 (2012).

[14] H. S. Lee, S.-W. Min, Y.-G. Chang, M. K. Park, T. Nam, H. Kim, J. H. Kim, S. Ryu, and S. Im, *$MoS_2$ Nanosheet Phototransistors with Thickness-Modulated Optical Energy Gap*, Nano Lett. **12**, 3695 (2012).

[15] F. Schwierz, *Graphene Transistors*, Nature Nanotech **5**, 487 (2010).

[16] J. S. Bunch, A. M. van der Zande, S. S. Verbridge, I. W. Frank, D. M. Tanenbaum, J. M. Parpia, H. G. Craighead, and P. L. McEuen, *Electromechanical Resonators from Graphene Sheets*, Science **315**, 490 (2007).

[17] G. Eda and M. Chhowalla, *Chemically Derived Graphene Oxide: Towards Large-Area Thin-Film Electronics and Optoelectronics*, Adv. Mater. **22**, 2392 (2010).

[18] A. McCreary, O. Kazakova, D. Jariwala, and Z. Y. Al Balushi, *An Outlook into the Flat Land of 2D Materials beyond Graphene: Synthesis, Properties and Device Applications*, 2D Mater. **8**, 013001 (2020).

[19] I. Song, C. Park, and H. C. Choi, *Synthesis and Properties of Molybdenum Disulphide: From Bulk to Atomic Layers*, RSC Adv. **5**, 7495 (2015).

[20] K. Momma and F. Izumi, VESTA 3 *for Three-Dimensional Visualization of Crystal, Volumetric and Morphology Data*, Journal of Applied Crystallography **44**, 1272 (2011).

[21] F. Wypych and R. Schöllhorn, *1T-$MoS_2$, a New Metallic Modification of Molybdenum Disulfide*, J. Chem. Soc., Chem. Commun. 1386 (1992).

[22] K. Kobayashi and J. Yamauchi, *Electronic Structure and Scanning-Tunneling-Microscopy Image of Molybdenum Dichalcogenide Surfaces*, Phys. Rev. B **51**, 17085 (1995).

[23] W. S. Yun, S. W. Han, S. C. Hong, I. G. Kim, and J. D. Lee, *Thickness and Strain Effects on Electronic Structures of Transition Metal Dichalcogenides: 2H- $MX_2$ Semiconductors ( M = Mo, W; X = S, Se, Te)*, Phys. Rev. B **85**, 033305 (2012).

[24] Z. Dai, L. Liu, and Z. Zhang, *Strain Engineering of 2D Materials: Issues and Opportunities at the Interface*, Adv. Mater. **31**, 1805417 (2019).

[25] Z. Li, Y. Lv, L. Ren, J. Li, L. Kong, Y. Zeng, Q. Tao, R. Wu, H. Ma, B. Zhao, D. Wang, W. Dang, K. Chen, L. Liao, X. Duan, X. Duan, and Y. Liu, *Efficient Strain Modulation of 2D Materials via Polymer Encapsulation*, Nat Commun **11**, 1151 (2020).

[26] Y. Sun and K. Liu, *Strain Engineering in Functional 2-Dimensional Materials*, Journal of Applied Physics **125**, 082402 (2019).

[27] S. Yu, H. D. Xiong, K. Eshun, H. Yuan, and Q. Li, *Phase Transition, Effective Mass and Carrier Mobility of $MoS_2$ Monolayer under Tensile Strain*, Applied Surface Science **325**, 27 (2015).

[28] E. Scalise, M. Houssa, G. Pourtois, V. Afanas'ev, and A. Stesmans, *Strain-Induced Semiconductor to Metal Transition in the Two-Dimensional Honeycomb Structure of $MoS_2$*, Nano Research **5**, 43 (2012).

[29] J. C. Meyer, A. K. Geim, M. I. Katsnelson, K. S. Novoselov, T. J. Booth, and S. Roth, *The Structure of Suspended Graphene Sheets*, Nature **446**, 60 (2007).

[30] A. Fasolino, J. H. Los, and M. I. Katsnelson, *Intrinsic Ripples in Graphene*, Nature Materials **6**, 858 (2007).

[31] J. Brivio, D. T. L. Alexander, and A. Kis, *Ripples and Layers in Ultrathin $MoS_2$ Membranes*, Nano Letters **11**, 5148 (2011).

[32] J. H. Warner, Y. Fan, A. W. Robertson, K. He, E. Yoon, and G. D. Lee, *Rippling Graphene at the Nanoscale through Dislocation Addition*, Nano Lett. **13**, 4937 (2013).

[33] Y. Liu and B. I. Yakobson, *Cones, Pringles, and Grain Boundary Landscapes in Graphene Topology*, Nano Lett. **10**, 2178 (2010).

[34] K.-K. Bai, Y. Zhou, H. Zheng, L. Meng, H. Peng, Z. Liu, J.-C. Nie, and L. He, *Creating One-Dimensional Nanoscale Periodic Ripples in a Continuous Mosaic Graphene Monolayer*, Physical Review Letters **113**, 086102 (2014).

[35] Z. Wang and M. Devel, *Periodic Ripples in Suspended Graphene*, Phys. Rev. B **83**, 125422 (2011).

[36] W. Bao, F. Miao, Z. Chen, H. Zhang, W. Jang, C. Dames, and C. N. Lau, *Controlled Ripple Texturing of Suspended Graphene and Ultrathin Graphite Membranes*, Nature Nanotechnology **4**, 562 (2009).

[37] A. L. Vázquez de Parga, F. Calleja, B. Borca, M. C. G. Passeggi, J. J. Hinarejos, F. Guinea, and R. Miranda, *Periodically Rippled Graphene: Growth and Spatially Resolved Electronic Structure*, Physical Review Letters **100**, (2008).

[38] L. Meng, Y. Su, D. Geng, G. Yu, Y. Liu, R.-F. Dou, J.-C. Nie, and L. He, *Hierarchy of Graphene Wrinkles Induced by Thermal Strain Engineering*, Applied Physics Letters **103**, 251610 (2013).

[39] S. Luo, G. Hao, Y. Fan, L. Kou, C. He, X. Qi, C. Tang, J. Li, K. Huang, and J. Zhong, *Formation of Ripples in Atomically Thin* $MoS_2$ *and Local Strain Engineering of Electrostatic Properties*, Nanotechnology **26**, 105705 (2015).

[40] S. Deng and V. Berry, *Increased Hierarchical Wrinklons on Stiff Metal Thin Film on a Liquid Meniscus*, ACS Applied Materials & Interfaces **8**, 24956 (2016).

[41] E. Cerda and L. Mahadevan, *Geometry and Physics of Wrinkling*, Physical Review Letters **90**, 074302 (2003).

[42] E. Cerda, K. Ravi-Chandar, and L. Mahadevan, *Wrinkling of an Elastic Sheet under Tension*, Nature **419**, 579 (2002).

[43] W. Wong and S. Pellegrino, *Wrinkled Membranes II: Analytical Models*, Journal of Mechanics of Materials and Structures **1**, 27 (2006).

[44] D.-B. Zhang, E. Akatyeva, and T. Dumitrică, *Bending Ultrathin Graphene at the Margins of Continuum Mechanics*, Physical Review Letters **106**, (2011).

[45] S. Xiong and G. Cao, *Bending Response of Single Layer $MoS_2$*, Nanotechnology **27**, 105701 (2016).

[46] J.-W. Jiang, Z. Qi, H. S. Park, and T. Rabczuk, *Elastic Bending Modulus of Single-Layer Molybdenum Disulfide ($MoS_2$): Finite Thickness Effect*, Nanotechnology **24**, 435705 (2013).

[47] G. Wang, Z. Dai, J. Xiao, S. Feng, C. Weng, L. Liu, Z. Xu, R. Huang, and Z. Zhang, *Bending of Multilayer van Der Waals Materials*, Phys. Rev. Lett. **123**, 116101 (2019).

[48] T. M. G. Mohiuddin, A. Lombardo, R. R. Nair, A. Bonetti, G. Savini, R. Jalil, N. Bonini, D. M. Basko, C. Galiotis, N. Marzari, K. S. Novoselov, A. K. Geim, and A. C. Ferrari, *Uniaxial Strain in Graphene by Raman Spectroscopy: G Peak Splitting, Grüneisen Parameters, and Sample Orientation*, Phys. Rev. B **79**, 205433 (2009).

[49] J. Zhao, W. Chen, J. Meng, H. Yu, M. Liao, J. Zhu, R. Yang, D. Shi, and G. Zhang, *Integrated Flexible and High-Quality Thin Film Transistors Based on Monolayer $MoS_2$*, Adv. Electron. Mater. **2**, 1500379 (2016).

[50] J. Xiang, W. Wang, L. Feng, C. Feng, M. Huang, P. Liu, X. Ren, and B. Xiang, *A Biaxial Strain Sensor Using a Single $MoS_2$ Grating*, Nanoscale Res Lett **16**, 31 (2021).

[51] E. Okogbue, J. H. Kim, T.-J. Ko, H.-S. Chung, A. Krishnaprasad, J. C. Flores, S.

Nehate, M. G. Kaium, J. B. Park, S.-J. Lee, K. B. Sundaram, L. Zhai, T. Roy, and Y. Jung, *Centimeter-Scale Periodically Corrugated Few-Layer 2D $MoS_2$ with Tensile Stretch-Driven Tunable Multifunctionalities*, ACS Appl. Mater. Interfaces **10**, 30623 (2018).

[52] K. He, C. Poole, K. F. Mak, and J. Shan, *Experimental Demonstration of Continuous Electronic Structure Tuning via Strain in Atomically Thin $MoS_2$*, Nano Lett. **13**, 2931 (2013).

[53] S. Manzeli, A. Allain, A. Ghadimi, and A. Kis, *Piezoresistivity and Strain-Induced Band Gap Tuning in Atomically Thin $MoS_2$*, Nano Lett. **15**, 5330 (2015).

[54] X. Wei, S. Xiao, F. Li, D.-M. Tang, Q. Chen, Y. Bando, and D. Golberg, *Comparative Fracture Toughness of Multilayer Graphenes and Boronitrenes*, Nano Lett. **15**, 689 (2015).

[55] Y. Yang, X. Li, M. Wen, E. Hacopian, W. Chen, Y. Gong, J. Zhang, B. Li, W. Zhou, P. M. Ajayan, Q. Chen, T. Zhu, and J. Lou, *Brittle Fracture of 2D $MoSe_2$*, Adv. Mater. **29**, 1604201 (2017).

[56] Z. Liao, L. Medrano Sandonas, T. Zhang, M. Gall, A. Dianat, R. Gutierrez, U. Mühle, J. Gluch, R. Jordan, G. Cuniberti, and E. Zschech, *In-Situ Stretching Patterned Graphene Nanoribbons in the Transmission Electron Microscope*, Sci Rep **7**, 211 (2017).

[57] K. Cao, S. Feng, Y. Han, L. Gao, T. Hue Ly, Z. Xu, and Y. Lu, *Elastic Straining of Free-Standing Monolayer Graphene*, Nat Commun **11**, 284 (2020).

[58] D. B. Williams and C. B. Carter, *Transmission Electron Microscopy* (Springer US,

Boston, MA, 2009).

[59] N. Tanaka, *Structure and Imaging of a Transmission Electron Microscope (TEM)*, in *Electron Nano-Imaging* (Springer Japan, Tokyo, 2017), pp. 17–28.

[60] M. J. Hÿtch, E. Snoeck, and R. Kilaas, *Quantitative Measurement of Displacement and Strain Fields from HREM Micrographs*, Ultramicroscopy **74**, 131 (1998).

[61] M. J. Hÿtch, J.-L. Putaux, and J.-M. Pénisson, *Measurement of the Displacement Field of Dislocations to 0.03 Å by Electron Microscopy*, Nature **423**, 270 (2003).

[62] S. Li, Y. Chang, Y. Wang, Q. Xu, and B. Ge, *A Review of Sample Thickness Effects on High-Resolution Transmission Electron Microscopy Imaging*, Micron **130**, 102813 (2020).

[63] M. Yi and Z. Shen, *A Review on Mechanical Exfoliation for the Scalable Production of Graphene*, J. Mater. Chem. A **3**, 11700 (2015).

[64] R. Yang, X. Zheng, Z. Wang, C. J. Miller, and P. X.-L. Feng, *Multilayer $MoS_2$ Transistors Enabled by a Facile Dry-Transfer Technique and Thermal Annealing*, Journal of Vacuum Science & Technology B, Nanotechnology and Microelectronics: Materials, Processing, Measurement, and Phenomena **32**, 061203 (2014).

[65] A. Castellanos-Gomez, M. Buscema, R. Molenaar, V. Singh, L. Janssen, H. S. J. van der Zant, and G. A. Steele, *Deterministic Transfer of Two-Dimensional Materials by All-Dry Viscoelastic Stamping*, 2D Materials **1**, 011002 (2014).

[66] H. Li, J. Wu, X. Huang, Z. Yin, J. Liu, and H. Zhang, *A Universal, Rapid Method for Clean Transfer of Nanostructures onto Various Substrates*, ACS Nano **8**, 6563

(2014).

[67] S. Wang, Z. Qin, G. S. Jung, F. J. Martin-Martinez, K. Zhang, M. J. Buehler, and J. H. Warner, *Atomically Sharp Crack Tips in Monolayer $MoS_2$ and Their Enhanced Toughness by Vacancy Defects*, ACS Nano **10**, 9831 (2016).

[68] P. Li, C. Jiang, S. Xu, Y. Zhuang, L. Gao, A. Hu, H. Wang, and Y. Lu, *In Situ Nanomechanical Characterization of Multi-Layer $MoS_2$ Membranes: From Intraplanar to Interplanar Fracture*, Nanoscale **9**, 9119 (2017).

[69] L. Tapasztó, T. Dumitrică, S. J. Kim, P. Nemes-Incze, C. Hwang, and L. P. Biró, *Breakdown of Continuum Mechanics for Nanometre-Wavelength Rippling of Graphene*, Nature Physics **8**, 739 (2012).

[70] N. Friedl, F. G. Rammerstorfer, and F. D. Fischer, *Buckling of Stretched Strips*, Computers & Structures **78**, 185 (2000).

[71] V. Nayyar, K. Ravi-Chandar, and R. Huang, *Stretch-Induced Stress Patterns and Wrinkles in Hyperelastic Thin Sheets*, International Journal of Solids and Structures **48**, 3471 (2011).

[72] D. Yan, K. Zhang, F. Peng, and G. Hu, *Tailoring the Wrinkle Pattern of a Microstructured Membrane*, Applied Physics Letters **105**, 071905 (2014).

[73] J. Huang, B. Davidovitch, C. D. Santangelo, T. P. Russell, and N. Menon, *Smooth Cascade of Wrinkles at the Edge of a Floating Elastic Film*, Physical Review Letters **105**, (2010).

[74] H. Vandeparre, M. Piñeirua, F. Brau, B. Roman, J. Bico, C. Gay, W. Bao, C. N. Lau, P. M. Reis, and P. Damman, *Wrinkling Hierarchy in Constrained Thin Sheets*

*from Suspended Graphene to Curtains*, Physical Review Letters **106**, 224301 (2011).

[75] J. S. Choi, Y. J. Chang, S. Woo, Y.-W. Son, Y. Park, M. J. Lee, I.-S. Byun, J.-S. Kim, C.-G. Choi, A. Bostwick, E. Rotenberg, and B. H. Park, *Correlation between Micrometer-Scale Ripple Alignment and Atomic-Scale Crystallographic Orientation of Monolayer Graphene*, Scientific Reports **4**, (2015).

[76] S. V. Dmitriev, J. A. Baimova, A. V. Savin, and Y. S. Kivshar, *Ultimate Strength, Ripples, Sound Velocities, and Density of Phonon States of Strained Graphene*, Computational Materials Science **53**, 194 (2012).

[77] J. Huang and Q. Han, *A Molecular Dynamics Study on Wrinkles in Graphene with Simply Supported Boundary under In-Plane Shear*, Journal of Nanomaterials **2017**, 1326790 (2017).

[78] W. Wong and S. Pellegrino, *Wrinkled Membranes I: Experiments*, J. Mech. Solids Struct. **1**, 3 (2006).

[79] M. Al-Gwaiz, V. Benci, and F. Gazzola, *Bending and Stretching Energies in a Rectangular Plate Modeling Suspension Bridges*, Nonlinear Analysis: Theory, Methods & Applications **106**, 18 (2014).

[80] J. L. Feldman, *Elastic Constants of 2H-MoS2 and 2H-NbSe2 Extracted from Measured Dispersion Curves and Linear Compressibilities*, Journal of Physics and Chemistry of Solids **37**, 1141 (1976).

[81] Z. Qin, G. Qin, and M. Hu, *Origin of Anisotropic Negative Poisson's Ratio in Graphene*, Nanoscale **10**, 10365 (2018).

[82] G. Qin and Z. Qin, *Negative Poisson's Ratio in Two-Dimensional Honeycomb Structures*, Npj Comput Mater **6**, 51 (2020).

[83] Q. Peng and S. De, *Outstanding Mechanical Properties of Monolayer $MoS_2$ and Its Application in Elastic Energy Storage*, Phys. Chem. Chem. Phys. **15**, 19427 (2013).

[84] B. Wang, J. Wu, X. Gu, H. Yin, Y. Wei, R. Yang, and M. Dresselhaus, *Stable Planar Single-Layer Hexagonal Silicene under Tensile Strain and Its Anomalous Poisson's Ratio*, Appl. Phys. Lett. **104**, 081902 (2014).

[85] Z. W. Ulissi, A. Govind Rajan, and M. S. Strano, *Persistently Auxetic Materials: Engineering the Poisson Ratio of 2D Self-Avoiding Membranes under Conditions of Non-Zero Anisotropic Strain*, ACS Nano **10**, 7542 (2016).

# Appendix I

### The evaluation of total tensile strain on the ripple structure

We should notice that the rippled structures, which are induced by the initial shear strain, the longitudinal x-direction is 45° to the boundary of the trench, as we mention in Chapter 6.1. Here we show the method to estimate the tensile strain on the rippled structure.

The direction that perpendicular to the trench is the X direction, it is the original X-Y coordinate when we discuss the initial shear strain, and the shear strain $\gamma$ is along the Y-direction. When we discuss the tensile strain of ripple structure (the x direction of ripples, the x-y coordinate, angle between the x-direction and X-direction is 45°), there is a transformation of strain from one coordinate system to another (from X-Y to x-y coordinate). The relationship can be retrieved from Morh's circle, and it can also be retrieved from the deformation.

Considering the rippled structures were formed by the initial shear strain ($\gamma$). For a simple shear that $\gamma = \frac{\Delta H}{L}$, where $\Delta H$ is the displacement perpendicular to the trench, as shown in Fig. S1.1. Here, the x- and y-direction indicating the longitudinal and transverse direction of ripples. The initial length along the x-direction is $\frac{L}{\sin\alpha}$, the

longitudinal deformation with a shear strain is $\Delta H cos\alpha$, thus, the tensile strain ($\varepsilon_{xsh}$) induced by the shear strain is:

$$\varepsilon_{xsh} = \frac{\Delta H \cos\alpha}{\frac{L}{\sin\alpha}} = \frac{\Delta H \cos\alpha \sin\alpha}{L} = \frac{1}{2}\gamma \sin 2\alpha \; . \tag{S1.1}$$

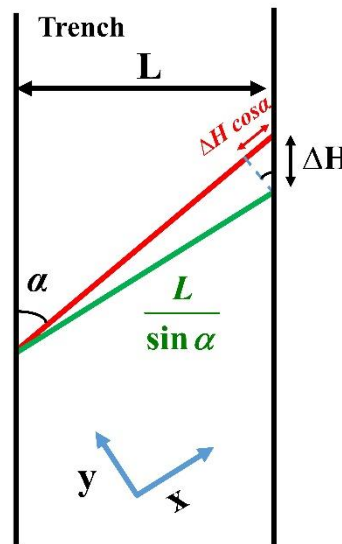


Figure S1.1. Diagram of the relationship between the initial shear strain γ and correspondingly induced tensile strain $\varepsilon_{xsh}$ of the ripples. The green line and red line indicate the longitudinal length without and with the shear strain $\gamma$. $\alpha$ is the angle between the x-direction of the ripple and the perpendicular direction of trench.

When the $\varepsilon_{appl}$ applied on the trench, the shear strain will change to:

$$\gamma' == \frac{\Delta H}{L + \Delta L} = \frac{\frac{\Delta H}{L}}{1 + \frac{\Delta L}{L}} = \frac{\gamma}{1 + \varepsilon_{appl}} \; . \tag{S1.2}$$

The relationship between the applied strain on the trench ($\varepsilon_{appl}$) and the correspondingly tensile strain component ($\varepsilon_{xap}$) was illustrated the Fig. S1.2. The

applied strain on the trench can be defined as: $\varepsilon_{appl} = \frac{\Delta L}{L}$ , where L is the initial width of the trench, and the $\Delta L$ is the deformation of the width with stretching, as shown in Fig. S1.2. The length along the x-direction of ripple is $\frac{L}{\sin\alpha}$ , and the longitudinal deformation is $\Delta L \sin\alpha$ , then, the stretching induced tensile strain $\varepsilon_{xap}$ can be calculated as:

$$\varepsilon_{xap} = \frac{\Delta L \sin\alpha}{\frac{L}{\sin\alpha}} = \frac{\Delta L \sin^2\alpha}{L} = \varepsilon_{appl} \sin^2\alpha . \tag{S1.3}$$

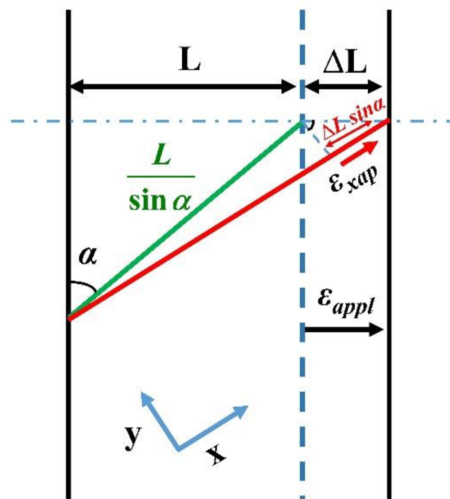


Figure S1.2. The diagram shows relationship between the strain applied on the trench and corresponding tensile strain. The green line and red line indicate the longitudinal length before and after the strain applied on trench. And α is the angle between the x-direction of ripple and the trench. The x- and y-direction indicating the longitudinal and transverse direction of ripples.

Therefore, the total tensile strain $\varepsilon_x$ can be obtained by the sum of shear induced tensile strain $\varepsilon_{xsh}$ and stretching induced tensile strain $\varepsilon_{xap}$, as illustrated in Fig. S1.3. The $\varepsilon_x$ can be obtained:

$$\varepsilon_x = \varepsilon_{xsh} + \varepsilon_{xap} = \frac{1}{2}\frac{\gamma}{1+\varepsilon_{appl}}\sin 2\alpha + \varepsilon_{appl}\sin^2\alpha \ . \quad \text{(S1.4)}$$

In the case of α is 45°, Eq. (S1.4) is simplified as $\varepsilon_x = \frac{1}{2}(\frac{\gamma}{1+\varepsilon_{appl}} + \varepsilon_{appl})$.

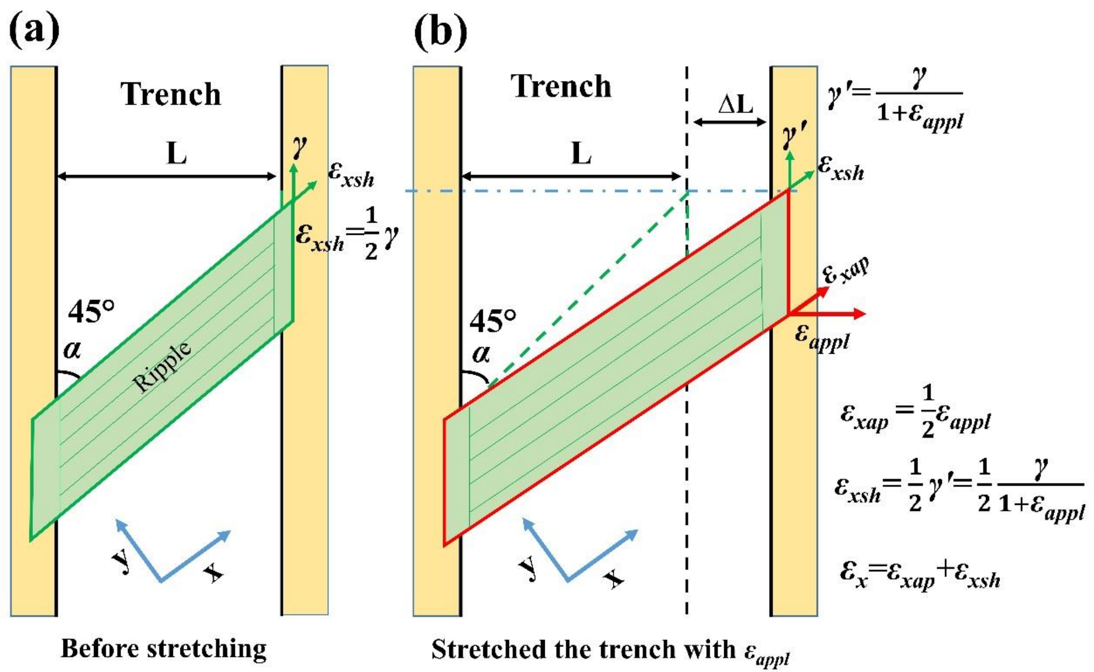


Figure S1.3. Illustration showing components of the tensile strain of rippled structure, where γ is the original shear strain, $\varepsilon_{appl}$ is the applied strain on trench, α is 45°.

# Acknowledgement

First of all, I would like to express my sincere thanks to my supervisor, Professor Yoshifumi Oshima. I am greatly indebted to Prof. Oshima for his kind supervision, strong support, and great encouragement during my study. Thanks for providing the guidance on the experiment, and the way of thinking about research. I have learned a lot not only in the research but also in life. In addition, I had a valuable experience because I had many opportunities to take participate in academic conferences.

Then I would like to express my deep thanks to Professor Masahiko Tomitori, my Second supervisor, for providing me with variable advice and suggestions on my research.

I would like to thank Professor Mikio Koyano for his patient instruction, valuable suggestions, and assistance during my minor research. The study with Prof. Mikio Koyano gave me a further understanding of my main research. I also would like to express a special debt of gratitude to Assistant Prof. Masanobu Miyata, who instructed and helped me a lot with the DFT calculation.

I am really grateful to Prof. Yukiko Takamura (JAIST) and Prof. Satoru Tanaka (Kyushu University) for devoting much time to reading this thesis and give me much advice, which will benefit me in my later study.

I am thankful for the support given by Associate Professor Masashi Akabori for his instruction on electron beam deposition. I also thank Associate Professor Xiaobin Zhang (Shibaura Institute of Technology) for her support on the sample preparation.

I would like to express my appreciation to Dr. Y. Chiew, Dr. C. Liu, Dr. J. Zhang, and, Mr. T. Chen in our lab for their kindly discussion and suggestion to my research. I also thank my friends, Dr. Z. Li, Dr. X. Wang, Dr. Y. Zhang, Dr. P. Cheng, Mr. X. Liu, and Mr. B. Cao for their kindly discussions and support. Thanks to my friends in JAIST for giving me a memorable life here.

In addition, special thanks to my family for their sincere support.

Thanks for the support of the MEXT scholarship during the doctoral course.

# List of achievements

## List of Publication

1. Lilin Xie and Yoshifumi Oshima, "Quantitative estimation of atom-scaled ripple structure using transmission electron microscopy images". Nanotechnology. **32** .185703(2021).

2. Lilin Xie and Yoshifumi Oshima, "Nonlinear mechanical response of rippled $MoS_2$ nanosheets evaluated by in situ transmission electron microscopy". (submitted)

3. Lilin Xie and Yoshifumi Oshima, "Development of the in situ stretching TEM holder for 2D materials". (preparing)

## Domestic Conferences

1. Lilin Xie and Yoshifumi Oshima, "Estimation of Atom-scaled Ripple Structure of $MoS_2$ from HRTEM Image", The 77th Annual Meeting of the Japanese Society of Microscopy, 14-16 June 2021, Tsukuba, online. (Oral)

2. Lilin Xie and Yoshifumi Oshima, "Identification of atom-scaled rippled structure of $MoS_2$ film from HRTEM image", Annual meeting of The Japan Society of Vacuum and Surface Science 2020, 19-21 November 2020, online. (Oral)

3. Lilin Xie and Yoshifumi Oshima, "Identify the rippled structure of $MoS_2$ film from HRTEM image", The 81th Japan Society of Applied Physics Autumn Meeting 2020, 8-11 September 2020, online. (Oral)

4. Lilin Xie and Yoshifumi Oshima, "Strained induced ripples and structure change in $MoS_2$ nanosheet", The 67th Japan Society of Applied Physics Spring Meeting 2020, 12-15 March 2020, Tokyo. (Oral)

5. Lilin Xie, Xiaona zhang and Yoshifumi Oshima, "Dislocation-Driven Growth of CuO Nanowires", The 66th Japan Society of Applied Physics Spring Meeting 2019, 9-12 March 2019, Tokyo. (Poster)

## International Conferences

1. Lilin Xie and Yoshifumi Oshima, "Development of stretching TEM holder for 2D materials", 2019 Annual Meeting of Electron Microscopy Society of China, 15-18 October 2019, Hefei, China. (Poster)